

Centro Brasileiro de Pesquisas Físicas
CBPF

Ph.D. Thesis

**NMR Quantum Information Processing
in Three-Qubit Systems: applications to
Quantum State Tomography,
Teleportation and the Yang-Baxter
problem**

Fatemeh Anvari Vind

Rio de Janeiro

To my parents, my mother and my father

Acknowledgements

First, I would like to thank my advisor, Professor Ivan S. Oliveira. His knowledge, intuition and honesty in science have been very inspiring. I want to thank him for having given me the chance to work in his lab. Despite encountering difficulties in either specific subject materials or general research and academic directions, he has always been extremely supportive, encouraging and infinitely patient.

I would like to acknowledge my advisor Professor Roberto S. Sarthour for his support and guidance. I enjoyed his guidance, his support and his refreshing insights throughout the course of my thesis.

I would like to thank Professor Alexandre M. Souza for teaching me the technical aspects of the experiment, and his deep involvement with the project even during the busiest of times.

It is been a blessing to be able to work and become friends with members of the NMR lab and I thank them for their friendship and encouragements.

Finally, I would like to thank my family whose love and presence continue to fuel and inspire me in everything I do.

Abstract

This thesis is composed of two different experiments, performed during my Ph.D. program in the Laboratory of Nuclear Magnetic Resonance (NMR), at the Brazilian Center for Research in Physics. For the last ten years, NMR has become one of the main experimental tools to implement quantum protocols of computation and communication.

In the first work, we developed a technique for Quantum State Tomography (QST) in a three qubits system consisting of strongly coupled nuclear spins, known in the NMR literature as “*ABX*” systems. We found that the number of experiments necessary to perform QST in such systems can be reduced in respect to those of three qubits weakly coupled, and, therefore reducing the experimental effort required for the complete density matrix reconstruction. To test the procedure we have implemented the full protocol for quantum teleportation. The tomographed results demonstrate that the density matrix can be reconstructed with less operations, and high fidelity.

The second work presented in this thesis is implementation of two-dimensional (2D) Yang-Baxter Equation (YBE) in NMR. The YBE first appeared in theoretical physics, in a paper by Yang [1], and in the work of Baxter in Statistical Mechanics [2, 3]. It turned out to be one of the basic equations in mathematical physics, and more precisely for introducing the theory of quantum groups. The Yang-Baxter Equation also plays an important role in completely integrable statistical models, Knot theory, braided categories, quantum computing, etc. The YBE is a universal gate for quantum computation and some solutions of the YBE are unitary and then they can be seen as a quantum gate. We present a practical scheme to test the YBE in the framework of quantum information. Then we experimentally test the validity of 2D YBE in NMR. The optically implementing YBE has been performed in [4].

Resumo

Esta tese é composta por dois trabalhos diferentes, realizados durante meu programa de doutorado no Laboratório de Ressonância Magnética Nuclear (RMN), do Centro Brasileiro de Pesquisas Físicas. Nos últimos dez anos, RMN se tornou uma das principais ferramentas experimentais para a implementação de protocolos quânticos de computação e comunicação.

No primeiro trabalho, aprimoramos um protocolo de Tomografia de Estado Quântico (TEQ) em um sistema de três q-bits formado por spins nucleares fortemente acoplados, conhecido na literatura de RMN como sistema “*ABX*”. Nós encontramos que o número de experimentos necessários para realizar TEQ em sistemas como esse pode ser reduzido com relação àqueles com três q-bits fracamente acoplados e, portanto, reduzindo o esforço experimental requerido para a reconstrução total da matriz densidade. Para testar o procedimento nós implementamos o protocolo completo para o teleporte quântico. Os resultados tomografados demonstram que a matriz densidade pode ser reconstruída com menos operações e alta fidelidade.

O segundo trabalho apresentado nesta tese é a implementação da Equação de Yang-Baxter (EYB) em RMN. A EYB apareceu primeiro na Física Teórica, em um artigo de Yang [1], e no trabalho de Baxter em Mecânica Estatística [2, 3]. Ela se tornou uma das equações básicas na Física Matemática, e mais precisamente na introdução da Teoria de Grupos Quânticos. A equação de Yang-Baxter também desempenha um papel importante em modelos estatísticos completamente integráveis, Teoria de Nós, Categorias Trançadas, Computação Quântica etc. A EYB é uma porta universal para a Computação Quântica e algumas soluções da EYB são unitárias e então elas podem ser vistas como uma porta quântica. Nós testamos a EYB 2D em RMN. Nós apresentamos um esquema prático para testar a EYB no âmbito da Informação Quântica. Então nós testamos experimentalmente a validade da EYB 2D em RMN. A implementação óptica da EYB foi realizada em [4].

Contents

List of Figures	ix
------------------------	-----------

List of Tables	xvi
-----------------------	------------

CHAPTER 1. Introduction	1
1.1. NMR as a Quantum Information Processing	1
1.2. Yang-Baxter Equation	4
1.3. Organization Of The Dissertation	5

CHAPTER 2. Review on NMR and QIP Fundamentals	7
2.1. Spin	8
2.2. NMR Spin Systems	11
2.2.1. Interacting Spins	14
2.2.2. The Control Hamiltonian	16
2.2.3. Relaxation and Decoherence	19
2.3. Quantum Bits	21
2.3.1. Mixed States and The Density Operator	25
2.4. Quantum Gates	26
2.4.1. Single Qubit Gates	27
2.4.2. Two-Qubit Gates	33
2.4.3. Three-Qubit Gates	36
2.5. Magnetic Field Gradients	42
2.6. Initialization	43
2.6.1. The Initial State of Nuclear Spins and Effective Pure States	44
2.6.2. Spatial Labeling	46
2.6.3. Logical Labeling	47

2.6.4. Temporal labeling	48
2.7. Preparing Pseudo-Pure States With Controlled-Transfer Gates	50
2.8. Measurement	53
2.8.1. Interpretation of NMR Spectra	53
2.9. The NMR Spectrometer	56

CHAPTER 3. Gradient Ascent Pulse Engineering	65
3.1. The Optimal Control Framework	66
3.2. Optimal Control For Quantum Systems	66
3.3. Algorithmic Scheme	68
3.4. Robustness	74

CHAPTER 4. Quantum State Tomography For Strongly Coupled Nuclear Spin Systems: Theoretical Treatment	77
4.1. Time Domain Signal	78
4.2. Product-Operator Basis	82
4.3. Two Nuclei “ <i>AB</i> ” Spin System	85
4.4. Three Nuclei “ <i>ABX</i> ” Spin System	92

CHAPTER 5. Experimental Benchmarks	105
5.1. “ <i>AB</i> ” Spin System	106
5.2. “ <i>ABX</i> ” Spin System	110
5.2.1. Quantum Teleportation	113

CHAPTER 6. NMR Implementation of Two-Dimensional YANG-BAXTER Equation	121
6.1. Implementation of the Yang-Baxter Equation in Quantum Optics	123
6.1.1. Reduction of the 4D YBE to the 2D YBE	123
6.1.2. Using the Polarization Qubit to Implement the 2D YBE	126
6.1.3. Using the Location Qubit to Implement the 2D YBE	130
6.2. Implementation of the 2D YBE in NMR	133

CHAPTER 7. Conclusions	150
<i>Appendix</i>	154
CHAPTER A. Unitary Transformation	155
A.1. Transforms	156
Bibliography	161

List of Figures

2.1.	The direction of nuclear magnetic moment (a) in the absence of an external magnetic field (b) in the presence of an external magnetic field.	10
2.2.	In the presence of an external magnetic field, on average, the net magnetization is along the z direction.	10
2.3.	Energy diagram or Zeeman splitting for a spin-1/2 particle subject to a static magnetic field.	12
2.4.	The energy difference between the two spin states depends on the strength of the external magnetic field.	13
2.5.	Nutation of a spin subject to a transverse RF field (a) observed in the rotating frame and (b) observed in the laboratory frame.	18
2.6.	(a) Bloch sphere representation of an arbitrary quantum state $ \psi\rangle$ for a single qubit. (b) Representation of several important quantum states, ignoring the normalization factor.	23
2.7.	Quantum circuit representation of (a) the X gate, (b) the Y gate, (c) the Z gate, (d) the Hadamard gate, (e) the S gate and, (f) the T gate.	31
2.8.	quantum circuit representation of (a) a Controlled-NOT gate, (b) a Zero-Controlled-NOT, (c) a SWAP gate, and (d) a Controlled-U gate. The \bullet symbol denotes the control qubit- the controlled operation is only executed if the qubit is in the $ 1\rangle$ state. The \circ symbol denotes the Zero-Controlled qubit, i.e. the operation is only executed if the control qubit is in the state $ 0\rangle$	35
2.9.	quantum circuit representation of a Fredkin gate with qubits a as control and qubits b and c as targets.	37

2.10. quantum circuit representation of a Toffoli gate with qubits a and b as controls and qubit c as target.	38
2.11. Minimum pulse sequences for the Fredkin with qubits a as control and qubits b and c as targets. Time goes from left to right.	40
2.12. Minimum pulse sequences for the Toffoli with qubits a and b as controls and qubit c as target. Time goes from left to right.	40
2.13. Single qubit circuits which are simplified.	41
2.14. two qubit circuits which are simplified.	41
2.15. Scheme of an NMR sample and field lines in a region with gradient.	42
2.16. Quantum circuit representation of a Controlled-transfer gate with qubit a as control and qubit b as target. Magnetic field gradient is after Controlled-rotation gate and which is implicit.	50
2.17. Quantum circuit for the preparation of pseudo-pure state of a two-qubit system. The gates are applied from left to right.	51
2.18. Quantum circuit for preparation of pseudo-pure state of a three-qubit system. The gates are applied from left to right. Where the angles $\theta_1 = \arccos(-1/7) \approx 98.2^\circ$ and $\theta_2 = \arccos(-5/7) \approx 135.6^\circ$	52
2.19. (a) Free induction decay (FID) and (b) the Fourier transform of the FID signal (Carbon spectrum) from carbon-13 labelled trichloroethylene in the thermal equilibrium state.	55
2.20. Scheme of a NMR spectrometer.	57
2.21. A typical NMR sample. The sample tube is held by a sample holder when it is inserted in the superconducting magnet.	58
2.22. Varian 500 MHz NMR magnet. The fill ports for liquid Nitrogen and Helium are at the top of the magnet. The probe is inserted at the bottom of the magnet, while the sample is inserted from the top.	59
2.23. Block diagram of a NMR spectrometer (transmitter section).	60
2.24. Block diagram of a NMR spectrometer (receiver section).	62

3.1. The m 'th control function is represented by a piecewise-constant pulse sequence consisting M scalar control amplitudes u_m	73
3.2. The quadrature components of the fluorine control fields for a GRAPE pulse that implements a 90 degree rotation on $F2$ in the iodotrifluoroethylene molecule (see Chapter (6)). The total duration of the pulse is $1000\mu s$	76
3.3. The robustness of the pulse to radio frequency field inhomogeneities. The amplitude in the Fig. (3.2) is changed and then the fidelity (the overlap of the output state from the simulated unitary and the output from the ideal unitary) is calculated.	76
4.1. Energy level diagram of an "AB" spin system. The numbers correspond to the eigenstates given in Table (4.1).	86
4.2. Typical spectrum for two nuclei "AB". It is assumed that $\omega_A > \omega_B$ and $J > 0$	90
4.3. Energy level diagram of an "ABX" spin system. The numbers correspond to the eigenstates given in Table (4.4).	94
4.4. Typical spectrum for three nuclei "ABX". The lines 1, 2, 3, 4 are "B" lines; 5, 6, 7, 8 are "A" lines and 9, 10, 11, 12, 14, 15 are "X" lines. The numbering of lines applies if $\omega_A > \omega_B$ and $J_{23} > J_{13}$. The numbers in the figure are related to the transitions indicated in Table (4.6).	97
5.1. The structure and the parameters of carbon and proton labeled trichloroethylene (TCE) molecule. The diagonal terms in the table are the chemical shifts (in Hz) of the carbons and proton. The nondiagonal terms are the coupling constants, also in Hz. The numbers above the carbons and proton specify the number of qubits.	108
5.2. Thermal equilibrium spectra of trichloroethylene (a) Carbon spectrum when the proton is not decoupled, (b) proton spectrum and (c) carbon spectrum when proton is decoupled, obtained by applying selective readout pulses to the system in its thermal equilibrium state.	109

-
- 5.3. Real parts of the reconstructed density matrices for an “ AB ” system. (a) State $|11\rangle$ and (b) after the application of the $CNOT$ gate over the state $|11\rangle$, resulting in the state $|10\rangle$, where $CNOT_{ij}$ denotes a Controlled-NOT gate with the qubit i as control and the qubit j as target. The fidelity was over 0.99 in both cases. The rows and columns represent the standard computational basis in binary order, with $\langle 00|$ starting from the leftmost column and $\langle 11|$ being the rightmost column. 110
- 5.4. Quantum circuit diagram for the teleportation protocol. Here $C1$ and $C2$ are denoted as qubit 1 and qubit 2, respectively and H is denoted as qubit 3. Numbers written at the bottom of the picture are marks that indicate the steps of the teleportation. H 's inside the rectangles are Hadamard gates and $|\phi\rangle = (|0\rangle + |1\rangle)/\sqrt{2}$ 114
- 5.5. Pulse sequence used to prepare three-qubit pseudo-pure state, where G_z is the magnetic field gradient along z axis. 116
- 5.6. Experimental three-qubit density matrices for the teleport experiment. From (a) to (c) are shown the real parts of the reconstructed density matrices of the pseudo-pure state, $|\psi_0\rangle = |000\rangle$, first step, $|\psi_1\rangle = |\psi_{00}\rangle$, and second step, $|\psi_2\rangle = \frac{(|\psi_{00}\rangle + |\psi_{11}\rangle)}{\sqrt{2}}$, of the teleportation, respectively. The rows and columns represent the standard computational basis in binary order, with $\langle 000|$ starting from the leftmost column and $\langle 111|$ being the rightmost column. 117
- 5.7. Experimental density matrices: The real part of the reconstructed density matrix of the third step of the teleportation in (a) the computational basis, $|\psi_3\rangle$, (b) the Bell basis. The state is in an equal mixture of the four different possible combinations. For clarity, we zoomed on the submatrices along the diagonal to show the four different states in Eq. (5.7) more clearly ($|\psi_1^\pm\rangle = (1/\sqrt{2})(|0\rangle \pm |1\rangle)$ and $|\psi_2^\pm\rangle = (1/\sqrt{2})(|1\rangle \pm |0\rangle)$). The rows and columns represent the standard computational basis in binary order, with $\langle 000|$ starting from the leftmost column and $\langle 111|$ being the rightmost column. 118

5.8. Final step of the teleportation protocol.	119
5.9. Experimental density matrix: the real part of the final reconstructed density matrix in (a) the computational basis, $ \psi_4\rangle = \frac{ 0\rangle+ 1\rangle}{\sqrt{2}}\frac{ 0\rangle+ 1\rangle}{\sqrt{2}} \psi\rangle = \frac{ 0\rangle+ 1\rangle}{\sqrt{2}}\frac{ 0\rangle+ 1\rangle}{\sqrt{2}}\frac{ 0\rangle- 1\rangle}{\sqrt{2}}$ and (b) the Bell basis. The rows and columns represent the standard computational basis in binary order, with $\langle 000 $ starting from the leftmost column and $\langle 111 $ being the rightmost column.	120
6.1. (a) Half-Wave Plate (HWP) and (b) Quarter-Wave Plate (QWP).	126
6.2. Realization of operations (a) $A(\theta)$ and (b) $B(\theta)$ by optical elements. $U_Q(\theta)$ and $U_H(\theta)$ are the matrices of QWP and HWP, respectively, and θ is the angle between the optical device axes and the vertical direction.	129
6.3. Optical realization of the (a) Left-Hand-Side and Right-Hand-Side of the Yang-Baxter equation. The angles of these QWPs (filled) and HWPs (empty) must satisfy the relation given in Eq. (6.11).	130
6.4. Schematic of the Mach-Zehnder interferometer.	131
6.5. Schematic setup for implementing either side of the 2D YBE, Eqs. (6.28) and (6.27), by means of location qubit. (a) Implementation of the Left-Hand-Side. (b) Implementation of the Right-Hand-Side. The relations of different parameters are referred to Eq. (6.11).	132
6.6. The structure of the iodotrifluoroethylene molecule.	134
6.7. The fluorine spectrum of the system, obtained by applying selective readout pulses to the system in its thermal equilibrium state.	136
6.8. The fluorine spectrum of second qubit, obtained by applying selective readout pulse to the system in its thermal equilibrium state.	136
6.9. The pulse sequence for preparation pseudo-pure state in the first and second experiments. G_z is the magnetic field gradient in the z direction. The pulse sequence does include the refocusing π pulses.	137
6.10. The pulse sequence for preparation the pseudo-pure state, where $\phi_1 = 98.2^\circ$, $\phi_2 = 135.6^\circ$ and G_z is the magnetic field gradient in the z direction. The pulse sequence includes the refocusing π pulses.	138

6.11. Pseudo-pure spectrum of iodotrifluoroethylene for second qubit.	138
6.12. The quantum circuit diagram for first step of the 2D YBE experiment. . .	139
6.13. The total quantum circuit diagram for implementation of the 2D YBE. F_1 , F_2 and F_3 are denoted as qubit 1, qubit 2 and qubit 3, respectively. The first part is separated from the final part by the blue line.	140
6.14. The first part of the quantum circuit after simplification.	140
6.15. Schematic of the Controlled-Swap gate logic circuit.	141
6.16. The quantum circuit diagram for the final step of the 2D YBE experiment (it consists Hadamard gate on second qubit and Controlled-Swap gate with second qubit as controll). The pulse sequence includes the refocusing π pulses.	141
6.17. The first part of the quantum circuit in Fig. (6.14) when $\theta_1 = -\theta_3$, $\theta_2 = 0$ and θ_3 varies between 0 and 2π	142
6.18. The total magnetization of qubit 2 when $\theta_1 = -\theta_3$, $\theta_2 = 0$ and θ_3 varies between 0 and 2π . The blue line is theoretical, the green dashed line is simulation and the red circles are experimental.	143
6.19. The histogram of the experimental data when $\theta_1 = -\theta_3$, $\theta_2 = 0$ and θ_3 varies between 0 and 2π	144
6.20. Comparison between the three times of implementation 2D YBE for correct angles when $\theta_1 = -\theta_3$, $\theta_2 = 0$ and θ_3 varies between 0 and 2π	144
6.21. The first part of the quantum circuit in Fig. (6.14) when $\theta_2 = \theta_3 = 0$ and θ_1 varies between 0 and 2π	145
6.22. The total magnetization of qubit 2 when $\theta_2 = \theta_3 = 0$ and θ_1 varies between 0 and 2π . The blue line is theoretical, the green dashed line is simulation and the red circles are experimental. For the wrong angles, the total mag- netization of qubit 2 is less than one and for the correct angles, the total magnetization of qubit 2 is one.	146
6.23. Comparison between the three times of implementation 2D YBE for wrong angles when $\theta_2 = \theta_3 = 0$ and θ_1 varies between 0 and 2π	146

-
- 6.24. The first part of the quantum circuit in Fig. (6.14) when $\theta_1 = \frac{\pi}{2}$, $\theta_3 = \frac{\pi}{4}$ and θ_2 varies between 0 and 2π 147
- 6.25. The total magnetization of qubit 2 when $\theta_1 = \frac{\pi}{2}$, $\theta_3 = \frac{\pi}{4}$ and θ_2 varies between 0 and 2π . The blue line is theoretical, the green dashed line is simulation and the red circles are experimental. For the wrong angles, the total magnetization of qubit 2 is less than one. 147
- 6.26. The first part of the quantum circuit in Fig. (6.14) when $\theta_1 = 2\theta_2$, $\theta_3 = \frac{\pi}{2}$ and θ_1 varies between 0 and 2π 148
- 6.27. The total magnetization of qubit 2 when $\theta_1 = 2\theta_2$, $\theta_3 = \frac{\pi}{2}$ and θ_1 varies between 0 and 2π . The blue line is theoretical, the green dashed line is simulation and the red circles are experimental. For the wrong angles, the total magnetization of qubit 2 is less than one. 149
- 6.28. The comparison between 13 times repeat the experiment in Fig. (6.26) with errorbar, when $\theta_1 = 2\theta_2$, $\theta_3 = \frac{\pi}{2}$ and θ_1 varies between 0 and 2π 149

List of Tables

2.1.	Larmor frequencies [MHz] of several species of nuclei, at 11.74 Tesla.	13
3.1.	Control parameters input into the GRAPE algorithm for trichloroethylene molecule (see Chapter (5)).	75
3.2.	Control parameters input into the GRAPE algorithm for iodotrifluoroethylene molecule (see Chapter (6)).	75
4.1.	The four eigenstates for two nuclei “AB”. Where $\alpha = 0$, $\beta = 1$ and $\theta = \frac{1}{2} \tan^{-1}(\frac{2\pi J_{12}}{\omega_1 - \omega_2})$ is the mixing angle.	86
4.2.	Examples of NMR “AB” spin systems.	87
4.3.	Transition Energies and Intensities for two nuclei spins “AB”.	89
4.4.	The eight eigenstates for three nuclei “ABX”. Where $\alpha = 0$, $\beta = 1$ and $\theta^\pm = \frac{1}{2} \tan^{-1} \frac{2\pi J_{12}}{\omega_1 - \omega_2 \pm \pi(J_{13} - J_{23})}$	93
4.5.	Examples of NMR “ABX” spin systems.	94
4.6.	Transition Energies and Intensities for three nuclei “ABX”, where $\bar{\omega} = \frac{(\omega_1 + \omega_2)}{2}$ and $\theta^\pm = \frac{1}{2} \tan^{-1} \frac{2\pi J_{12}}{\omega_1 - \omega_2 \pm \pi(J_{13} - J_{23})}$	97
5.1.	The pulse set, together, yield the complete tomography of two-spin homonuclear system. The pulse set labeled 1X applied to the two-spin system, for example, specifies no pulse on spin 1, and an X pulse on spin 2.	107
5.2.	Control parameters input into the GRAPE algorithm for trichloroethylene molecule (see Chapter (3)).	109
5.3.	Nine pulse sets that, together, yield complete tomography on an “ABX” spin system.	113

6.1. The parameters of fluorine labeled iodotrifluoroethylene molecule. The diagonal terms in the table are the chemical shifts (in Hz) of the fluorines. The off-diagonal terms are the coupling constants, also in Hz	134
6.2. Control parameters input into the GRAPE algorithm for iodotrifluoroethylene molecule.	135



Introduction

SECTION: 1.1

NMR as a Quantum Information Processing

Quantum information science is an exciting, emerging field that promises to dramatically improve the acquisition, transmission and processing of information. In 1948 Claude Shannon published a paper with the title: A mathematical theory of communication. On this paper, Shannon defined the unit of information, the binary digit, or bit, and established the theory which tells us how to determine the amount of information (i.e., the number of bits) which can be sent per unit time through a communication channel, and how this information can be fully recovered, even in the presence of noise in the channel. This work founded the theory of information.

In the early 1980s, scientists, including Richard Feynman [5], considered possible schemes to exploit the laws of quantum physics to compute. This led to the idea of a quantum computer, i.e. a computer whose functional principles would be based on the

quantum mechanical laws.

In the last decades it has been shown that Nuclear Magnetic Resonance (NMR) is an excellent tool for testing principles of quantum information science and developing techniques to control quantum systems [6]. To date, NMR is one of the most accurate techniques in terms of quantum control, capable of implementing experiments with up to twelve quantum bits [7] and hundreds of logical operations [8, 9]. One approach to achieve highly precise control, first introduced in Ref [10], consists of using numerically optimized shaped pulses. A substantial improvement over the initial proposal was obtained by applying optimal control theory to the problem of handling quantum nuclear spins states. This effort resulted in the Gradient Ascent Pulse Engineering (GRAPE) algorithm [11].

In a NMR quantum information processor, qubits are represented by the nuclear spins contained within an ensemble of molecules. NMR is an effective tool for demonstrating and developing new techniques for QC, due to its long decoherence time (on the order of seconds) relative to the timescales over which unitary evolutions occur. This suggested that quantum information can be preserved over the course of computation. The application of Radio-Frequency (RF) pulses in NMR also provides a robust method for coherently controlling the interactions between specific spins in the system, thereby allowing the precise implementation of unitary gates [12].

The realization of a quantum information processor in a NMR system was a challenge at first because spins are in a mixed state at room temperature, whereas QC requires systems in a pure state. Proposals for performing QC in such an ensemble system were first given by Cory, Fahmy, Havel [13], Gershenfeld and Chuang [14]. The method outlined in [13] involves the creation of pseudo-pure states, which are mixed states that transform similarly to pure spin states. The highly mixed nature of the spin states renders the creation of pseudo-pure states for more than ten qubits impractical [13, 15]. However, in the nascent stage of experimentally realizing QC, NMR remains a potent technology

for developing control methods and demonstrating the implementation of standard quantum algorithms. In 1998 the first quantum algorithm was experimentally demonstrated in Isaac Chuang's laboratory, using NMR techniques [16] and nearly simultaneously by Jones's group [17]. Their experiments clearly demonstrated a quantum algorithm and suggested that much larger implementations using NMR techniques are accessible.

Quantum information processing (QIP) has become a major field of research because of its broad potential of applications: faster-than-classical algorithms, unique quantum processes to perform novel tasks (teleportation, quantum cryptography, etc.), efficient simulation of quantum systems, and a thought-provoking role in the exploration of quantum mechanics and its foundations. But despite great developments, many implementation issues remain unsolved.

In liquid solutions the internal Hamiltonian of a spin system consists of the Zeeman Hamiltonian, describing the magnetic interaction of nuclear spins with a static magnetic field, and the indirect J coupling Hamiltonian, describing the interaction of pairs of nuclear spins through the bonding electrons. The indirect interaction can be classified as weak or strong, depending on the relative magnitude of the scalar coupling constant between two spins and the difference of their Larmor frequencies [18, 19]. One approach to avoid unwanted evolutions during the implementation of quantum operations, caused by such internal Hamiltonian, consists of decomposing the actual propagator into a target propagator followed by error terms which can be tracked and corrected. This approach is mostly used for weakly coupled systems and allows high fidelity quantum gates to be implemented with regular shaped pulses, as described in [20]. For strongly coupled systems, however, the task of implementing quantum computation becomes more complicated, and optimal control theory is often necessary to achieve high fidelities.

After the application of the correct dynamics to the spin system, either by employing regular shaped pulses or optimal control theory, it is necessary to characterize the

final state. This task is often accomplished by performing Quantum State Tomography (QST). The first QST on NMR system was reported by Chuang et al.[21] for systems of two coupled spins $1/2$. Later, different methods were proposed for quadrupolar nuclei systems [22, 23, 24] and n weakly coupled spins [25]. In this thesis, we have studied QST in a system with strongly coupled spins, known in NMR literature as “ ABX ” system. We have found that the number of experiments necessary to perform QST in an “ ABX ” system can be reduced with respect to three weakly coupled qubits. To test the procedure we have simulated the full quantum teleportation protocol. The results demonstrate that good accuracy in the density matrix reconstruction can be achieved.

SECTION: 1.2

Yang-Baxter Equation

The Yang-Baxter Equation (YBE) originated from solving the repulsive δ interaction problem in one-dimension of N particles [1, 26], and problems of statistical models on lattices [2, 3, 27]. Today, the Yang-Baxter Equation has become an important tool in physics, and has many applications in a variety of areas of physics, for instance in quantum field theory, statistical mechanics, and group theory [2, 3, 27, 28, 29, 30, 31, 32, 33, 34, 35, 36, 37]. It can be applied in completely integrable statistical models to find the solutions by means of the nested Bethe ansatz [37]. Recently it turns up gradually that the Yang-Baxter Equation is naturally linked to a hot area of frontier research, quantum information and computing [38, 39]. It is found that the Yang-Baxter Equation is closely related to quantum entangled states [40, 41], and the braiding operations in the Yang-Baxter equation are universal quantum gates [42, 43, 44, 45, 46]. The Yang-Baxter Equation attracts much attention in recent years and is being studied intensively in the context of quantum correlation and entanglement, and topological quantum computing [47, 48, 49, 50, 51, 52, 53, 54].

Due to its importance, the experimental verification of Yang-Baxter Equation has been pursued all along. Notably, an experimental verification was carried out by Tennant et al in 1995 [55, 56]. Tennant et al measured the spectrum of Heisenberg spin-half chain, and the experimental result appeared to agree with the calculation based on the Yang-Baxter Equation. Recently, the density profile of 1-dimensional wires was measured and it agreed well with the theoretical calculations based on Yang's solvable model [57].

Hu, Xue and Ge gave an explicit optical realization of the Yang-Baxter Equation in 2008 [4]. By the use of the Temperley-Lieb algebra, they made a remarkable reduction that obtained a Yang-Baxter Equation with dimension 2, the minimum dimensional Yang-Baxter Equation so far. Then, Zheng-Li-Song-Long experimentally implemented the Hu-Xue-Ge scheme and demonstrated the validity of the Yang-Baxter Equation using linear quantum optical components such as beamsplitters, half-wave plates, quarter wave plates, and etc [58]. In our experiment, we experimentally implemented and demonstrated the validity of the Yang-Baxter Equation using Nuclear Magnetic Resonance. The equality of the two sides of the Yang-Baxter Equation is directly verified.

SECTION: 1.3

Organization Of The Dissertation

This thesis is organized as follows: The Chapter (2) is intended for review on NMR and QIP fundamentals. In Chapter (3), we introduce the optimal control framework and benchmark an optimal control algorithm known as GRAPE which updates all control variables in a concurrent manner. We specify the algorithmic scheme by analyzing the most important components; different procedures for computing the gradient and the update step are presented. In the following Chapters, (4) and (5), we analyze the Quantum State Tomography (QST) in two and three qubits systems consisting of strongly coupled nuclear spins, known in the NMR literature as “*AB*” and “*ABX*” systems, respectively and show that the reconstruction of the density matrix for “*AB*” and “*ABX*” systems

can be improved. We also present the results for implementation of the full protocol for quantum teleportation. In Chapter (6), we present the NMR implementation of the two-dimensional Yang-Baxter Equation and demonstrate its validity. The equality between the two sides of the Yang-Baxter equation in two-dimension has demonstrated directly. In Chapter (7), final conclusions are presented.

2

Review on NMR and QIP Fundamentals

Nuclear Magnetic Resonance (NMR) is a spectroscopic technique which is conventionally used to gain information about static and dynamic properties of magnetically active nuclei. NMR was discovered in 1945 by E. M. Purcell et al., and F. Bloch et al., [6]. They discovered almost simultaneously that the nuclear spins of molecules which are placed in a magnetic field, can be controlled by electromagnetic excitation at a given frequency, therefore leading to nuclear magnetic resonance (NMR). Since then, NMR has been the subject of intensive research and development. The technology is now sufficiently advanced to allow accurate control of the state of nuclear spins. In the year of 1997 Cory et al. [59] and Gershenfeld et al. [60], independently, proposed NMR as a possible experimental technique to implement a quantum information processing (QIP). NMR is an excellent tool for testing principles of quantum information science and developing techniques to control quantum systems [6]. The success of NMR as a test-bed of experimental QIP may be attributed to the well established theory of NMR and availability of extremely sophisticated NMR instruments. In this section we will discuss the theory of NMR in

the context of QIP. The concepts of NMR are discussed in greater depth in the books of Oliveira [6], Slichter [61] and Ernst [18], etc.

SECTION: 2.1

Spin

Matter is made of atoms. Atoms are made up of electrons and nuclei. Each atomic nucleus (protons and neutrons composing the atomic nucleus) possesses a property called spin, which is a fundamental and important property along with mass, electric charge and magnetic moment. Spin is so called because it has very similar behaviour to classically spinning systems with properties such as angular momentum and a frequency.

The atomic nucleus has a positive charge. In some nuclei, this positive charge rotates about the nuclear axis. This spinning charge generates a small magnetic field and therefore the nucleus possesses a magnetic moment along the axis of rotation. The magnetic moment is represented by $\boldsymbol{\mu}$. The spinning atomic nucleus also has angular momentum and the relationship between these quantities is described by:

$$\boldsymbol{\mu} = \gamma \mathbf{J}, \quad (2.1)$$

where γ is the gyromagnetic ratio and it is a fundamental nuclear constant which has a different value for every nucleus. The angular momentum is described in terms of the nuclear spin operator, \mathbf{I} as:

$$\mathbf{J} = \hbar \mathbf{I}, \quad (2.2)$$

where \hbar is Planck's constant divided by 2π . The spin value (represented by I) depends on the number of protons and neutrons or the atomic and mass numbers. Spin numbers have values of 0, 1/2, 3/2, and so forth. If the number of both, protons and neutrons, is even then there is no overall spin and $I = 0$. If the number of neutrons plus the number

of protons is odd, then the nucleus has a half-integer spin (i.e. $I = 1/2, 3/2, 5/2$). If the number of both, protons and neutrons, is odd, then the nucleus has an integer spin (i.e. $I = 1, 2, 3$).

The quantum characteristics of the nuclear spin operator are given by the eigenvalues and eigenvectors of its square modulus (denoted by \mathbf{I}^2) and its z-component (denoted by I_z) [6]:

$$\mathbf{I}^2 |I, m\rangle = I(I + 1) |I, m\rangle, \quad (2.3)$$

$$I_z |I, m\rangle = m |I, m\rangle, \quad (2.4)$$

where $I^2 = I_x^2 + I_y^2 + I_z^2$. The state vectors denoted by $|I, m\rangle$ correspond to the common eigenvectors of \mathbf{I}^2 and I_z , being specified by the quantum numbers I and m , with $m = -I, -I + 1, \dots, I - 1, I$. The action of the components, I_x and I_y on the basis $|I, m\rangle$ can be evaluated using the raising and lowering operators, which are defined from as:

$$I_{\pm} = I_x \pm iI_y, \quad (2.5)$$

such that:

$$I_x = \frac{1}{2}(I_+ + I_-), \quad I_y = \frac{-i}{2}(I_+ - I_-). \quad (2.6)$$

The actions of such operators on the $|I, m\rangle$ vectors are given by [6]:

$$\begin{aligned} I_+ |I, m\rangle &= \sqrt{I(I + 1) - m(m + 1)} |I, m + 1\rangle, \\ I_- |I, m\rangle &= \sqrt{I(I + 1) - m(m - 1)} |I, m - 1\rangle. \end{aligned} \quad (2.7)$$

In a macroscopic sample and in the absence of an external magnetic field, normally the nuclear magnetic moments are randomly oriented and the vector sum of all nuclear magnetic moments is zero. So, the net sample magnetization is zero. When placed in an external magnetic field, the nuclear magnetic moment can either be aligned with the external magnetic field or anti-aligned with the external magnetic field but the majority is

aligned with the external magnetic field. Therefore, the net magnetization will be aligned with the external magnetic field. As it is shown in Figs. (2.1) and (2.2).

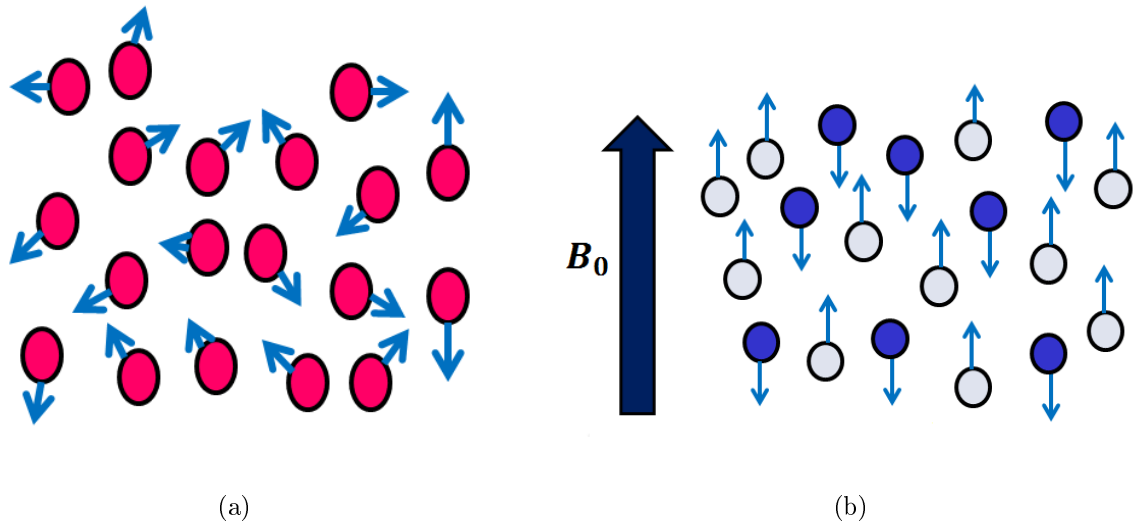


Fig. 2.1: The direction of nuclear magnetic moment (a) in the absence of an external magnetic field (b) in the presence of an external magnetic field.

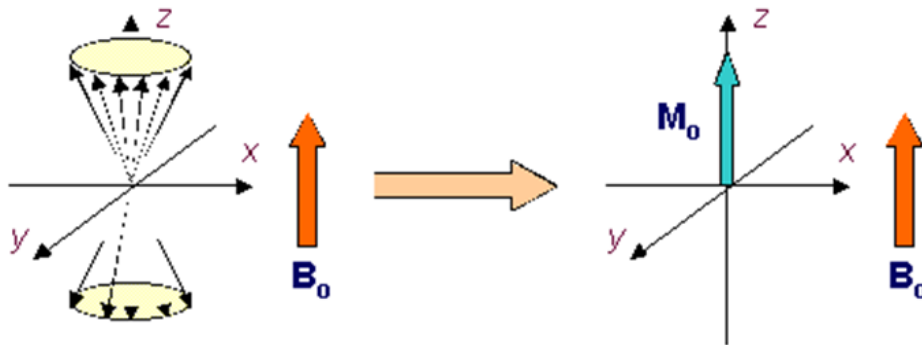


Fig. 2.2: In the presence of an external magnetic field, on average, the net magnetization is along the z direction.

Each nuclear magnetic moment in a sample precesses around the external magnetic field with a frequency ω_0 which is called Larmor frequency. The Larmor frequency is given by:

$$\omega_0 = \gamma B_0, \quad (2.8)$$

where the Larmor frequency is proportional to the gyromagnetic ratio.

SECTION: 2.2

NMR Spin Systems

The Hamiltonian of NMR spin system is comprised by the system Hamiltonian and the control Hamiltonian, $H = H_S + H_C$. The system Hamiltonian, H_S , describes the interactions among the spins and the interaction between the spins and an external magnetic field. The control Hamiltonian, H_C , describes the interaction between the spins and an oscillating radio frequency field. The most common nuclei observed in NMR spectroscopy have spin - 1/2 because they have two discrete energy levels. Some example of spin 1/2 nuclei are 1H , ^{13}C , ^{15}N , ^{19}F , and ^{31}P . Spin-0 nuclei are not magnetic and hence they are not detectable with NMR. Higher order spins (e.g. spin 3/2 or spin 7/2) are also used but they are more complex than spin 1/2 nuclei. Here, we will not consider high order spins in this work.

The time evolution of a spin-1/2 particle subject to a static magnetic field \vec{B}_0 along the \hat{z} -axis is governed by the Hamiltonian:

$$H_0 = -\mu \cdot B = -\hbar\gamma B_0 I_z = -\hbar\omega_0 I_z = \begin{bmatrix} -\frac{\hbar\omega_0}{2} & 0 \\ 0 & \frac{\hbar\omega_0}{2} \end{bmatrix}, \quad (2.9)$$

where I_x , I_y , and I_z (x , y and z components of the nuclear spin angular momentum operators) relate to the well-known Pauli matrices as:

$$I_x = \frac{1}{2}\sigma_x, \quad I_y = \frac{1}{2}\sigma_y, \quad I_z = \frac{1}{2}\sigma_z, \quad (2.10)$$

where, in matrix symbolism,

$$\sigma_x = \begin{bmatrix} 0 & 1 \\ 1 & 0 \end{bmatrix}, \quad \sigma_y = \begin{bmatrix} 0 & -i \\ i & 0 \end{bmatrix}, \quad \sigma_z = \begin{bmatrix} 1 & 0 \\ 0 & -1 \end{bmatrix}. \quad (2.11)$$

The eigenvalues of Hamiltonian are the energies associated with the different possible states of the spin which are proportional to the eigenvalues of the operator I_z , given by:

$$E_m = -m\hbar\omega_0. \quad (2.12)$$

Therefore, for a nucleus with spin I , there are $2I + 1$ energy levels spaced by the amount $\hbar\omega_0$. Hence, Eqs. (2.9) and (2.12) show that the spin-1/2 has two-discrete energy eigenstates - $|0\rangle$ or $|\uparrow\rangle$ (the spin is aligned with the static magnetic field, i.e. "spin-up" and $m = \frac{1}{2}$) and $|1\rangle$ or $|\downarrow\rangle$ (the spin is anti-aligned with the static magnetic field, i.e. "spin-down" and $m = -\frac{1}{2}$). Furthermore, the $|0\rangle$ state, whose energy is given by $\langle 0|H|0\rangle$, has $\hbar\omega_0$ less energy than the $|1\rangle$ state (the energy of the $|1\rangle$ state is given by $\langle 1|H|1\rangle$), as illustrated in the energy diagram of Fig. (2.3). The energy splitting is known as the Zeeman splitting. The energy separation between the two spin states ("spin-up" and "spin-down") is proportional to the strength of the external magnetic field, and increases as the magnetic field strength is increased (see Fig. (2.4)). In the absence of external magnetic field, these two spin states ("spin-up" and "spin-down") have the same energy.

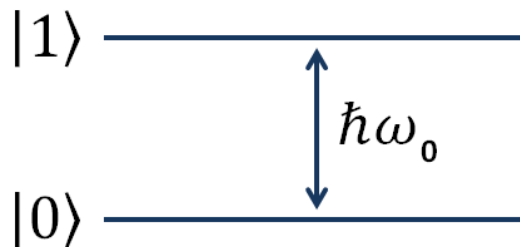


Fig. 2.3: Energy diagram or Zeeman splitting for a spin-1/2 particle subject to a static magnetic field.

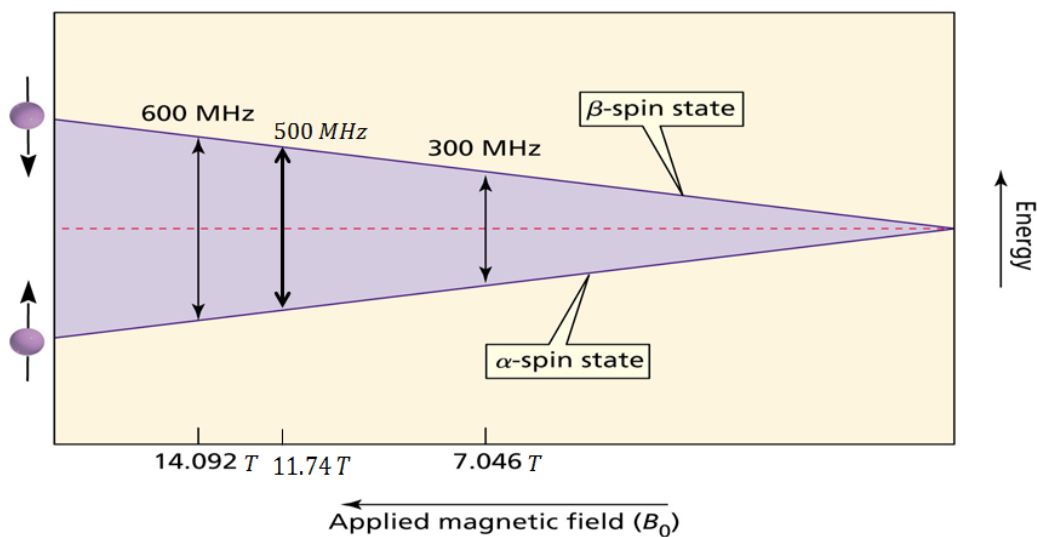


Fig. 2.4: The energy difference between the two spin states depends on the strength of the external magnetic field.

In the case of liquid-state NMR, typical values of the magnetic field B_0 are in the range of 5 – 20 Tesla, resulting in precession frequencies ω_0 of a few hundred MHz , in the radio-frequency range.

Different species of nuclei (or heteronuclear spins) can be spectrally distinguished because they generally have a different gyromagnetic ratio γ , and hence a different Larmor frequency. Table (2.1) summarizes various Larmor frequencies at a magnetic field strength of 11.74 Tesla.

Nucleus	1H	^{13}C	^{15}N	^{19}F	^{31}P
$\omega_0/2\pi$	500	126	-51	470	202

Tab. 2.1: Larmor frequencies [MHz] of several species of nuclei, at 11.74 Tesla.

Spins of the same nuclear species (homonuclear spins) which are part of the same molecule can also have distinct frequencies, by amounts known as their chemical shifts, σ_i (dependent on the chemical environment).

The electron cloud at the nuclei produces a local magnetic field that is in turn affected by the magnetic field B_0 . This local magnetic field causes the change of the resonance frequency in the NMR spectroscopy, referred to as chemical shift. Therefore, the nuclear spin Hamiltonian for a molecule consisting of N uncoupled nuclei can be described by:

$$H_0 = - \sum_{i=0}^N \hbar(1 - \sigma_i)\gamma B_0 I_z^i = - \sum_{i=0}^N \hbar\omega_0^i I_z^i, \quad (2.13)$$

where the i superscripts label the nuclei and σ is known as the chemical shift which, in some cases, can be a tensor quantity.

— SUBSECTION: 2.2.1 —

Interacting Spins

Basically there are two types of interaction between nuclear spins in molecules: magnetic dipole-dipole interaction, and J coupling which are briefly described in the following.

- **Magnetic Dipole-Dipole Interaction:**

Magnetic dipole-dipole interaction looks like the interaction between two bar magnets close to each other. It takes place through space and depends on the internuclear vector \vec{r}_{ij} connecting two nuclei i and j , which is described by the Hamiltonian:

$$H_D = \sum_{i < j} \frac{\mu_0 \gamma_i \gamma_j \hbar}{4\pi |\vec{r}_{ij}|^3} [\vec{I}^i \cdot \vec{I}^j - \frac{3}{|\vec{r}_{ij}|^2} (\vec{I}^i \cdot \vec{r}_{ij})(\vec{I}^j \cdot \vec{r}_{ij})]. \quad (2.14)$$

In this equation, μ_0 is the magnetic permeability of free space and \vec{I}^i is the magnetic moment vector of spin i . It is inversely proportional to the cube of the spatial separation between the two spins, and the relative positioning of the magnetic moment vector of the two spins. Both intramolecular dipolar couplings between spins in the same molecule and intermolecular dipolar couplings between spins in different molecules exist. However,

for molecules in liquid solution, both intramolecular dipolar couplings and intermolecular dipolar couplings are averaged away due to rapid tumbling [6]. This is the case for the samples used in this thesis.

- **J Coupling:**

This interaction is also known as scalar coupling and is mediated through shared electrons in the chemical bond between the nuclei. The nuclear spin interacts with its neighboring electrons. These in turn interact with other neighboring electrons, which can then influence other nuclear spins. In order to obtain strong J-coupling, the nuclear-electron and electron-electron interaction need to be strong. The strength of the J-coupling is furthermore dependent on additional parameters such as the gyromagnetic ratio of the nuclei, and the geometry of the molecule. However, it is independent of the applied magnetic field B_0 and its direction. This interaction is the most important for the application of NMR to quantum information processing.

The Hamiltonian for scalar J-coupling of a molecule containing N spin-1/2 coupled nuclei is given by:

$$H_J = \hbar \sum_{i<j}^N \pi J_{ij} \sigma^i \cdot \sigma^j / 2 = \hbar \sum_{i<j}^N \pi J_{ij} (\sigma_x^i \sigma_x^j + \sigma_y^i \sigma_y^j + \sigma_z^i \sigma_z^j) / 2, \quad (2.15)$$

where J_{ij} is the coupling strength between the spins i and j . Here, the system is said to be strongly coupled. When the frequency separation between the spins is large compared to their coupling strength, i.e. when $2\pi|J_{ij}| \ll |\omega_i - \omega_j|$, we can simplify Eq. (2.15) to [6]:

$$H_J = \hbar \sum_{i<j}^N \pi J_{ij} \sigma_z^i \sigma_z^j / 2. \quad (2.16)$$

When the chemical shift between the nuclei are sufficiently large, this condition is easily satisfied for heteronuclear spins and for small homonuclear molecules. When the condition $|\omega_i - \omega_j| \gg 2\pi J$ applies, the spectra are also said to be first order and the system is said to be weakly coupled.

In summary, the simplest form of a system Hamiltonian of N nuclear spins in an isotropic solution and with first order spectra is given by:

$$H = - \sum_{i=0}^N \hbar \omega_0^i \sigma_z^i / 2 + \hbar \sum_{i < j}^N \pi J_{ij} \sigma_z^i \sigma_z^j / 2. \quad (2.17)$$

The interpretation of this equation is that in addition to the static magnetic field, each spin “sees” another magnetic field along $\pm \hat{z}$ produced by neighbouring spins. The resonance frequency ω_i of each spin i is shifted by $-J_{ij}/2$ when spin j is in the $|0\rangle$ state, and by $+J_{ij}/2$ when spin j is in the $|1\rangle$ state. A molecule with two spins that are coupled with strength J would then have two resonance frequencies for each spin (the frequency spectrum of spin i consists of two lines separated by J_{ij} and centered around ω_0^i). We can associate each with the state of the other spins, either $|0\rangle$ or $|1\rangle$.

The magnitude of the couplings can be measured directly in the spectrum. The coupling strength J can be a few hundred Hertz for coupling through a single bond, and a few Hertz or tenths of Hertz for couplings through three or four bonds. The coupling need not be positive and the relative signs of the couplings can be determined by sequences of pulses as well known as soft-COSY, for example [18].

— SUBSECTION: 2.2.2 —

The Control Hamiltonian

Radio-Frequency Fields

The physical mechanism used to control the NMR system is described in this section. The state of a spin-1/2 particle in a static magnetic field \vec{B}_0 along \hat{z} can be manipulated by applying an electromagnetic field $\vec{B}_1(t)$ which rotates in the $\hat{x} - \hat{y}$ plane at frequency ω_{rf} , at or near the spin precession frequency ω_0 . The single-spin Hamiltonian owing to

the radio frequency (RF) field is given by, similar to Eq. (2.9) for the static field B_0 ,

$$H_{rf} = -\hbar\gamma B_1[\cos(\omega_{rf}t + \phi)I_x - \sin(\omega_{rf}t + \phi)I_y], \quad (2.18)$$

where $\omega_1 = \gamma B_1$ and ϕ is the phase of the RF field, and B_1 its amplitude. Typical values for ω_1 are up to ≈ 50 kHz in liquid state NMR. For N spins, the radio frequency Hamiltonian takes the following form:

$$H_{rf} = -\sum_{i=1}^N \hbar\gamma B_1[\cos(\omega_{rf}t + \phi)I_x^i - \sin(\omega_{rf}t + \phi)I_y^i]. \quad (2.19)$$

In practice, the RF field oscillates along a fixed axis in the laboratory, perpendicular to the static magnetic field. This oscillating field can be decomposed into two counter-rotating fields, one of which rotates at frequency ω_{rf} in the same direction as the spin and so can be set on or near resonance with the spin. The other component rotates in the opposite direction and results in a tiny shift of the Larmor frequency, also known as the Bloch-Siegert shift. We note also that the amplitude B_1 and phase ϕ of the RF field can be varied, as opposed to other parameters such as the Larmor frequency and coupling constants. It has a central role in controlling quantum systems via NMR with techniques such as GRAPE, which will be discussed in Chapter (3).

The Rotating Frame

We can now investigate the evolution of a spin due to the RF field at or near the Larmor frequency ω_0 . The dynamics however are very complicated when described in the laboratory reference frame. A description at a reference frequency that rotates about the \hat{z} axis at frequency ω_{rf} simplifies this picture. This is the *rotating reference frame*.

We can describe the motion of a single nuclear spin in a coordinate system rotating

about \hat{z} at ω_{rf} as:

$$|\psi\rangle^{rot} = \exp(i\omega_{rf}tI_z)|\psi\rangle, \quad (2.20)$$

where $|\psi\rangle$ is the generic state of a single nuclear spin which is a linear combination of the two eigenkets (see section (2)) in the laboratory reference frame. The superscript in the left hand side of the Eq. (2.20) refers to $|\psi\rangle$ in the rotating reference frame.

Substitution of $|\psi\rangle$ in the Schrödinger equation $i\hbar (d|\psi\rangle/dt) = H|\psi\rangle$ with,

$$H = -\hbar\omega_0I_z - \hbar\omega_1[\cos(\omega_{rf}t + \phi)I_x - \sin(\omega_{rf}t + \phi)I_y], \quad (2.21)$$

gives $i\hbar (d|\psi\rangle^{rot}/dt) = H^{rot}|\psi\rangle^{rot}$, where,

$$H^{rot} = -\hbar(\omega_0 - \omega_{rf})I_z - \hbar\omega_1[\cos \phi I_x - \sin \phi I_y]. \quad (2.22)$$

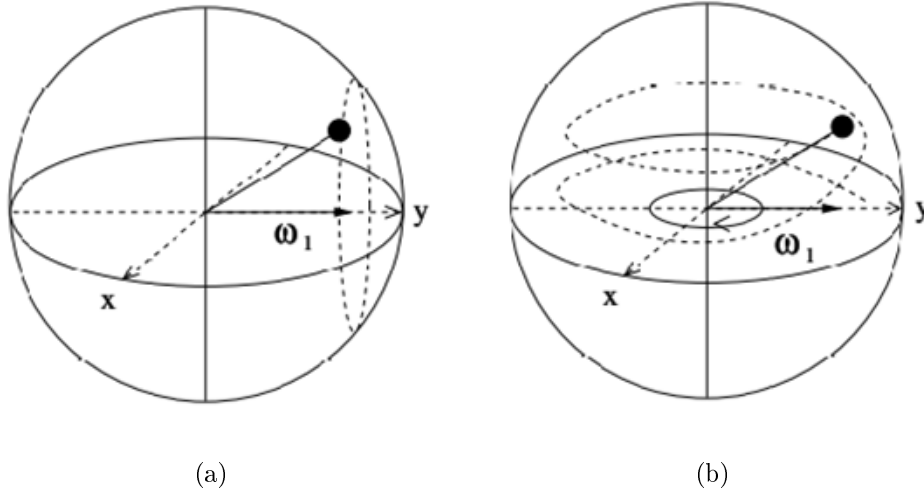


Fig. 2.5: Nutation of a spin subject to a transverse RF field (a) observed in the rotating frame and (b) observed in the laboratory frame.

Naturally, the RF field lies along a fixed axis in the frame rotating at ω_{rf} . Furthermore, if $\omega_{rf} = \omega_0$, the first term in Eq. (2.22) vanishes. In this case, an observer in the rotating frame will see the spin simply precess about \vec{B}_1 (Fig. (2.5(a))), a motion called nutation. The choice of ϕ controls the nutation axis. An observer in the laboratory frame

sees the spin spiral down over the surface of the Bloch sphere (Fig. (2.5(b))).

If the RF field is off-resonance with respect to the spin frequency by $\Delta\omega = \omega_0 - \omega_{rf}$, the spin precesses in the rotating frame about an axis tilted away from the \hat{z} axis by an angle $\alpha = \arctan(\omega_1/\Delta\omega)$, and with frequency $\omega'_1 = \sqrt{(\Delta\omega)^2 + \omega_1^2}$. The RF field has virtually no effect on spins that are far off resonance, since α is very small when $|\Delta\omega| \gg \omega_1$. If all spins have well-separated Larmor frequencies, we can thus in principle selectively rotate any one qubit without rotating the other spins.

In the case of systems with multiple spins where a separate rotating frame are used for each spin and in the presence of multiple RF fields indexed r , the RF Hamiltonian in this multiply rotating frame is given by:

$$H^{rot} = \sum_{i,r} -\hbar\omega_1^r \{ \cos[(\omega_{rf}^r - \omega_0^i)t + \phi^r] I_x^i - \sin[(\omega_{rf}^r - \omega_0^i)t + \phi^r] I_y^i \}, \quad (2.23)$$

where the amplitudes ω_1^r and phases ϕ^r are control parameters.

— SUBSECTION: 2.2.3 —

Relaxation and Decoherence

One important feature of the nuclear spins is its relative isolation from environment, so that the coherence time of the system is high compared with the time scales of the dynamics of the system. Therefore, under good approximation and specific conditions, the dynamics of the NMR system can be considered as an isolated system.

The coupling of the system with the environment is described by an additional Hamiltonian H_{env} , weakly coupled to the system and control Hamiltonian. This coupling leads to decoherence, or the loss of quantum information. In NMR, decoherence is parameterized by two parameters: T_1 , connected to the system energy loss to the environment and

T_2 connected to the loss of coherence of the system.

1. **Longitudinal Relaxation** (or T_1 relaxation)

Thermal equilibrium is a state in which the population of α - and β -states (for a spin-1/2 system α and β refer to $m = \frac{1}{2}$ and $m = -\frac{1}{2}$, respectively) corresponds to the Boltzmann distribution. Furthermore, the spins are uncorrelated in phase such that no transverse magnetization exists. However, when RF pulses are applied the state of the spins is pertubated away from equilibrium distributions and longitudinal relaxation describes the return of the z-component magnetization to its equilibrium value, or, equivalently, return of the populations of the energy levels of the spin system (diagonal elements of the density operator) to the equilibrium Boltzmann distribution. The longitudinal or spin-lattice relaxation time constant is called T_1 . Typical values for T_1 range from milliseconds to several seconds although T_1 may be as long as days or even months in exceptional cases.

2. **Transverse Relaxation** (or T_2 relaxation)

Transverse relaxation describes the decay of transverse (x, y) magnetization to zero, or equivalently, the decay of transverse quantum coherences (off-diagonal elements of the density matrix). Analogously, the transverse or spin-spin relaxation time constant is called T_2 . Typical values for T_2 range from milliseconds to several seconds.

A final requirement for implementing QIP using liquid-state NMR is to have qubits which maintain quantum coherence. We thus need a system where the time to implement quantum gates is significantly shorter than the decoherence time of the system. The low energies of nuclear spins naturally decouples them from other degrees of freedom, hence isolating them well. The only decoherence present in NMR arises from interaction with the other spins or by energy exchange with the surroundings. In liquid state NMR, these processes are associated with loss of coherence on the order 100's of ms to seconds, while

the longest quantum gates can be implemented on the order of 10's of ms. These competing timescales allow us to implement a lot of gates before decoherence affects the system, significantly.

SECTION: 2.3

Quantum Bits

A quantum bit, or qubit, is simply a two level quantum system, labeled as $|0\rangle$ and $|1\rangle$, effectively identifying them with the two logical states 0 and 1. This choice is usually called the computational basis. In NMR, the qubits are spin-1/2 nuclei in a molecule. Spin-1/2 nucleus has exactly two orthogonal states. For the case of spin-1/2 particle, the logical state 0 can be represented by the spin up state ($|0\rangle \equiv |\uparrow\rangle$), whereas the logical state 1 can be represented by the spin down state ($|1\rangle \equiv |\downarrow\rangle$). Obviously, systems with N spins-1/2 are N -qubit systems.

Unlike to the case of classical bits in which only two states, 0 and 1, can exist, the quantum bit can be in any superposition of the computational basis of the form:

$$|\psi\rangle = \alpha|0\rangle + \beta|1\rangle, \quad (2.24)$$

where α and β are arbitrary complex numbers related to each other by the constraint $|\alpha|^2 + |\beta|^2 = 1$ in order for $|\psi\rangle$ to be correctly normalized. $|\alpha|^2$ and $|\beta|^2$ indicate probabilities of measuring spin up and spin down, respectively. The state $|\psi\rangle$ can in this case be written as a column vector consisting of two entries, α and β .

One particularly important pair of superposition states is $|+\rangle$ and $|-\rangle$, defined by:

$$|\pm\rangle = \frac{|0\rangle \pm |1\rangle}{\sqrt{2}}, \quad (2.25)$$

which play a key role in many quantum algorithms.

We can multiply an arbitrary $|\psi\rangle$ by any phase factor without loss of generality because this overall phase is unmeasurable, so we can write $|\psi\rangle$ as:

$$|\psi\rangle = \cos(\theta/2)|0\rangle + e^{-i\phi} \sin(\theta/2)|1\rangle, \quad (2.26)$$

where $\alpha = \cos(\theta/2)$, $\beta = e^{-i\phi} \sin(\theta/2)$ and the variables θ and ϕ are real numbers.

Visually, this state can be represented on the Bloch sphere as shown in Fig. (2.6). This picture will help us understand the dynamics of nuclear spins in the context of NMR quantum computing. The Bloch sphere allows us to visualize the state of a single qubit in a three-dimensional space. A qubit can exist on any point on the surface of the Bloch sphere. This sketch is very useful for visualizing single qubit quantum states but for multiple qubits, this picture may not even hold in general.

The state of a qubit is the unit radius vector extending outwards the origin of an x, y, z three-dimensional space. The direction of the vector is defined by the two angles, θ and ϕ . The angle θ is the rotation of the vector from the z axis and the angle ϕ is the rotation from the x axis on the xy plane. The Bloch sphere is the three-dimensional shape formed by varying θ and ϕ over all possible values ($0 \leq \theta \leq \pi$ and $0 \leq \phi \leq 2\pi$).

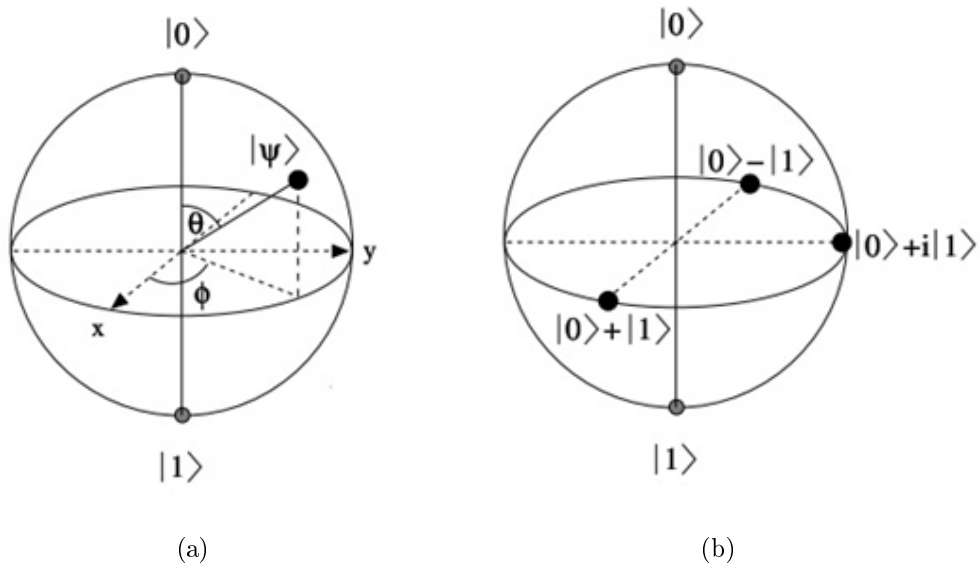


Fig. 2.6: (a) Bloch sphere representation of an arbitrary quantum state $|\psi\rangle$ for a single qubit. (b) Representation of several important quantum states, ignoring the normalization factor.

Later, we will discuss single qubit operators such as the σ_x , σ_y , and σ_z rotation gates. Fundamentally, all qubit operators cause the state vector on the Bloch sphere to rotate to another point on the sphere.

A system of a single qubit is hardly interesting, but even a two qubit system or systems with more than one qubit can show interesting computational behaviour. A system of two qubits, for example, has four computational basis states, and can be found in a arbitrary superposition of all four,

$$|\psi\rangle = \alpha|00\rangle + \beta|01\rangle + \gamma|10\rangle + \delta|11\rangle, \quad (2.27)$$

where $|00\rangle$ is the short hand notation for $|0\rangle \otimes |0\rangle$, \otimes is the tensor product or Kronecker product symbol, and the coefficients $\alpha, \beta, \gamma, \delta$ satisfy the normalization condition $|\alpha|^2 + |\beta|^2 + |\gamma|^2 + |\delta|^2 = 1$. Two qubits can exist in four states at the same time, and $|\psi\rangle$ is given by a column vector of four entries.

For N qubits, a general quantum state $|\psi\rangle$ can be described as:

$$|\psi\rangle = \sum_{i=0}^{2^N-1} c_i |i\rangle, \quad (2.28)$$

where i is the decimal (instead of binary) representation, and the c_i satisfy the normalization condition $\sum_{i=0}^{2^N-1} |c_i|^2 = 1$. Describing the pure state of N qubits thus requires 2^N complex numbers. This is in contrast to the description of N classical bits which only requires a number of complex numbers linear in N .

Entanglement

The N qubit state $|\psi\rangle$ can sometimes be written as a Kronecker product of several individual qubit states:

$$|\psi\rangle = \otimes_{i=1}^N |\psi_i\rangle, \quad (2.29)$$

where $|\psi_i\rangle$, the state of the i -th qubit, is of the form of Eq. (2.26) and $\otimes_{i=1}^N$ represents the N Kronecker products of the states $|\psi_i\rangle$. If this equation holds, then each qubit can be represented on the Bloch sphere, similar to Fig. (2.6). Thus we only require a number of complex numbers linear in N to describe the N pure qubits, similar to N classical bits. Such a quantum state is therefore also known as a separable state. For example, the two qubit states can be divided into two classes of states, said separable states, which can be decomposed into a tensor product of individual states of each system, as the state $|\psi\rangle = (|00\rangle + |01\rangle + |10\rangle + |11\rangle)/2 = [(|0\rangle + |1\rangle)/\sqrt{2}] \otimes [(|0\rangle + |1\rangle)/\sqrt{2}]$.

If $|\psi\rangle$ cannot be written into the product form of Eq. (2.29), then the two qubits are said to be entangled. For example, states $|\phi_{\pm}\rangle = (|00\rangle \pm |11\rangle)/\sqrt{2}$ and $|\psi_{\pm}\rangle = (|01\rangle \pm |10\rangle)/\sqrt{2}$ are maximally entangled states, which form the important two-qubit Bell states or EPR states. The two qubits are correlated because the measurement of one qubit directly affects the state of the other qubit. Unentangled qubits may each be

represented on a Bloch sphere. Entanglement however cannot easily be visually represented. Instead, the state is mathematically described in Hilbert space, a 2^N -dimensional complex vector space.

— SUBSECTION: 2.3.1 —

Mixed States and The Density Operator

The above description of the possible states of a qubit requires preparation of perfect pure states. However, this situation is only an idealization due to experimental limitations. One way to deal with this situation is introducing non-pure states, or statistical mixtures (or mixed states). The state of a quantum system in a statistical mixture is conveniently described by its density operator:

$$\rho = \sum_i p_i |\psi_i\rangle\langle\psi_i|, \quad (2.30)$$

where $\langle\psi|$ represents the Hermitian conjugate of $|\psi\rangle$, and $|\psi\rangle\langle\psi|$ denotes the outer product (a linear operator). Obviously, the probabilities p_i must satisfy $p_i \geq 0$ and $\sum_i p_i = 1$. The density operator of a pure state $|\psi\rangle$ is then just $\rho = |\psi\rangle\langle\psi|$.

The density operator also has two important characteristics:

$$\text{Tr}(\rho) = 1, \quad (2.31)$$

because $\text{Tr}(\rho) = \sum_i p_i \text{Tr}(|\psi_i\rangle\langle\psi_i|) = \sum_i p_i = 1$. This is also known as the trace condition. Furthermore, the density operator is a positive operator because $\langle\phi|\rho|\phi\rangle \geq 0$ where $|\phi\rangle$ is any other quantum state. Therefore, the density operator must have some spectral decomposition into a set of orthogonal states:

$$\rho = \sum_k \lambda_k |k\rangle\langle k|, \quad (2.32)$$

where λ_k are the real-valued eigenvalues of ρ and $|k\rangle$ are orthogonal (the $|\psi\rangle$ above need not be orthogonal). Since a pure state has only one eigenvalue, necessarily equal to unity, and a mixed state has several eigenvalues, we can derive a very useful condition which allows us to distinguish between mixed and pure states:

$$\text{Tr}(\rho^2) = 1 \rightarrow \text{When } \rho \text{ is pure,}$$

$$\text{Tr}(\rho^2) < 1 \rightarrow \text{When } \rho \text{ is mixed.}$$

The density matrix formalism can also be mapped to the Bloch sphere picture by writing a density operator as:

$$\rho = \frac{I + \vec{r} \cdot \vec{\sigma}}{2}, \quad (2.33)$$

where $\vec{\sigma} = \sigma_x \hat{x} + \sigma_y \hat{y} + \sigma_z \hat{z}$ and $\sigma_x, \sigma_y, \sigma_z$ are Pauli matrices and \vec{r} is a real three-dimensional vector with $\|\vec{r}\| \leq 1$. Pure states have $\|\vec{r}\| = 1$ and mixed states have $\|\vec{r}\| < 1$.

A mixed state is a manifestation of the lack of knowledge about the quantum system or ensemble of quantum systems.

SECTION: 2.4

Quantum Gates

Quantum logic gates are unitary transformations which implement some desired logic operation on qubits. Thus, with respect to the control of quantum systems, the goal is the implementation of a unitary transformation on the qubits, U , which can be decomposed into a sequence of unitary transformations, $U = U_k U_{k-1} \dots U_2 U_1$. It has long been known that NMR can be used to implement any desired unitary evolution, including quantum logic gates. In this section we describe a set of unitary gates with which we can construct any arbitrary quantum circuit.

A very useful result from classical information theory is that any operation can be decomposed into a set of gates for example AND, OR and NOT gates, which is known as a universal set of gates. The NAND and NOR gates are universal, and also form a universal set.

Similar to the classical case, there also exists a set of universal gates for quantum computation. Any arbitrary unitary operation can be approximated to arbitrary extent from a finite universal set of quantum gates. Arbitrary single qubit operations and Controlled-NOT (CNOT) gate form a universal set of quantum gates.

— SUBSECTION: 2.4.1 —

Single Qubit Gates

Single qubit gates are defined by 2×2 matrices and represent the simplest quantum logical operations. At first, we introduce a convenient matrix representation to describe quantum states and unitary transformations. The quantum state $|\psi\rangle = \alpha|0\rangle + \beta|1\rangle$ is written in matrix notation as:

$$|\psi\rangle = \begin{bmatrix} \alpha \\ \beta \end{bmatrix}, \quad (2.34)$$

where $|\psi\rangle$ is a column vector of two entries, α and β which are the amplitudes of the $|0\rangle$ and $|1\rangle$ states respectively and $|\alpha|^2 + |\beta|^2 = 1$. The matrix representation of $\langle\psi|$ is then just a row vector with the same entries, but taking their complex conjugates:

$$\langle\psi| = [\alpha^* \ \beta^*]. \quad (2.35)$$

In general, any single qubit rotation takes the form:

$$U = e^{i\alpha} R_{\hat{n}}(\theta), \quad (2.36)$$

where $R_{\hat{n}}(\theta)$ corresponds to a rotation of the state vector $|\psi\rangle$ on the Bloch sphere in Fig.

(2.6) around the axis $n = (n_x, n_y, n_z)$ over an angle θ . Mathematically, we can define $R_{\hat{n}}(\theta)$ as:

$$R_{\hat{n}}(\theta) = \exp\left(-i\frac{\theta\hat{n}\cdot\vec{\sigma}}{2}\right) = \cos\left(\frac{\theta}{2}\right) I - i\sin\left(\frac{\theta}{2}\right) [n_x \sigma_x + n_y \sigma_y + n_z \sigma_z], \quad (2.37)$$

where $\vec{\sigma} = (\sigma_x, \sigma_y, \sigma_z)$, with $\sigma_x, \sigma_y, \sigma_z$ denoting the Pauli matrices and I the identity matrix:

$$\sigma_x = \begin{bmatrix} 0 & 1 \\ 1 & 0 \end{bmatrix}, \quad \sigma_y = \begin{bmatrix} 0 & -i \\ i & 0 \end{bmatrix}, \quad \sigma_z = \begin{bmatrix} 1 & 0 \\ 0 & -1 \end{bmatrix}, \quad I = \begin{bmatrix} 1 & 0 \\ 0 & 1 \end{bmatrix}. \quad (2.38)$$

The Pauli matrices satisfy the following useful relationships:

$$\sigma_x \sigma_y = i\sigma_z, \quad \sigma_y \sigma_z = i\sigma_x, \quad \sigma_z \sigma_x = i\sigma_y, \quad \sigma_x^2 = \sigma_y^2 = \sigma_z^2 = 1. \quad (2.39)$$

In the Bloch sphere, there are three axes (\hat{x}, \hat{y} and \hat{z}) and thus three important single qubit rotations (the \hat{x}, \hat{y} and \hat{z} -rotations). These are given by:

$$R_{\hat{x}}(\theta) = \exp\left(\frac{-i\theta\sigma_x}{2}\right) = \cos\left(\frac{\theta}{2}\right) I - i\sin\left(\frac{\theta}{2}\right) \sigma_x = \begin{bmatrix} \cos\left(\frac{\theta}{2}\right) & -i\sin\left(\frac{\theta}{2}\right) \\ -i\sin\left(\frac{\theta}{2}\right) & \cos\left(\frac{\theta}{2}\right) \end{bmatrix}, \quad (2.40)$$

$$R_{\hat{y}}(\theta) = \exp\left(\frac{-i\theta\sigma_y}{2}\right) = \cos\left(\frac{\theta}{2}\right) I - i\sin\left(\frac{\theta}{2}\right) \sigma_y = \begin{bmatrix} \cos\left(\frac{\theta}{2}\right) & -\sin\left(\frac{\theta}{2}\right) \\ \sin\left(\frac{\theta}{2}\right) & \cos\left(\frac{\theta}{2}\right) \end{bmatrix}, \quad (2.41)$$

$$R_{\hat{z}}(\theta) = \exp\left(\frac{-i\theta\sigma_z}{2}\right) = \cos\left(\frac{\theta}{2}\right) I - i\sin\left(\frac{\theta}{2}\right) \sigma_z = \begin{bmatrix} e^{-i\theta/2} & 0 \\ 0 & e^{i\theta/2} \end{bmatrix}. \quad (2.42)$$

We can define the general single qubit operator as the product of the rotation operations by first rotating over \hat{x} , then \hat{y} , and lastly \hat{z} . To achieve this, we can write any U with the global phase term as:

$$U = e^{-i\alpha} R_{\hat{z}}(\beta) R_{\hat{y}}(\gamma) R_{\hat{x}}(\delta). \quad (2.43)$$

We actually do not require the ability to perform explicit \hat{z} -rotations because we can generate them from \hat{x} and \hat{y} rotations:

$$R_{\hat{z}}(\beta) = R_{\hat{x}}(90^\circ) R_{\hat{y}}(\beta) R_{\hat{x}}(-90^\circ) = R_{\hat{y}}(-90^\circ) R_{\hat{x}}(\beta) R_{\hat{y}}(90^\circ), \quad (2.44)$$

where time goes from right to left (i.e. $R_{\hat{x}}(-90^\circ)$ or $R_{\hat{y}}(90^\circ)$ is applied first). Thus, arbitrary \hat{x} and \hat{y} rotations are sufficient to implement any arbitrary single qubit rotation. Now we can review some of the common single qubit operators.

The NOT or X Gate:

This is sometimes called the Pauli X gate (or Pauli σ_x gate and for convenience, we show it by X). It maps $|0\rangle$ onto $|1\rangle$ and vice-versa, similar to classical inversion. The unitary matrix which effects this transformation for arbitrary input states is:

$$U_{NOT} = X = \begin{bmatrix} 0 & 1 \\ 1 & 0 \end{bmatrix}. \quad (2.45)$$

The Y Gate:

The Pauli Y gate (or Pauli σ_y gate and for convenience, we show it by Y) performs the following mapping on the logical states:

$$Y|0\rangle = i|1\rangle, \quad Y|1\rangle = -i|0\rangle. \quad (2.46)$$

So, the unitary matrix takes this form:

$$Y = \begin{bmatrix} 0 & -i \\ i & 0 \end{bmatrix}. \quad (2.47)$$

The Z Gate:

The Pauli Z gate (or Pauli σ_z gate and for convenience, we show it by Z) performs these

mapping on the logical gates:

$$Z|0\rangle = |0\rangle, \quad Z|1\rangle = -|1\rangle. \quad (2.48)$$

This gate just changes the relative phase factor by -1 and its matrix is:

$$Z = \begin{bmatrix} 1 & 0 \\ 0 & -1 \end{bmatrix}. \quad (2.49)$$

The Phase or S Gate:

The Phase (or S) gate performs the following mapping on the logical states:

$$S|0\rangle = |0\rangle, \quad S|1\rangle = i|1\rangle. \quad (2.50)$$

The matrix is defined as:

$$S = \begin{bmatrix} 1 & 0 \\ 0 & i \end{bmatrix}. \quad (2.51)$$

The $\pi/8$ or T Gate:

The T gate is defined by the matrix:

$$T = \begin{bmatrix} 1 & 0 \\ 0 & e^{i\pi/4} \end{bmatrix}. \quad (2.52)$$

The Hadamard Gate:

A important single qubit gate is the HADAMARD gate, defined as:

$$H = \frac{1}{\sqrt{2}} \begin{bmatrix} 1 & 1 \\ 1 & -1 \end{bmatrix}. \quad (2.53)$$

The Hadamard gate is extremely useful because it maps the basis states $|0\rangle$ and $|1\rangle$

into a superposition of the two states with equal weight. That is:

$$|0\rangle \Rightarrow (|0\rangle + |1\rangle)/\sqrt{2}, \quad |1\rangle \Rightarrow (|0\rangle - |1\rangle)/\sqrt{2}. \quad (2.54)$$

We can describe these single qubit rotations and single qubit gates via the quantum circuit language, first introduced by Deutsch and shown in Fig. (2.7). The horizontal wires denote the individual qubits, and time goes from left to right.

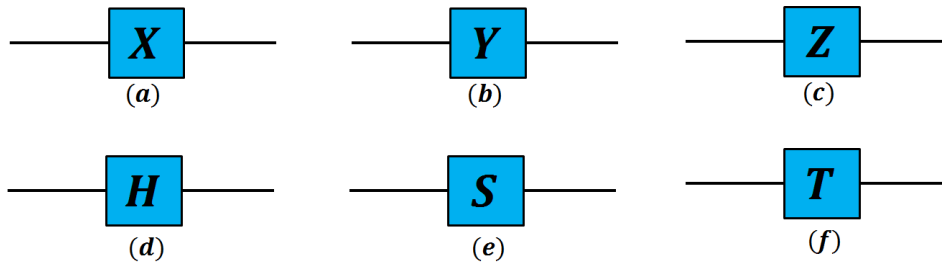


Fig. 2.7: Quantum circuit representation of (a) the X gate, (b) the Y gate, (c) the Z gate, (d) the Hadamard gate, (e) the S gate and, (f) the T gate.

As we have shown, single qubit rotations can be generated by Pauli matrices. But when we have n multiple qubits and wish to apply only a single qubit operation around \hat{n} on qubit i , we denote this rotation by $R_n^i(\theta)$. This rotation can be generated by a concatenation of Pauli matrices σ_k^i where k is either x, y or z and σ_k^i is the short hand notation for n -fold Kronecker product of I matrices (Identity matrix) expect for the i -th location, where we have σ_k . For example, when we have three qubits and wish to apply a single qubit \hat{x} rotation on qubit three, then:

$$R_x^3(\theta) = \exp(-i \frac{\theta(I \otimes I \otimes \sigma_x)}{2}) = \exp(-i \frac{\theta(IIX)}{2}), \quad (2.55)$$

where IIX is just the short-hand notation for $I \otimes I \otimes \sigma_x$ and I is the 2×2 identity matrix.

Implementation of Single-Qubit Gates

Rotations on single qubits can be implemented directly in the rotating frame using RF pulses. From the control Hamiltonian, Eq. (2.18), it follows that when an RF field of amplitude ω_1 is applied to a single-spin system at $\omega_{rf} = \omega_0$, the spin evolves under the transformation:

$$U = \exp[i\omega_1 (\cos \phi I_x - \sin \phi I_y) t_{pw}], \quad (2.56)$$

where t_{pw} is the pulse width (or pulse length), the time duration of the RF pulse. U describes a rotation in the Bloch sphere over an angle θ proportional to the product of t_{pw} and $\omega_1 = \gamma B_1$, and about an axis in the $\hat{x} - \hat{y}$ plane determined by the phase ϕ .

Thus a pulse with phase $\phi = \pi$ and $\omega_1 t_{pw} = \pi/2$ will perform $R_x(90^\circ)$, which is a 90° rotation about \hat{x} , denoted for short as X . A similar pulse but twice as long realizes a $R_x(180^\circ)$ rotation, written for short as X^2 . By changing the phase of the RF pulse to $\phi = \pi/2$, Y and Y^2 pulses can similarly be implemented.

The Hadamard gate transforms the computational basis states into the uniform superposition of states, and back (time goes from right to left):

$$H = R_{\hat{x}}(180^\circ) R_{\hat{y}}(90^\circ) = R_{\hat{y}}(90^\circ) R_{\hat{z}}(180^\circ). \quad (2.57)$$

The pulse sequence for implementation of some single quantum gates are as following:

$$X \text{ Gate} \Rightarrow R_{\hat{x}}(180^\circ), \quad (2.58)$$

$$Y \text{ Gate} \Rightarrow R_{\hat{y}}(180^\circ), \quad (2.59)$$

$$Z \text{ Gate} \Rightarrow R_{\hat{x}}(-90^\circ) \rightarrow R_{\hat{y}}(180^\circ) \rightarrow R_{\hat{x}}(90^\circ), \quad (2.60)$$

$$S \text{ Gate} \Rightarrow R_{\hat{x}}(-90^\circ) \rightarrow R_{\hat{y}}(90^\circ) \rightarrow R_{\hat{x}}(90^\circ), \quad (2.61)$$

$$T \text{ Gate} \Rightarrow R_{\hat{x}}(-90^\circ) \rightarrow R_{\hat{y}}(45^\circ) \rightarrow R_{\hat{x}}(90^\circ). \quad (2.62)$$


SUBSECTION: 2.4.2

Two-Qubit Gates

Two-qubit quantum gates have two inputs and can operate on one or two qubits. The most important two-qubit gate is the CNOT (Controlled-NOT) gate. The CNOT gate is an X gate operating on one qubit but controlled by the other qubit. The operations of the CNOT gate with the first qubit as control on the logic basis states are:

$$\begin{aligned} \text{CNOT} |00\rangle &= |00\rangle, & \text{CNOT} |01\rangle &= |01\rangle, \\ \text{CNOT} |10\rangle &= |11\rangle, & \text{CNOT} |11\rangle &= |10\rangle. \end{aligned} \quad (2.63)$$

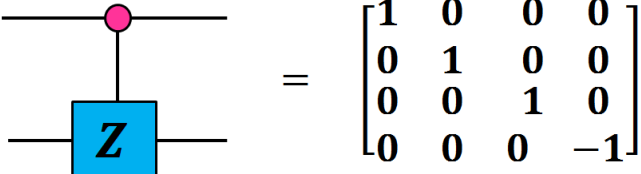
The circuit and the unitary matrix for the *CNOT* gate are then:



$$\text{CNOT} = \begin{bmatrix} 1 & 0 & 0 & 0 \\ 0 & 1 & 0 & 0 \\ 0 & 0 & 0 & 1 \\ 0 & 0 & 1 & 0 \end{bmatrix}. \quad (2.64)$$

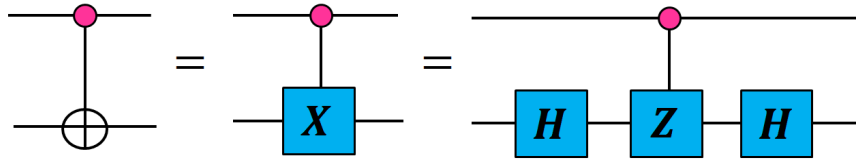
This gate inverts the target qubit (represented in the second line of the above circuit) if and only if the control qubit (the first qubit) is in state $|1\rangle$.

In NMR experiments, however, the key two-qubit gate is the Controlled-Z gate:



$$= \begin{bmatrix} \mathbf{1} & \mathbf{0} & \mathbf{0} & \mathbf{0} \\ \mathbf{0} & \mathbf{1} & \mathbf{0} & \mathbf{0} \\ \mathbf{0} & \mathbf{0} & \mathbf{1} & \mathbf{0} \\ \mathbf{0} & \mathbf{0} & \mathbf{0} & -\mathbf{1} \end{bmatrix}$$

which is easily converted to a Controlled-NOT gate:



with the application of a pair of Hadamard gates.

Controlled-Z can be easily decomposed as a product operator:

$$\text{Controlled-Z} = \exp[-i(\pi/2)(-\frac{1}{2}I + I_z^1 + I_z^2 - 2I_z^1 I_z^2)], \quad (2.65)$$

where the $\frac{1}{2}I$ term is just a global phase, and can be ignored as usual and I_z^1 is the z-component of the first spin and I_z^2 is the z-component of the second spin. Terms I_z^1 and I_z^2 are just single qubit rotations, and can be implemented with single-qubit gates. The term $2I_z^1 I_z^2$ corresponds to evolution under the spin-spin coupling term, $2\pi J I_z^1 I_z^2$ for a time $1/2J$.

There are several extensions of the *CNOT* gates, one important two-qubit gate is the SWAP gate, which swaps two qubits, i.e. $00 \mapsto 00$, $01 \mapsto 10$, $10 \mapsto 01$, and $11 \mapsto 11$. This gate can be entirely constructed out of three *CNOT* gates:

$$\text{SWAP}_{12} = \text{CNOT}_{12} \text{CNOT}_{21} \text{CNOT}_{12}, \quad (2.66)$$

where CNOT_{ij} is the Controlled-NOT gate with the qubit i as control and the qubit j as target. Besides the *CNOT*, we can in fact implement any controlled U operation. The quantum circuits representation for a few two-qubit gates are shown in Fig. (2.8).

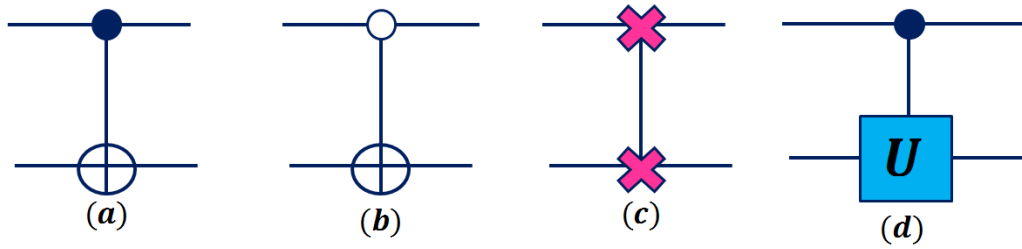


Fig. 2.8: quantum circuit representation of (a) a Controlled-NOT gate, (b) a Zero-Controlled-NOT, (c) a SWAP gate, and (d) a Controlled-U gate. The \bullet symbol denotes the control qubit- the controlled operation is only executed if the qubit is in the $|1\rangle$ state. The \circ symbol denotes the Zero-Controlled qubit, i.e. the operation is only executed if the control qubit is in the state $|0\rangle$.

As we mentioned, if we have some sequence of individual unitary evolutions applied one after another, the overall resulting unitary evolution can be calculated as:

$$U = U_i U_{i-1} U_{i-2} \dots U_2 U_1. \quad (2.67)$$

The first unitary gate that we should apply, U_1 , must be on the right hand side and the last, U_i , on the left. The order is important since in general:

$$U_1 U_2 \neq U_2 U_1. \quad (2.68)$$

That is, in general, two unitary operators may not commute under multiplication.

Implementation of Two-Qubit Gates

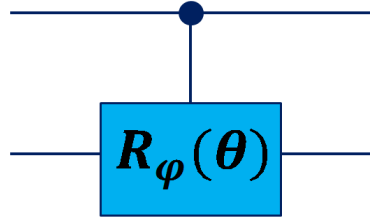
A possible pulse sequences for the $CNOT_{12}$, $CNOT_{21}$ and $SWAP$ gates respectively are (time goes from right to left):

$$CNOT_{12} = R_z^1(90^\circ) R_z^2(-90^\circ) R_x^2(90^\circ) U_J(1/2J) R_y^2(90^\circ), \quad (2.69)$$

$$CNOT_{21} = R_z^2(90^\circ) R_z^1(-90^\circ) R_x^1(90^\circ) U_J(1/2J) R_y^1(90^\circ), \quad (2.70)$$

$$\begin{aligned} SWAP = & R_y^2(90^\circ) R_z^2(-270^\circ) R_z^1(-270^\circ) U_J(1/2J) R_y^2(90^\circ) \\ & R_y^1(-90^\circ) U_J(1/2J) R_x^1(90^\circ) R_x^2(-90^\circ) U_J(1/2J) R_y^2(-90^\circ). \end{aligned} \quad (2.71)$$

Another important gate is *Controlled-Phase* gate. This gate can be obtained through the following pulse sequence:



$$Controlled - Phase = R_y^2(90^\circ) R_x^2(180^\circ) U_J\left(\frac{\theta}{2\pi J}\right) R_x^2(180^\circ) R_z^1(90^\circ) R_z^2(90^\circ) R_y^2(90^\circ). \quad (2.72)$$

SUBSECTION: 2.4.3

Three-Qubit Gates

Three qubit gates have three inputs and three outputs, and are described by 8×8 square unitary matrices. Common examples of three qubit gates that we will cover in more detail are Toffoli and Fredkin gates. These are the same gates that we have used in this thesis (see chapter (6)).

The state of the three qubit gates can be written as the linear superposition of its 8 computational basis states as:

$$\begin{aligned}
 |\psi\rangle = & c_0|000\rangle + c_1|001\rangle + c_2|010\rangle + c_3|011\rangle + c_4|100\rangle + \\
 & c_5|101\rangle + c_6|110\rangle + c_7|111\rangle,
 \end{aligned}
 \tag{2.73}$$

where $\sum_{i=0}^7 |c_i|^2 = 1$.

The Fredkin Gate:

The Fredkin gate has one control input and two target qubits. It is essentially the Controlled-SWAP gate. When the control qubit is asserted, the target qubits are swapped. The quantum circuit of a Fredkin gate is shown in Fig. (2.9) where the control is a and target qubits are b and c .

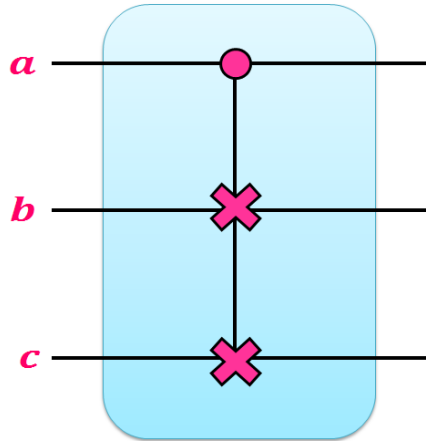


Fig. 2.9: quantum circuit representation of a Fredkin gate with qubits a as control and qubits b and c as targets.

The operations of the Fredkin gate on the logic basis states are:

$$\begin{aligned}
 |000\rangle & \rightarrow |000\rangle, & |100\rangle & \rightarrow |100\rangle, \\
 |001\rangle & \rightarrow |001\rangle, & |101\rangle & \rightarrow |110\rangle, \\
 |010\rangle & \rightarrow |010\rangle, & |110\rangle & \rightarrow |101\rangle, \\
 |011\rangle & \rightarrow |011\rangle, & |111\rangle & \rightarrow |111\rangle.
 \end{aligned}
 \tag{2.74}$$

Therefore, the unitary matrix of the Fredkin gate is given by:

$$Fredkin = \begin{bmatrix} 1 & 0 & 0 & 0 & 0 & 0 & 0 & 0 \\ 0 & 1 & 0 & 0 & 0 & 0 & 0 & 0 \\ 0 & 0 & 1 & 0 & 0 & 0 & 0 & 0 \\ 0 & 0 & 0 & 1 & 0 & 0 & 0 & 0 \\ 0 & 0 & 0 & 0 & 1 & 0 & 0 & 0 \\ 0 & 0 & 0 & 0 & 0 & 1 & 0 & 0 \\ 0 & 0 & 0 & 0 & 0 & 0 & 1 & 0 \\ 0 & 0 & 0 & 0 & 0 & 0 & 0 & 1 \end{bmatrix}. \quad (2.75)$$

The Toffoli Gate:

The Toffoli gate is also known as the Controlled-CNOT gate because it is literally a CNOT gate with a secondary control input. The function is if both control inputs are asserted, the target qubit is inverted. Fig. (2.10) shows a circuit diagram of the quantum Toffoli gate with qubits a and b as controls and qubit c as target.

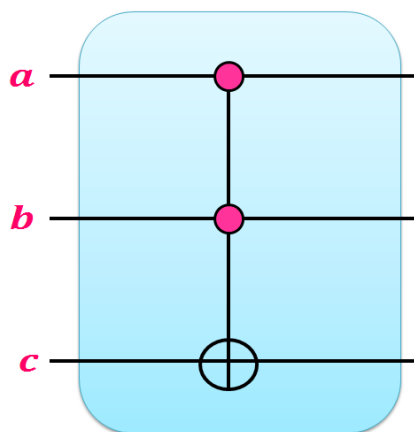


Fig. 2.10: quantum circuit representation of a Toffoli gate with qubits a and b as controls and qubit c as target.

The operations of the Toffoli gate on the logic basis states are:

$$\begin{aligned}
 |000\rangle &\rightarrow |000\rangle, & |100\rangle &\rightarrow |100\rangle, \\
 |001\rangle &\rightarrow |001\rangle, & |101\rangle &\rightarrow |101\rangle, \\
 |010\rangle &\rightarrow |010\rangle, & |110\rangle &\rightarrow |111\rangle, \\
 |011\rangle &\rightarrow |011\rangle, & |111\rangle &\rightarrow |110\rangle.
 \end{aligned} \tag{2.76}$$

Therefore, the unitary matrix of the Toffoli gate is given by:

$$Toffoli = \begin{bmatrix} 1 & 0 & 0 & 0 & 0 & 0 & 0 & 0 \\ 0 & 1 & 0 & 0 & 0 & 0 & 0 & 0 \\ 0 & 0 & 1 & 0 & 0 & 0 & 0 & 0 \\ 0 & 0 & 0 & 1 & 0 & 0 & 0 & 0 \\ 0 & 0 & 0 & 0 & 1 & 0 & 0 & 0 \\ 0 & 0 & 0 & 0 & 0 & 1 & 0 & 0 \\ 0 & 0 & 0 & 0 & 0 & 0 & 0 & 1 \\ 0 & 0 & 0 & 0 & 0 & 0 & 1 & 0 \end{bmatrix}. \tag{2.77}$$

Implementation of Three-Qubit Gates

A possible and minimum pulse sequences for the Fredkin and Toffoli gates respectively are shown in Figs. (2.11) and(2.12).

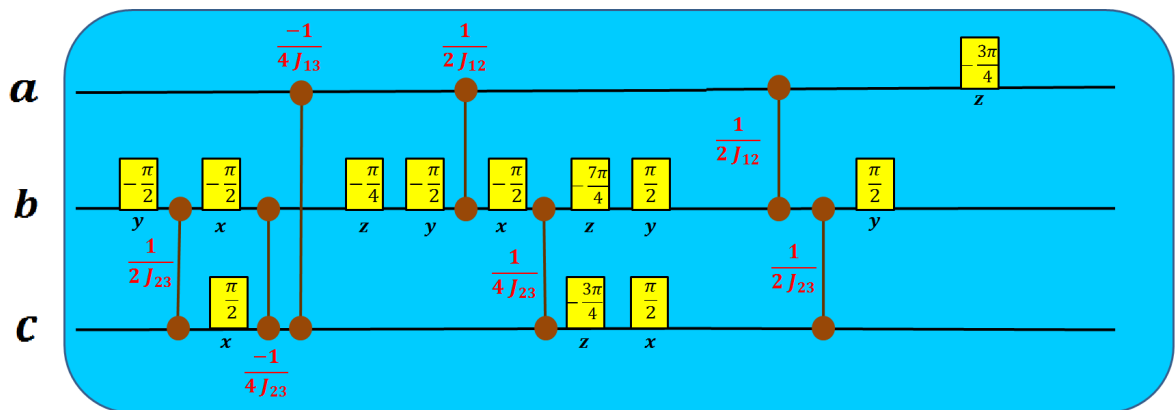


Fig. 2.11: Minimum pulse sequences for the Fredkin with qubits a as control and qubits b and c as targets. Time goes from left to right.

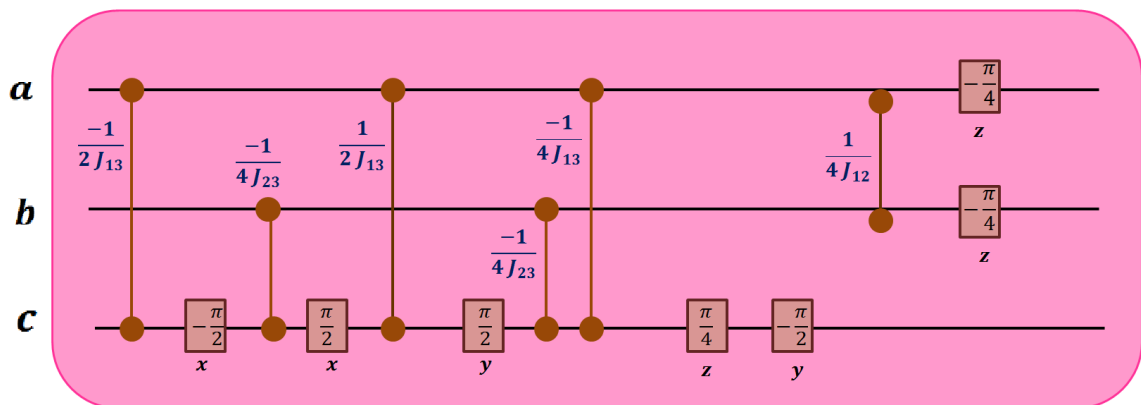


Fig. 2.12: Minimum pulse sequences for the Toffoli with qubits a and b as controls and qubit c as target. Time goes from left to right.

Now, in Figs. (2.13) and (2.14), we have shown some single and two qubit circuits that they share the same unitary transformation in both sides or they are the same in the left hand side and the right hand side.

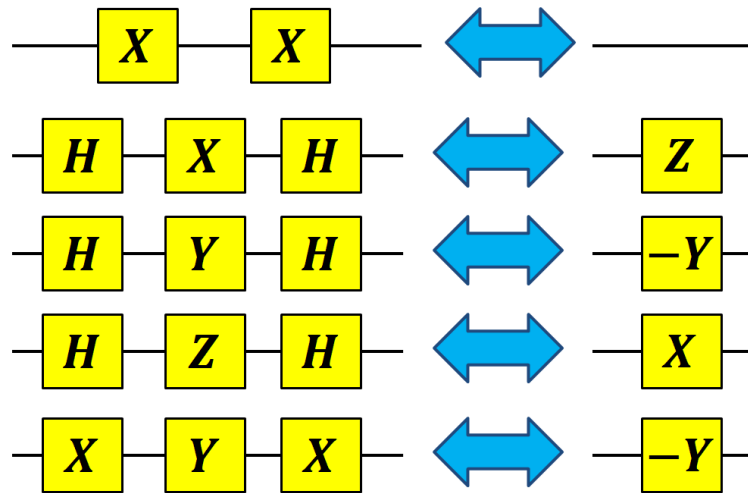


Fig. 2.13: Single qubit circuits which are simplified.

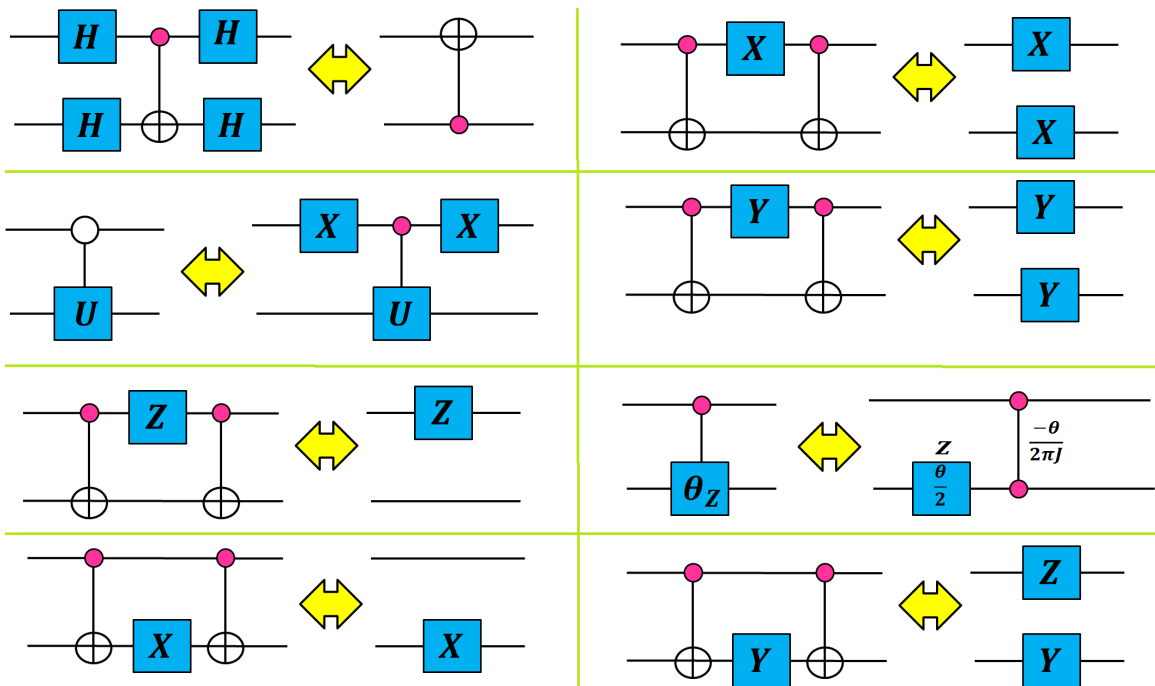


Fig. 2.14: two qubit circuits which are simplified.

SECTION: 2.5

Magnetic Field Gradients

Now, we would like to discuss the magnetic field gradients before we start to talk about the initial state of the nuclear spins and describe the preparation methods of the pseudo-pure state. Magnetic field gradients create spatial inhomogeneity of the magnetic field in the z direction along the sample tube, which has the effect of a non-unitary transformation on the macrostate of the system. The application of field gradients is necessary in the context of quantum computing for the preparation of pseudo-pure states and the reproduction of non-unitary evolution of a system.

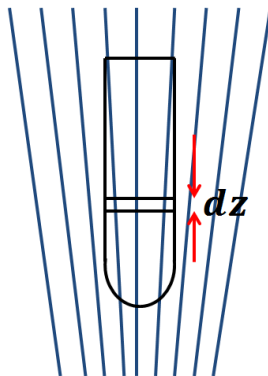


Fig. 2.15: Scheme of an NMR sample and field lines in a region with gradient.

In a region where the field generated by the gradient is $B(z)$ (Fig. (2.15)), the evolution is given by:

$$H = H_0 + \hbar B(z) \sum_i \gamma_i I_z^i, \quad (2.78)$$

where the subscript i refers to each of the spin systems. By assuming that the Hamiltonian of the system commutes with I_z . Thus, we consider only the effect of the interaction with the magnetic field gradient, since the evolution under the system Hamiltonian (with static field) adds only a multiplicative factor to the density matrix.

As the gradient term does not depend on time, the density matrix evolves according

to:

$$\rho(t) = e^{-iB(z)t \sum_i \gamma_i I_z^i} \rho(0) e^{iB(z)t \sum_i \gamma_i I_z^i}. \quad (2.79)$$

Using the basis of eigenstates of I_z , $|m_1, m_2, \dots, m_N\rangle$ which for simplicity we denote by $|M\rangle$, it is easy to see that an element of the density matrix evolves with:

$$\langle M' | \rho(t) | M \rangle = \langle M' | \rho(0) | M \rangle e^{iB(z)t \sum_i \gamma_i \delta_{M,M'}^i}, \quad (2.80)$$

where $\delta_{M,M'} = M - M'$. Since the observed signal is the average of the whole sample signal, we can integrate in the z direction to get the average. Assuming that the field generated by applying a gradient has the form $B(z) = \alpha z$, we have:

$$\frac{1}{2L} \int_{-L}^{+L} e^{iB(z)t \sum_i \gamma_i \delta_{M,M'}^i} dz = \frac{\sin(\alpha L t \sum_i \gamma_i \delta_{M,M'}^i)}{\alpha L t \sum_i \gamma_i \delta_{M,M'}^i}. \quad (2.81)$$

Then we see that, at the end of the application of the gradient for a sufficiently long time, the elements of the density matrix which satisfy $\delta_{M,M'} \neq 0$ are eliminated. It is worth noticing that the application of the magnetic field gradient itself is not a non-unitary operation, because the gradient is only a magnetic field that varies along the sample. What makes its non-unitary effect is the average over the sample, which happens in the acquisition of data.

SECTION: 2.6

Initialization

In order to implement quantum algorithms and extract relevant information, one must know the initial state of the quantum processor and that state should preferably be pure. Liquid state NMR does not offer this possibility due to its high temperature and ensemble nature, but techniques have been developed to partially overcome this limitation. This section is a review of existing techniques.

SUBSECTION: 2.6.1

The Initial State of Nuclear Spins and Effective Pure States

In Liquid state NMR experiments at room temperature, the state of the system is described by the Boltzmann thermal distribution. Therefore, the density matrix at the thermal equilibrium state is given by:

$$\rho_{th} = \frac{e^{-\beta H}}{Z}, \quad (2.82)$$

where $\beta = 1/(k_B T)$ and Z is the partition function ($Z = Tr(exp(-\beta H))$) and H is the Hamiltonian of N spins system. As we have in general $\omega_0^i \gg J_{ij}$ (ω_0 is on the order of MHz while J is on the order of tens to hundreds of Hz), in this equation only the term connected to the interaction with the external field is taken into account and we have not included the J -coupling between the spins. The Zeeman energy of the nuclei is much smaller than $k_B T$, so that $(\hbar\omega_0^i)/(k_B T) \approx 10^{-5} \ll 1$ for a temperature of 300K with a field of 11.74 Tesla. For N spins system in thermal equilibrium, we have:

$$\rho_{th} \approx \frac{1}{2^N} I + \frac{1}{2^N} \frac{\hbar}{k_B T} \sum_{i=1}^N \omega_0^i I_z^i, \quad (2.83)$$

where I is the $2^N \times 2^N$ identity matrix.

The non-identity part of the thermal state is called the deviation density matrix. So that the thermal state in liquid state NMR at room temperature is highly mixed. A single spin system in thermal equilibrium is then simply approximated by:

$$\rho_{th} = \frac{1}{2} I + \frac{\hbar\omega_0}{2k_B T} I_z. \quad (2.84)$$

The fact that the thermal equilibrium state at room temperature is highly mixed makes it difficult to prepare the spin system in the pure state ($|00\dots 0\rangle$) and we can not use standard NMR techniques to change the thermal equilibrium state into that state.

Because of this difficulty in preparing pure states in NMR systems, almost all experiments of quantum information processing by NMR use the pseudo-pure states, sometimes called effective pure states. There are several ways to prepare pseudo-pure states, especially methods of temporal [62] and spatial [63] averages and logical labeling[64]. These three methods are described in detail in the following subsections. In this thesis, we usually use the technique of spatial averaging which consists of applying spatially varying magnetic fields, or magnetic field gradients, to achieve the pseudo-pure state.

A pseudo-pure state of N qubits system is given by:

$$\rho_{eff} = \frac{1 - \epsilon_0}{2^N} I + \epsilon_0 |\psi\rangle\langle\psi|, \quad (2.85)$$

where ϵ_0 is a measure of the purity of a state, I is the $2^N \times 2^N$ identity matrix and $|\psi\rangle$ is a pure state such as $|00\dots 0\rangle$. It is valuable to mention that NMR experiments are only sensitive to the traceless deviation density matrix. Therefore, the observable signal in NMR is proportional to the difference between two populations, instead of the populations themselves and the density matrix proportional to the identity matrix does not produce a measurable signal. Hence any part of a density matrix that is proportional to the identity matrix can be ignored during the experiment. Furthermore, the identity matrix does not evolve under unitary operations, i.e. $U^\dagger I U = I$. We can only consider the deviation density matrix ρ_{dev} .

Gershenfeld and Chuang [64] and, independently, Cory, Havel and Fahmy [13, 62] realized that a density matrix of the form of Eq. (2.85) gives the signal and has the dynamic behaviour of just the second term, $|\psi\rangle\langle\psi|$, which represents a pure state. So, the goal is to create an effective pure state for which all populations are equal (identity part) except for one which differs (deviation part), for example $|00\dots 0\rangle$.

A convenient way of describing the pseudo-pure states is for using the product operator formalism which uses the Pauli matrices (see chapter (4)). For example, the pseudo-pure

state $|00\rangle\langle 00|$ is described on this basis as $I_z^1 + I_z^2 + 2I_z^1 I_z^2$, wherein the identity term was neglected because it was not observed in the NMR signal as we have mentioned. The use of this basis simplifies the visualization of the effects of unitary and non-unitary transformations on qubits, facilitating the construction of sequences of pulses for the preparation of states and implementation of logical operations.

— SUBSECTION: 2.6.2 —

Spatial Labeling

Spatial averaging [62] averages the NMR signal spatially over a volume of the sample to equalize all populations expect for the ground state population. This is done via magnetic field gradients to remove undesirable coherences. All non-diagonal entries of the density matrix are made zero in this method. Spatial averaging can be easily understood by using the product operator formalism.

From the thermal equilibrium state of a system of two homonuclear spins, $I_z^1 + I_z^2$, the sequence of transformations:

$$I_z^1 + I_z^2$$

$$R_x^2(60) \Rightarrow I_z^1 + \frac{1}{2} I_z^2 - \frac{\sqrt{3}}{2} I_y^2 \quad (2.86)$$

$$G_z \Rightarrow I_z^1 + \frac{1}{2} I_z^2 \quad (2.87)$$

$$R_x^1(45) \Rightarrow \frac{\sqrt{2}}{2} I_z^1 + \frac{1}{2} I_z^2 - \frac{\sqrt{2}}{2} I_y^1 \quad (2.88)$$

$$t(1/2J_{12}) \Rightarrow \frac{\sqrt{2}}{2} I_z^1 + \frac{1}{2} I_z^2 + \frac{\sqrt{2}}{2} I_x^1 I_z^2 \quad (2.89)$$

$$R_y^1(-45) \Rightarrow \frac{1}{2} I_z^1 - \frac{1}{2} I_x^1 + \frac{1}{2} I_z^2 + \frac{1}{2} I_x^1 I_z^2 + \frac{1}{2} I_z^1 I_z^2 \quad (2.90)$$

$$G_z \Rightarrow \frac{1}{2} I_z^1 + \frac{1}{2} I_z^2 + \frac{1}{2} I_z^1 I_z^2 \quad (2.91)$$

where G_z indicates the application of gradient in the direction z , $t(1/2J_{12})$ indicates a

period of free evolution of the system in duration $1/2J$ and I_i^1 (I_i^2) denotes a rotation about the spin 1 (2) in the direction i . Here and throughout the section, the system state is described using the deviation density matrix. This technique has been successfully used for state preparation on two or three spins. That is the one that we have used for preparing a pseudo-pure state in this thesis.

SUBSECTION: 2.6.3

Logical Labeling

Logical labeling [64, 65] consists of applying a pulse sequence which rearranges the thermal equilibrium populations such that a subset of the spins is in an effective pure state, conditioned upon the state of the remaining spins. Then the computation is carried out within this embedded subsystem.

We explain logical labeling using a three-spin example. The thermal equilibrium deviation density matrix for a homonuclear three-spin system is approximately:

$$\rho_{eq} = \frac{1}{2^3} \frac{\hbar\omega_0}{2k_B T} \begin{bmatrix} 3 & & & & & & & \\ & 1 & & & & & & \\ & & 1 & & & & & \\ & & & -1 & & & & \\ & & & & 1 & & & \\ & & & & & -1 & & \\ & & & & & & -1 & \\ & & & & & & & -3 \end{bmatrix}, \quad (2.92)$$

where this diagonal represents the populations of the state $|000\rangle, |001\rangle, \dots, |111\rangle$. Suppose we can swap the populations of the states $|011\rangle$ and $|100\rangle$, which can be done using a

sequence of one and two-qubit operations. The density matrix changes into:

$$\rho_{eff} = \frac{1}{2^3} \frac{\hbar\omega_0}{2k_B T} \begin{bmatrix} 3 & & & & & & & \\ & 1 & & & & & & \\ & & 1 & & & & & \\ & & & 1 & & & & \\ & & & & -1 & & & \\ & & & & & -1 & & \\ & & & & & & -1 & \\ & & & & & & & -3 \end{bmatrix}. \quad (2.93)$$

Now, the subspace $|000\rangle, |001\rangle, |010\rangle, |011\rangle$ is in an effective pure state. In other words, when spin 1 is $|0\rangle$, the system is effective pure. Performing logical operations within this subsystem allows two-qubit quantum computations (this may require decoupling spin 1 from the other spins).

SUBSECTION: 2.6.4

Temporal labeling

Temporal labeling consists of averaging multiple experiments, each of which underwent a different permutation of the populations. Each experiment is designed such that the sum of the input states equals an effective-pure state. Since quantum mechanics is linear, the sum of the resulting output states behaves as if the computation was done on a pure state.

Assume that we are given only homonuclear spins so that each term in the thermal density matrix has the same weight. The idea then is to perform a series of *CNOT* operations that transform the n terms in the thermal density matrix into a different set of n terms that are part of the effective-pure state. We then perform a different series of operations to create additional n new terms. Since $2^n - 1$ terms are required, and we can create n terms in each experiment, we need to perform $\lceil (2^n - 1)/n \rceil$ to obtain all necessary

terms. We can cancel out additional terms by performing *NOT* operations.

The following relations illustrate how *CNOT* and *NOT* operations affect the product operator terms:

$$I I \xrightarrow{CNOT_{12}} I I \quad (2.94)$$

$$I I_z^1 \xrightarrow{CNOT_{12}} I_z^1 I_z^2 \quad (2.95)$$

$$I_z^1 I \xrightarrow{CNOT_{12}} I_z^1 I \quad (2.96)$$

$$I_z^1 I_z^2 \xrightarrow{CNOT_{12}} I I_z^2 \quad (2.97)$$

$$I \xrightarrow{NOT} I \quad (2.98)$$

$$I_z^1 \xrightarrow{NOT} -I_z^1 \quad (2.99)$$

As an example, let us explain a three-qubit homonuclear example. The thermal density matrix is given by $\rho_{th} \cong I_z^1 + I_z^2 + I_z^3$. The following three experiments create an effective pure state $\rho_{eff} \cong I_z^1 + I_z^2 + I_z^3 + I_z^1 I_z^2 + I_z^1 I_z^3 + I_z^2 I_z^3 + I_z^1 I_z^2 I_z^3$ after summing over all terms:

$$CNOT_{21} CNOT_{32} \mapsto I_z^1 I_z^2 I_z^3 + I_z^2 I_z^3 + I_z^3 \quad (2.100)$$

$$CNOT_{31} \mapsto I_z^1 I_z^3 + I_z^2 + I_z^1 \quad (2.101)$$

$$CNOT_{12} NOT_3 \mapsto I_z^1 + I_z^1 I_z^2 - I_z^3 \quad (2.102)$$

For heteronuclear spins each term in the thermal density matrix has a different weight and hence we require $2^n - 1$ experiments to obtain all terms in the effective-pure state. If k of the n spins are homonuclear, we simply create k new terms in each experiment, requiring $[(2^n - 1)/k]$ experiments.

Now, we describe a method of preparing pseudo pure state based on Controlled-transfer gates using spatial averaging techniques [22]. We have used this method for preparing pseudo pure state of three homonuclear system (see chapter (6)). In this procedure

of preparing pseudo pure state, the population of the ground state remains unchanged throughout the process which ensures the maximum purity of the prepared state.

SECTION: 2.7

Preparing Pseudo-Pure States With Controlled-Transfer Gates

All methods for preparing pseudo-pure states work by averaging the populations of states other than the ground state, ideally leaving the ground state unchanged. This method consists of using a Controlled-rotation gate with a rotation angle of θ , followed by the application of a magnetic field gradient which both of them are called Controlled-transfer gate [66]. The quantum circuit of the Controlled-transfer gate is shown in Fig. (2.16).

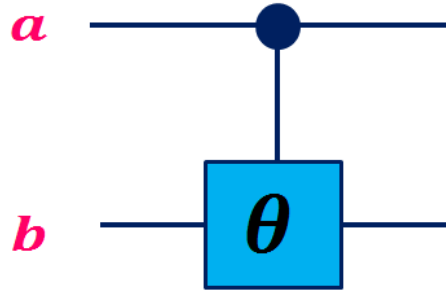


Fig. 2.16: Quantum circuit representation of a Controlled-transfer gate with qubit a as control and qubit b as target. Magnetic field gradient is after Controlled-rotation gate and which is implicit.

The performance of a Controlled-transfer gate on a general population state or on diagonal state of a two-qubit system is given by:

$$\begin{bmatrix} a & 0 & 0 & 0 \\ 0 & b & 0 & 0 \\ 0 & 0 & c & 0 \\ 0 & 0 & 0 & d \end{bmatrix} \rightarrow \begin{bmatrix} a & 0 & 0 & 0 \\ 0 & b & 0 & 0 \\ 0 & 0 & c' & 0 \\ 0 & 0 & 0 & d' \end{bmatrix}, \quad (2.103)$$

where c' and d' are given by:

$$c' = \frac{c + d + (c - d) \cos \theta}{2}, \quad (2.104)$$

$$d' = \frac{c + d - (c - d) \cos \theta}{2}, \quad (2.105)$$

where θ is the Controlled-rotation angle.

For preparing a pseudo-pure state of a two-qubit system, the Controlled-transfer gate must be applied two times, one with the qubit one as control and second with the qubit two as control. The rotation angles for each of these gates are calculated from the coefficients of the thermal state of the system. This preparation scheme for a two-qubit system is illustrated by the circuit below:

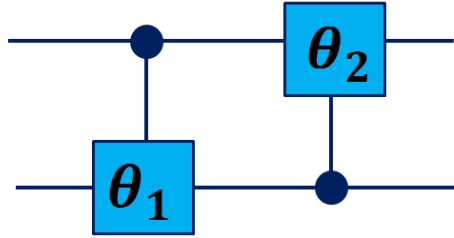


Fig. 2.17: Quantum circuit for the preparation of pseudo-pure state of a two-qubit system. The gates are applied from left to right.

For generating a pseudo-pure state, the angles θ_1 and θ_2 must be set to:

$$\theta_1 = \arccos\left[\frac{2b - (c + d)}{3(c - d)}\right], \quad \theta_2 = \frac{\pi}{2}. \quad (2.106)$$

The Controlled-transfer gates (see Fig. (2.16)) with qubit one as control and qubit two as target can be implemented by the sequence of pulses as:

$$\begin{aligned} R_y^2\left(\frac{\pi}{2}\right) &\rightarrow R_x^2(\pi) \rightarrow U_J\left(\frac{\theta}{2\pi J}\right) \rightarrow R_x^2(\pi) \\ &\rightarrow R_z^1\left(\frac{\theta}{2}\right) \rightarrow R_z^2\left(\frac{\theta}{2}\right) \rightarrow R_y^2\left(\frac{\pi}{2}\right) \rightarrow G_z, \end{aligned} \quad (2.107)$$

where G_z presents the magnetic field gradient in the \hat{z} direction, the superscripts indicate which spin is excited and the subscripts denote the phase of the pulses. U_J is a free evolution of the system Hamiltonian.

At the end of Fig. (2.17), the pseudo-pure state is given by:

$$\begin{bmatrix} a & 0 & 0 & 0 \\ 0 & \frac{b+c+d}{3} & 0 & 0 \\ 0 & 0 & \frac{b+c+d}{3} & 0 \\ 0 & 0 & 0 & \frac{b+c+d}{3} \end{bmatrix}. \quad (2.108)$$

As we can see for the matrix in Eq. (2.108), the populations of the excited levels are changed in the process of preparing the pseudo-pure state. In other words, the populations b , c , and d are mixed and the population of the ground state is unchanged. This ensures the maximum possible purity of the pseudo-pure state.

For the preparation of pseudo-pure state in systems with more qubits, the Controlled-transfer gates must be applied only on the spins in which the coupling is stronger in order to optimize the time spent in preparing states. Therefore, for a three-qubit system, the following circuit is used in the preparation of the pseudo-pure state:

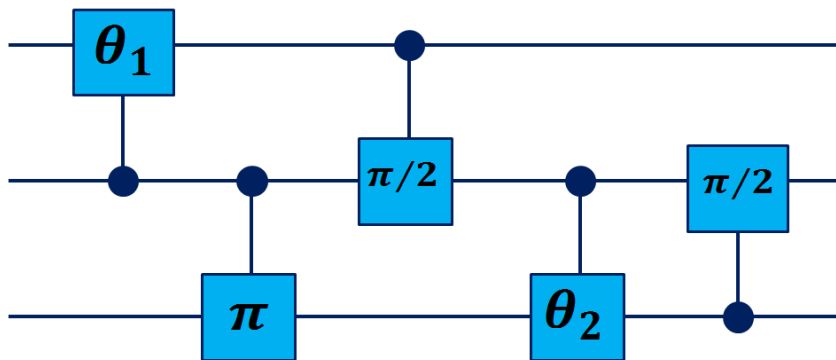


Fig. 2.18: Quantum circuit for preparation of pseudo-pure state of a three-qubit system. The gates are applied from left to right. Where the angles $\theta_1 = \arccos(-1/7) \approx 98.2^\circ$ and $\theta_2 = \arccos(-5/7) \approx 135.6^\circ$.

SECTION: 2.8

Measurement

This section discusses the measurement procedure of nuclear spins in liquid solution. We begin by determining the physical properties of the measured signal: It is an induced oscillating voltage for which the Fourier transform yields the NMR spectrum.

SUBSECTION: 2.8.1

Interpretation of NMR Spectra**The NMR Signal**

The signal of a single nuclear spin is too weak to be directly detected, and therefore NMR experiments are performed using a large ensemble of identical molecules, typically on the order of 10^{23} , all dissolved in a liquid solvent. The entire sample is subject to the same radio frequency field and hence each molecule undergoes the same operations.

The same RF coil that produces the B_1 field is also used to detect the signal. The spins precess about the \hat{z} -axis at their respective Larmor frequency. Then, the spins in a sample are rotated from their equilibrium direction to the transverse plane with an applied RF pulse and the precessing magnetization in the RF coil around the sample induces the voltage. The NMR signal is displayed as a function of time. We can perform a Fourier transform from this signal to obtain the spectrum. Fourier transform is a mathematical technique that converts a function of the time into a function of frequencies, according to:

$$S(\omega) = \int_0^{\infty} S(t)e^{-i\omega t} dt. \quad (2.109)$$

The amplitude and phase of the spectral lines give us information about the respective spin states. Mathematically, we can write the induced voltage in the RF coil due to spin

i as:

$$V_i(t) = V_0 \text{Tr}[e^{-iH_0t/\hbar}\rho(0)e^{iH_0t/\hbar}(-i\sigma_x^i - \sigma_y^i)], \quad (2.110)$$

where V_0 is the maximum signal strength and $\rho(0)$ is the density matrix at the start of the measurement. The phases of the observable $(-i\sigma_x^i - \sigma_y^i)$ are chosen such that a positive absorptive line corresponds to a spin along $-\hat{y}$ (this is the signal we obtain if we apply a $R_x(90)$ rotation on a spin in the state $|0\rangle$). Similarly, we choose a negative absorptive line to correspond to the spin being along $+\hat{y}$, and a positive and negative dispersive lines to a spin along $+\hat{x}$ and $-\hat{x}$ respectively. Eq. (2.110) represents the signal in the lab frame, but by mixing the signal with a reference oscillator at ω_0^i , we obtain instead the expectation value of $(-i\sigma_x^i - \sigma_y^i)$ in the rotating frame, which is the relevant reference frame for quantum computing. If ρ is mixed, as is the case in room temperature experiments, the expectation value represents an averaged read out over the statistical mixture of states.

Since a spin along the $\pm\hat{z}$ -axis of the Bloch sphere, corresponding to the computational basis states $|0\rangle$, $|1\rangle$, can not induce a voltage in the RF coil, we have to change the basis to obtain a measurement in the $|0\rangle$, $|1\rangle$ basis. This is achieved using a $R_x(90)$ read-out pulse. With the above phase conventions, a spin in the $|0\rangle$ state produces a positive absorptive signal following the read-out pulse, and a spin in the $|1\rangle$ state produces a negative absorptive signal.

Measurement Process

The RF coil is present at all times, contributing only small amounts to decoherence. The other decoherence process (inhomogeneities in B_0 , interactions with other spins and the environment) are still active. The transverse component of the magnetic moment hence decays over time, usually exponentially. This decaying signal in the time domain is called free induction decay, or FID for short. The FID typically decays as $V(t)e^{-t/T_2^*}$ where T_2^* includes the T_2 decoherence processes as well as other systematic phase randomizations. Using Eq. (2.109), the Fourier transform of this signal gives rise to a Lorentzian lineshape:

$$V(t) e^{-t/T_2^*} \Rightarrow \frac{\lambda}{\lambda^2 + (\omega - \omega_0)^2} - \frac{i(\omega - \omega_0)}{\lambda^2 + (\omega - \omega_0)^2}, \quad (2.111)$$

where $\lambda = \frac{1}{T_2^*}$ and the two terms correspond to the absorptive and dispersive components which may or may not be both present at the same time. The linewidth at half height is given by:

$$\Delta f = \frac{\Delta\omega}{2\pi} = \frac{1}{\pi T_2^*}. \quad (2.112)$$

The Figure (2.19) (a) and (b) show free induction decay (FID) and the Fourier transform of the FID signal from carbon-13 labeled trichloroethylene (see Fig. (5.1)) in the thermal equilibrium state, respectively.

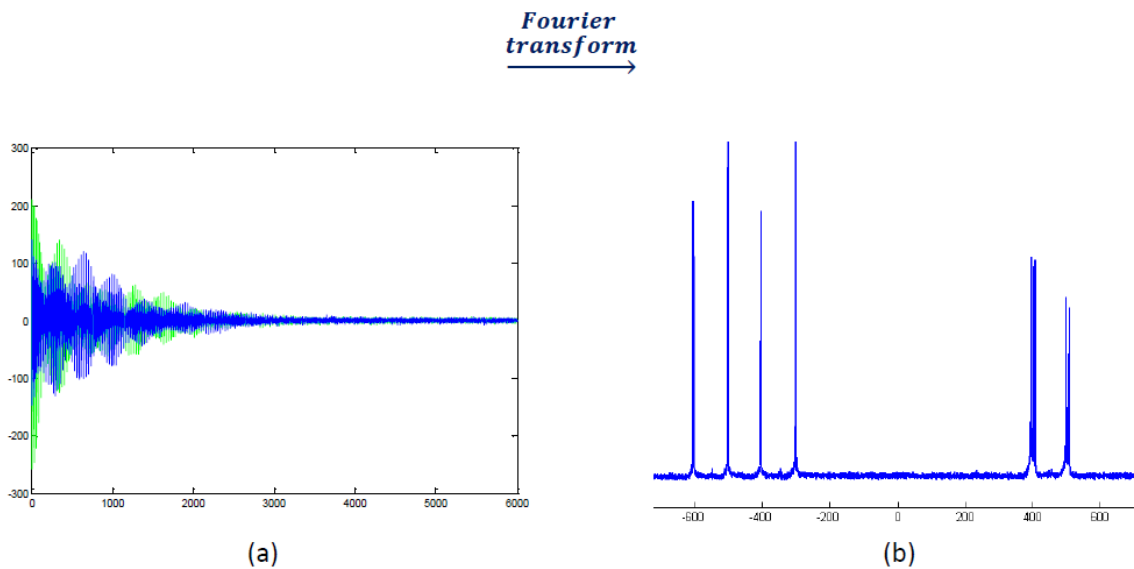


Fig. 2.19: (a) Free induction decay (FID) and (b) the Fourier transform of the FID signal (Carbon spectrum) from carbon-13 labelled trichloroethylene in the thermal equilibrium state.

As mentioned earlier, when we apply a read-out pulse on a single spin that is either in the $|0\rangle$ or $|1\rangle$ state, we obtain either a positive or negative absorptive line. This is the case for most quantum computations. However, other states such as superpositions give rise to different signals. By designing a proper sequence of different read-out pulses, we can reconstruct the full density operator of this single spin.

In Chapter (4) and (5), we completely describe how the full density operator can be reconstructed by performing several experiments each with appropriate unitary transformations just before the measurement. In the following section, we give a brief description of the experimental apparatus.

SECTION: 2.9

The NMR Spectrometer

NMR spectrometers have now become very complex instruments capable of performing an almost limitless number of sophisticated experiments. However, the essential parts of a spectrometer are not that complex to understand in outline, and it is certainly helpful when using the spectrometer to have some understanding of how it works. The main components of a NMR spectrometer are outlined in Fig. (2.20). A sample containing a large number of identical molecules dissolved in some liquid solution is placed in a strong, static and nearly homogeneous magnetic field. The radio frequency (RF) pulses are generated by a radio-frequency coil placed next to the sample inside a probe. The same coil is used to detect the signal of the spins during the measurement. The experiment is controlled by a computer. We next explain the main components: the sample, the magnet, the RF transmitter, duplexer, the probe and the signal receiver. In this thesis, all experiments were performed with high-resolution spectrometer, Varian Premium Shielded 500MHz.

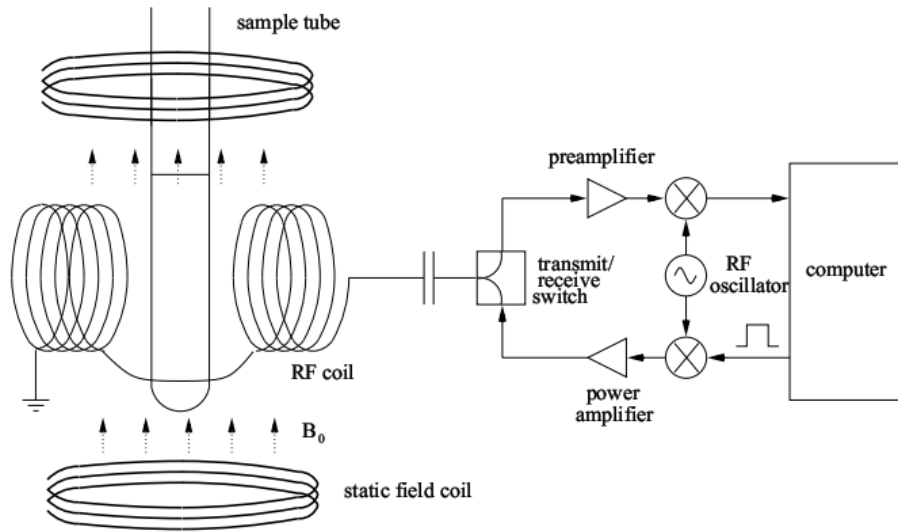


Fig. 2.20: Scheme of a NMR spectrometer.

- **Sample**

The physical NMR qubits are represented by the spin-1/2 nuclei of atoms in a molecule. Since the signal of a single molecule is too weak to be detected with current technologies, we use a liquid solution containing $\sim 10^{23}$ molecules to enhance the signal. These molecules are dissolved in some liquid solvent at room temperature and atmospheric pressure. The solvent is chosen based on the solubility of the molecules in the solvent, and on the coherence times of the qubits obtained in this solvent. The NMR solvents are usually deuterated because the deuterium signal is used as part of a feedback loop which keeps the detection system locked over the course of several experiments.

The sample solution is held in a thin-walled glass NMR sample tube with a 5mm outer diameter (4.2mm inner diameter). The sample tube is filled with our liquid solution to about 5cm from the bottom. It is critical that the walls of the tube be straight and uniform in thickness, in order to minimize fluctuations of the magnetic susceptibility.

Finally, the open end of the glass sample tube is flame sealed to prevent impurities from leaking into the solution. The filled and sealed sample tube is then placed in a sample holder called “spinner” (see Fig. (2.21)). As the name suggests, the sample holder does not only hold the sample in place but it is also used to spin the sample about the axis of the static magnetic field to average out $\hat{x}\hat{y}$ inhomogeneities in the static field.

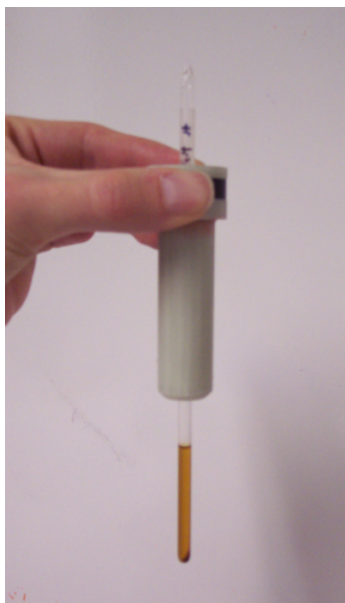


Fig. 2.21: A typical NMR sample. The sample tube is held by a sample holder when it is inserted in the superconducting magnet.

- **Magnet**

The sample inside the sample holder is placed in the bore of a superconducting magnet at room temperature. The magnet is made of a superconducting solenoid immersed in a bath of liquid Helium (4.2 Kelvin). A current passing through the solenoid produces the static magnetic field. The Helium vessel is surrounded by a vacuum seal, a liquid Nitrogen vessel and another vacuum seal. The whole magnet is mounted on air-cushioned vibration isolation legs (see Fig. (2.22)).



Fig. 2.22: Varian 500 MHz NMR magnet. The fill ports for liquid Nitrogen and Helium are at the top of the magnet. The probe is inserted at the bottom of the magnet, while the sample is inserted from the top.

The current that passes through the superconducting solenoid is on the order of 100A in strength, producing a field of about 11.74 Tesla at the center of the magnet (about 200,000 times as strong as the earth's magnetic field). The resulting Larmor frequency of 1H spin is 500 MHz. The field strength outside the magnet drops off dramatically, reaching only 5 Gauss about 3 meters away from the magnet (about 10 times the earth's magnetic field). Due to the strong fields, we must make sure that no magnetic objects are placed close to the magnet. Magnetic objects can be pulled into the bore and damage the magnet.

Sensitivity and resolution of NMR signals are the fundamental reasons for the requirement of higher magnetic field strengths. Resolution of NMR spectra at a constant line width in hertz improves linearly with magnetic field strength (B_0).

The sensitivity of an NMR signal is proportional to the population difference between two nuclear transition states. Because the energy gap of the two nuclear states is small (in the RF range), the population difference determined by the Boltzmann distribution is also small. An increase in field strength will increase the population difference, and thus increases sensitivity.

The magnet has to be regularly refilled with liquid Nitrogen (once a week) and liquid Helium (once every 3 months).

- **Transmitter**

The function of the transmitter is to generate, amplify, and send RF pulses to the probe. The transmitter section is made up of other smaller parts, such as: 1) synthesizer, which is responsible for generating radio frequency signals continuously; 2) Pulse programmer; 3) radio frequency amplifier, which increases the intensity of the applied signal in the sample; 4) the attenuator, which allows us to control the intensity of signal sent to the sample. A basic electronic block diagram of the transmitter section of a NMR spectrometer is shown in Fig. (2.23) [6].

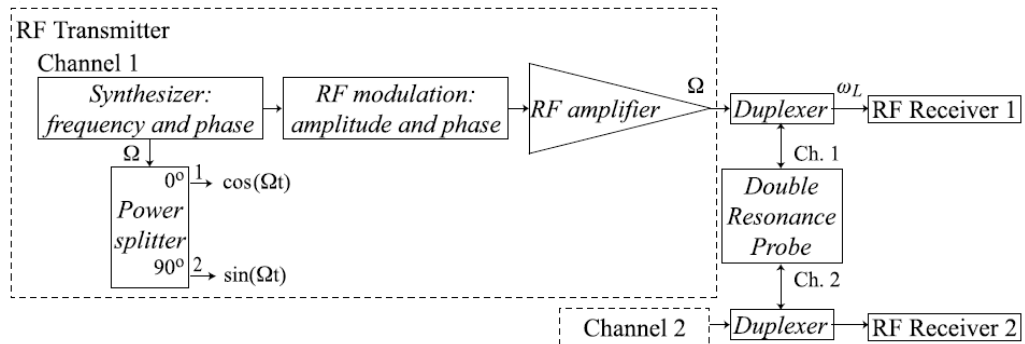


Fig. 2.23: Block diagram of a NMR spectrometer (transmitter section).

- **Duplexer**

From the duplexer, two cables emerge. One cable leads to the probe, which is mounted inside the magnet, and which contains the sample. The second cable leads to the receiver section, which is used to detect the weak radio frequency signals generated by the nuclear spins. When a strong radio frequency pulse arrives from the amplifier, the duplexer diverts it towards the probe, not into the sensitive signal detection circuitry and when, on the other hand, the tiny NMR signal travels from the probe to the duplexer, it is diverted into the signal detection path, not towards the amplifier.

- **Probe**

A wave generator produces a voltage that oscillates sinusoidally at a desired frequency. This output is cut off in pulses by a switch which is opened and closed by a pulse generator, controlled by the computer spectrometer. The pulses are amplified and sent to the NMR probe.

The probe is in a cylindrical aluminum housing which contains the RF coils, a tuning and matching electrical circuit, a temperature control system, a sample spinning mechanism and sometimes gradient coils. The probe also contains the sample and it is responsible for coupling the RF field to the spins. In the probe, the NMR signal from the sample is collected.

The probe may contain a (Z) gradient coil, or three ($X; Y; Z$) gradient coils, or none. These coils produce a static magnetic field in the \hat{z} direction, but the strength of this field varies linearly along the \hat{x} ; \hat{y} or \hat{z} axis.

- **Receiver**

The precession of the nuclear magnetization, excited by this RF field, in the same

coil induces an oscillating voltage, which is the NMR signal, that is sent in sequence to the receiver. So, the function of the receiver is to record the voltage induced in the coil by the oscillating magnetic signals from the spins. In other words, a receiver is used to detect the NMR signal generated at the probe and amplify the signal to a level suitable for digitization. At the receiver, after being pre-amplifier, the NMR signal is mixed with a reference frequency, usually the same as that was used by the pulse for exciting the spins. Because the RF signal is very weak coming from the probe, it is amplified first by a preamplifier that is located near or inside the probe to reduce the loss of signal, before it is transferred to the receiver inside the console. A basic electronic block diagram of the receiver section of a NMR spectrometer is shown in Fig. (2.24) [6].

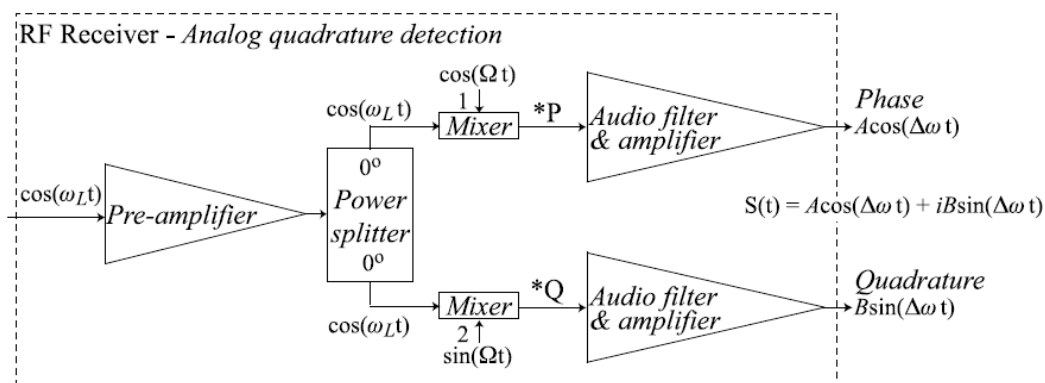


Fig. 2.24: Block diagram of a NMR spectrometer (receiver section).

- **The Analogue to Digital Converter**

The signals generated at the probe coil and detected by the receiver are in continuous or analog form, meaning that their amplitudes change smoothly, such as in a sine wave. However, the signals to be processed by computers and other electronic devices in the NMR spectrometer are a digital or discrete type, which means that their amplitudes can only exist in certain levels or ranges, such as binary digits.

On the other hand, the output controlled by the computer needs to be converted to analog form. Therefore, for NMR spectrometers it is necessary to accurately convert an analog signal to a digital number proportional to its amplitude (ADC), and vice versa (DAC). Then, an analogue to digital converter or ADC is used to convert the NMR signal from a voltage to a binary number which can be stored in the computer memory. These conversions are essential in a wide variety of processes in which the analog information is converted (ADC) for data processing and display such as the Fourier transformation of the time domain data, and the digital information is converted to analog (DAC) for a computer controlling the experimental setup such as shimming, gradient pulse amplitude, or waveform generation.

The Pulse Programmer

The spectrometer is operated using software from Varian (Vnmr). All experiments can be controlled entirely by the software, provided that the hardware has been properly configured for a particular experiment.

The pulse sequences are written in C, and several commands are provided by Varian's software. These commands typically involve specific parameters, such as the pulse width, phase, pulse shape, and channel number.

Each pulse sequence and framework must be compiled, and is then submitted to the spectrometer. The digitized signal can be Fourier transformed and displayed by the Varian software as well. Further processing, such as zeroth and first-order phase corrections or line-broadening, can also be applied.

Most of our analysis is not done by the Varian software. Instead, we interface with the spectrometer via MATLAB which allows us to set up a large number of experiments to run automated. The data is also stored in some desired directory

for future analysis. We can then use other MATLAB routines to analyze the data as it is accumulated. For example, in quantum state tomography experiments, the density matrix is derived from a large set of output spectra. The flexibility in MATLAB programs thus allows easy execution of a pulse sequence and a straightforward analysis of the collected data.

3

Gradient Ascent Pulse Engineering

In quantum computing, logic gates are implemented as unitary operators acting on qubits. In NMR implementations these unitary operators are realized by sequences of radio-frequency pulses and the natural evolution of the spin system. In general, a pulse sequence that generates a desired unitary propagator is neither trivial nor unique. It is useful to find optimal sequences that minimize the negative effects of errors, relaxation, and decoherence. However, it is much more difficult to find an appropriate control sequence to perform some desired operation. Numerical methods offer effective solutions to this problem. One of the solutions is Gradient Ascent Pulse Engineering (GRAPE) algorithm. GRAPE algorithm was introduced by Khaneja et al. [11] for the design of pulse sequences in NMR spectroscopy. The algorithm utilizes optimal control theory to search for pulses that can maximize the coherence transfer between coupled spins as well as minimize relaxation effects during a given time step. This method allows us to optimize functions with more variables, which makes the optimization result be smoother.

SECTION: 3.1

The Optimal Control Framework

We begin with a general definition of the optimal control problem. Consider a system with state vector $x(t)$, influenced by controls $u(t)$ over the time interval $[0, T]$. The scalar, real-valued objective functional Φ (also called the quality function or fidelity) is written in the form:

$$\Phi = \Psi(x(T)) + \int_0^T L(x(t), u(t)) dt. \quad (3.1)$$

It is worth mentioning that the first term in the above equation depends only on the state at the final time T , while the second term integrates up a running cost. The task is to maximize Φ subject to the condition that the equation of motion of the system,

$$\frac{dx}{dt} = \mathbf{f}(\mathbf{x}(t), u(t)), \quad (3.2)$$

is satisfied, with $x(t) = x_0$ and $u(t)$ is restricted to the set of permissible controls. A solution is said to be time-optimal if Φ is maximized for the minimum value of T which is denoted by T_{min} .

For a more detailed introduction into optimal control, see [67], [68] and the book by Kirk [69].

SECTION: 3.2

Optimal Control For Quantum Systems

A closed quantum system can be described by the Hamiltonian,

$$H_{tot}(t) := H_0 + \sum_{m=1}^M u_m(t) H_m, \quad (3.3)$$

where H_0 is the drift Hamiltonian, H_m are the control Hamiltonians or radio-frequency Hamiltonians corresponding to the available control fields and $u_m(t) = (u_1(t), u_2(t), \dots, u_m(t))$

represents the vector of amplitudes that can be changed and which is referred to as the control vector. In the case of a spin 1/2, e.g., we have $H_m = \{I_x, I_y\}$. The state of the spin system is characterized by the density operator $\rho(t)$, and its equation of motion is the Liouville-von Neumann equation [70]:

$$\frac{d\rho(t)}{dt} = -i[H_{tot}(t), \rho(t)]. \quad (3.4)$$

We can write this equation of motion for the propagator of a closed quantum system as follows:

$$\frac{dU(t)}{dt} = \dot{U}(t) = -iH_{tot}(t)U(t). \quad (3.5)$$

At $t = 0$, the initial propagator is $U(0) = 1$.

The control problem for synthesising a target operator, or quantum gate, U_G can now be described as:

$$\max \phi(u), \text{ subject to } \dot{U}(t) = -iH_{tot}(t)U(t). \quad (3.6)$$

As we mentioned, the quality function Φ in Eq. (3.1) contains a term for the quality at the final time T and a term representing the running cost. The final quality reflects the distance between the achieved unitary operation $U(T)$ and the desired gate U_G .

There are two ways for expressing the geometrical distance between the two unitary operators U_G and $U(T)$. The first one takes the global phase between the two operators into account and yields the quality term as follows:

$$\Phi_1 := \text{Re } \text{tr}\{U_G^\dagger U(T)\}/N, \quad (3.7)$$

which is normalised to 1 and N is the matrix dimension. Φ_1 achieves the maximum of 1 if and only if $U(T) = U_G$, which follows from

$$\|U(T) - U_G\|_2^2 = 2N - 2\text{Re } \text{tr}\{U_G^\dagger U(T)\}, \quad (3.8)$$

and the property of the Hilbert-Schmidt norm $\|x\| = 0 \Leftrightarrow x = 0$.

For practical applications the global phase can be neglected. For this purpose we define a quality function that is insensitive to any global phase factors:

$$\Phi_2 := |\text{tr}\{U_G^\dagger U(T)\}|^2 / N^2. \quad (3.9)$$

This function is maximized if

$$U(T) = e^{-i\theta} U_G, \quad (3.10)$$

for any $\theta \in [0, 2\pi]$.

SECTION: 3.3

Algorithmic Scheme

Here, we present an iterative scheme for performing the maximization of Eq. (3.6) by updating the control vector u . The following steps describe this algorithm.

Step 1: Initial Setup

Fix a final time T and a digitization K such that T is divided into K time steps t_k with $\Delta t_k = t_k - t_{k-1} = T/K$. During each step k , the control term H_m and the corresponding control amplitude $u_m(t_k)$ are constant. Guess a random initial value $u_m(t_k)$ for all k and m .

Step 2: Compute Hamiltonians

The total Hamiltonian is constant over each time interval t_k . The total Hamiltonian can be computed as follows:

$$H_{tot}(t_k) = H_0 + \sum_m u_m(t_k) H_m \quad \forall t_k. \quad (3.11)$$

Step 3: Exponentiate

The unitary propagator $U(T)$ can be obtained via direct integration of $\dot{U} = -iH_{tot}U$ with $U(0) = 1$. Then, the propagators U_k for the system can be computed by the exponentials:

$$U_k = e^{-i\Delta t_k H_{tot}(t_k)} \quad \forall k. \quad (3.12)$$

The total propagator is obtained by the product of U_k . The goal of optimization is to find the u_m such that this propagator corresponds to a given target unitary transformation.

Step 4: Propagate Forward

Set $U_0 = \mathbf{1}$ and calculate the forward propagation as follows:

$$U_{k:0} = U_k \cdot U_{k-1} \dots U_1 \cdot U_0 \quad \forall k. \quad (3.13)$$

Step 5: Propagate Backward

Similarly, set $U_{K+1} = U_G^\dagger$ and calculate the backward propagation as follows:

$$\lambda_{K+1:k+1} := U_{K+1} \cdot U_K \dots U_{k+2} \cdot U_{k+1} \quad \forall k. \quad (3.14)$$

Step 6: Evaluate Quality

Evaluate the quality function according to Eq. (3.7) or Eq. (3.9):

$$\Phi_1 = \text{Re } \text{tr}\{U_G^\dagger U(T)\}/N = \text{Re } \text{tr}\{\lambda_{K+1:k+1} U_{k:0}\}/N,$$

or

$$\Phi_2 = |\text{tr}\{U_G^\dagger U(T)\}|^2/N^2 = |\text{tr}\{\lambda_{K+1:k+1} U_{k:0}\}|^2/N^2.$$

Step 7: Get Gradient

The derivative of the quality function Φ_1 with respect to $u_m(t_k)$ is:

$$\begin{aligned}
\nabla_{k,m}\Phi_1 &= \text{Re}\nabla_{k,m}\text{tr}\{\lambda_{K+1:k+1}U_{k:0}\}/N \\
&= \text{Retr}\{\nabla_{k,m}(\lambda_{K+1:k+1}U_{k:0})\}/N \\
&= \text{Retr}\{\lambda_{K+1:k+1}(\nabla_{k,m}U_{k:0})\}/N \\
&= \text{Retr}\{\lambda_{K+1:k+1}(\nabla_{k,m}U_k)U_{k-1:0}\}/N \\
&= \text{Retr}\{\lambda_{K+1:k+1}(\nabla_{k,m}e^{-i\Delta t_k H_{\text{tot}}(t_k)})U_{k-1:0}\}/N.
\end{aligned} \tag{3.15}$$

Since the control Hamiltonians do not commute with the total Hamiltonian in the general case, calculating the derivative of the exponential is nontrivial. There are several methods to obtain this derivative including: 1) an approximation of the gradient term to first order in Δt_k (the standard approximation), 2) the well-known finite-difference method, 3) an approximation using a series expansion, and 4) an exact method based on the eigen-decomposition of the total Hamiltonian and etc. In this thesis, for computing the gradient vector, we have used the methods number one and two. For more details about numbers three and four see [71] and [72], respectively.

The gradient vector for all t_k and u_m ,

$$\nabla\Phi = \left(\frac{\partial\Phi(U_{1:0})}{\partial u_1(t_1)}, \dots, \frac{\partial\Phi(U_{k:0})}{\partial u_m(t_k)}, \dots, \frac{\partial\Phi(U_{K:0})}{\partial u_M(t_K)} \right),$$

can be computed by using one of the formulas derived in parts A and B below. We introduce the shorthand notation $\nabla_{k,m}\Phi = \frac{\partial\Phi}{\partial u_m(t_k)}$ for gradient vector.

A: The Standard Gradient Approximation

The general approach for computing the derivative of the exponential of a matrix function $f(x)$ is [73]:

$$\frac{\partial}{\partial x}e^{f(x)} = \int_0^1 e^{sf(x)} \frac{\partial f}{\partial x} e^{(1-s)f(x)} ds. \tag{3.16}$$

This yields:

$$\frac{\partial U_k}{\partial u_m(t_k)} = -i \left(\int_0^{\Delta t_k} U_k(\tau) H_m U_k(-\tau) d\tau \right) U_k, \quad (3.17)$$

where

$$U_k(\tau) = \exp\{-i\tau H_{tot}(t_k)\}. \quad (3.18)$$

For small enough Δt_k the unitaries inside the integral Eq. (3.17) can then be expanded to first order in τ , leading to:

$$\begin{aligned} \int_0^{\Delta t_k} U_k(\tau) H_m U_k(-\tau) d\tau &\approx \int_0^{\Delta t_k} (1 - i\tau H_{tot}(t_k)) H_m (1 + i\tau H_{tot}(t_k)) d\tau \\ &\approx \int_0^{\Delta t_k} H_m - i\tau [H_{tot}(t_k), H_m] d\tau. \end{aligned} \quad (3.19)$$

This approximation requires:

$$\Delta t_k \ll \|H_{tot}(t_k)\|_2^{-1} \forall k, \quad (3.20)$$

in order to be valid. By computing the integral and dropping the Δt^2 term we find:

$$\int_0^{\Delta t_k} U_k(\tau) H_m U_k(-\tau) d\tau \approx \Delta t H_m. \quad (3.21)$$

Thus, a first order approximation of the derivative of unitary propagator U_k with respect to the control fields $u_m(t_k)$ can be evaluated as:

$$\frac{\partial U_k}{\partial u_m(t_k)} \approx -i \Delta t_k H_m U_k. \quad (3.22)$$

By inserting Eqs. (3.22) into (3.15), the gradient expression for the quality function Φ_1 can be yielded:

$$\nabla_{k,m} \Phi_1 = -\text{Retr}\{\lambda_{K+1:k+1} i \Delta t_k H_m U_{k:0}\} / N. \quad (3.23)$$

Similarly, we have the following approximate gradient term for the quality function Φ_2 :

$$\nabla_{k,m} \Phi_2 = -2 \text{Retr}\{\lambda_{K+1:k+1} i \Delta t_k H_m U_{k:0}\} \text{tr}\{U_{k:0} \lambda_{K+1:k+1}\} / N^2. \quad (3.24)$$

B: Computing the Exponential Derivative by a Finite-Difference Method

The derivative of a general function f at a point x is defined by the limit:

$$\frac{\partial f}{\partial x} = \lim_{\epsilon \rightarrow 0} \frac{f(x + \epsilon) - f(x)}{\epsilon}. \quad (3.25)$$

When ϵ is a fixed non-zero value, the fraction on the right-hand side is an approximation of the derivative of f . In our case, Eq. (3.25) becomes:

$$\nabla_{k,m} \Phi_1 = \frac{\text{Retr}\{\lambda_{K+1:k+1} P_{k,m} U_{k-1:0}\} / N - \Phi_1}{\epsilon}, \quad (3.26)$$

with

$$P_{k,m} = \exp\{-i\Delta t_k (H_{tot}(t_k) + \epsilon H_m)\}. \quad (3.27)$$

For Φ_2 we find:

$$\nabla_{k,m} \Phi_2 = \frac{|\text{tr}\{\lambda_{K+1:k+1} P_{k,m} U_{k-1:0}\}|^2 / N^2 - \Phi_2}{\epsilon}. \quad (3.28)$$

Numerically, this derivative can be set to reach the best machine precision when ϵ is sufficiently small. Typically, when choosing ϵ to be on the order of 10^{-7} , we can find the best results.

Step 8: Update Controls

There exist many methods for updating the control vector in an iterative optimization scheme which include 1) Steepest ascent 2) Newton and quasi-Newton methods 3) Conjugate gradients 4) Line search and etc. For a more detailed information into these four methods see [74], [75], [76] and [77]. Here, we will explain only the first method.

Steepest Ascent

Steepest ascent is a first-order method for computing the control vector for the next iteration. Only the gradient information is used to determine the new vector. In the case

of our pulse optimization, the control amplitudes in the next iteration are:

$$u_m(t_k) \rightarrow u_m(t_k) + \gamma \nabla_{k,m} \Phi. \quad (3.29)$$

Here, γ is a stepsize parameter. If the stepsize is sufficiently small at each iteration, and exact gradients are used, the algorithm is guaranteed to converge monotonically to a local maximum of the quality function.

Step 9: Check Stopping Criteria

Iterate steps 2 through 8 until $\Phi > 1 - \epsilon$. The goal tolerance ϵ is introduced because we cannot expect a numerical method to reach a final fidelity of exactly 1. The algorithm is terminated if the change in the performance index Φ is smaller than a chosen threshold value. In practice, several other stopping criteria are applied, e.g., an upper limit for the number of iterations, and a lower limit for the norm of the gradient or the step.

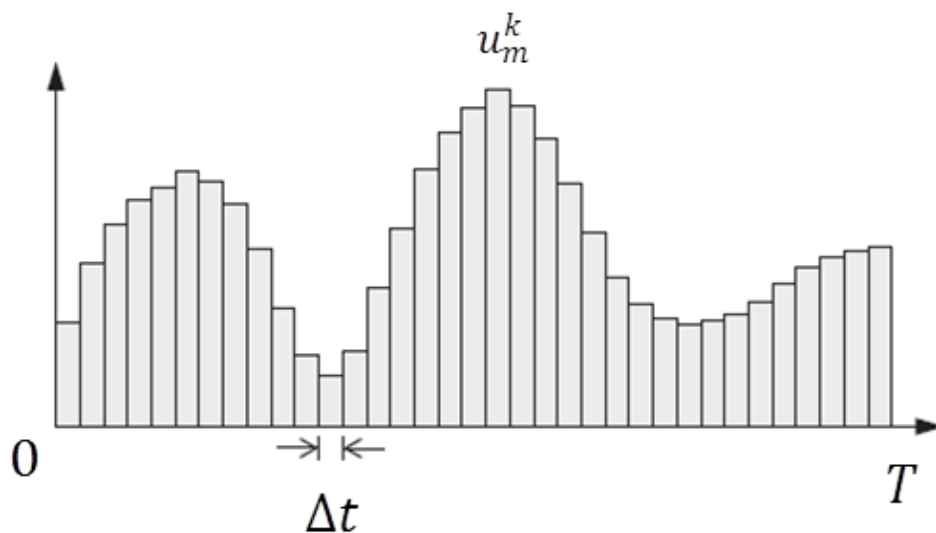


Fig. 3.1: The m 'th control function is represented by a piecewise-constant pulse sequence consisting M scalar control amplitudes u_m .

SECTION: 3.4

Robustness

The GRAPE algorithm can be configured to search for controls which are robust under the variation of any system parameters. Consider a parameter δ_r which appears in the Hamiltonian and therefore influences the resulting unitary at time T , $U_r(T)$. Let us assume the quality function $\Phi\{U(T)\}$ is normalized to have a maximum of 1. The average,

$$\bar{\Phi}(T) := \frac{1}{R} \sum_{r=1}^R \Phi\{U_r(T)\}, \quad (3.30)$$

then achieves a maximum of 1 if and only if $\Phi\{U_r(T)\}$ is maximized for each and every choice of δ_r . Any of the previous quality functions can be extended in this fashion to search for robust controls. It may be that T must be increased for such controls to exist, however, or that some compromise between maximum fidelity and robustness is necessary.

In this thesis, in order to implement NMR experiments, we have used some pulses generated by the GRAPE algorithm. We have implemented some single qubit operations and unitary gates by applying radio-frequency pulses generated using the GRAPE algorithm to rotate spins. The GRAPE algorithm of finding pulses is for coherently controlling a system of qubits and implementing precise unitary transformations in NMR.

For the purpose of our experiment, the GRAPE code was used to find an optimal pulse for a given unitary operation (the Controlled-NOT gate, for example). A key parameter in the use of the GRAPE algorithm is the total duration of the pulse. The total duration of each modulated sequence was between $1ms$ to $2ms$ for single qubit unitaries and a pulse time comparable to the scalar coupling constant ($\frac{1}{2J_{ij}}$) for two-qubit operations between spins i and j . Tables (3.1) and (3.2) show the control parameters for each GRAPE pulse used in this these. The Fidelity is given by:

$$F = \frac{|Tr(U_{sim}U_{ideal}^\dagger)|}{\sqrt{Tr(U_{sim}U_{sim}^\dagger)Tr(U_{ideal}U_{ideal}^\dagger)}}, \quad (3.31)$$

where U_{sim} and U_{ideal} are the simulated unitary by using the output of the pulse optimization and the desired target unitary, respectively.

Pulse	Time step	Total time	$\frac{1}{2J}$	Fidelity
$R_x^1(\frac{\pi}{2})$	1 μs	1000 μs	-	0.9999
$R_x^2(\frac{\pi}{2})$	1.5 μs	1500 μs	-	1
Hadamard for first qubit	1 μs	1000 μs	-	0.9999
Hadamard for second qubit	1.5 μs	1500 μs	-	1
$CNOT_{12}$	2 μs	4000 μs	2.5 ms	0.9999
$CNOT_{23}$	3 μs	6000 μs	4.9 ms	0.9999

Tab. 3.1: Control parameters input into the GRAPE algorithm for trichloroethylene molecule (see Chapter (5)).

Pulse	Time step	Total time	Fidelity
$R_x^1(\frac{\pi}{2})$	1 μs	1000 μs	0.9999
$R_x^2(\frac{\pi}{2})$	1 μs	1000 μs	1
$R_x^3(\frac{\pi}{2})$	1 μs	1000 μs	0.9999

Tab. 3.2: Control parameters input into the GRAPE algorithm for iodotrifluoroethylene molecule (see Chapter (6)).

For example, Fig. (3.2) shows phase and amplitude obtained in the optimization of 90 degree pulse applied to the second qubit about the x axis ($R_x^2(\frac{\pi}{2})$) in the iodotrifluoroethylene molecule. Also, the robustness of the pulse to radio frequency field inhomogeneities is shown on Fig. (3.3).

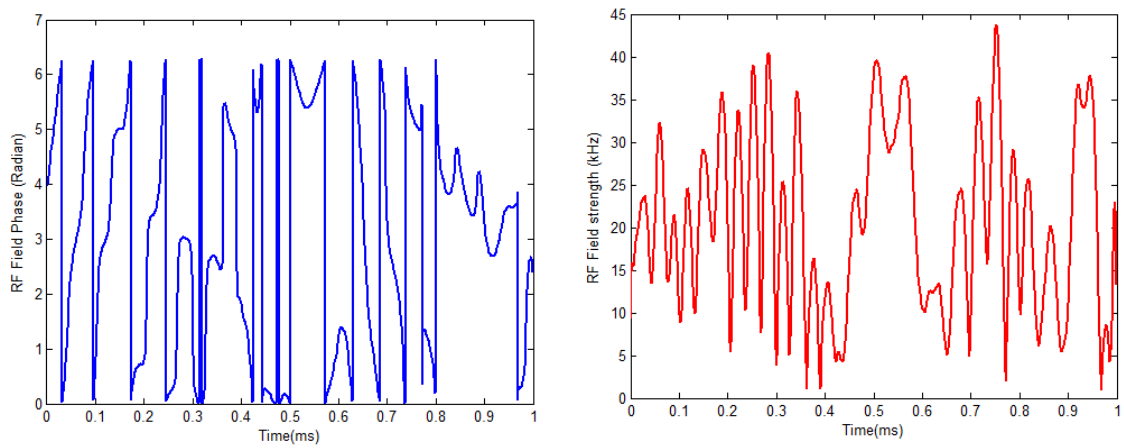


Fig. 3.2: The quadrature components of the fluorine control fields for a GRAPE pulse that implements a 90 degree rotation on $F2$ in the iodotrifluoroethylene molecule (see Chapter (6)). The total duration of the pulse is $1000\mu s$.

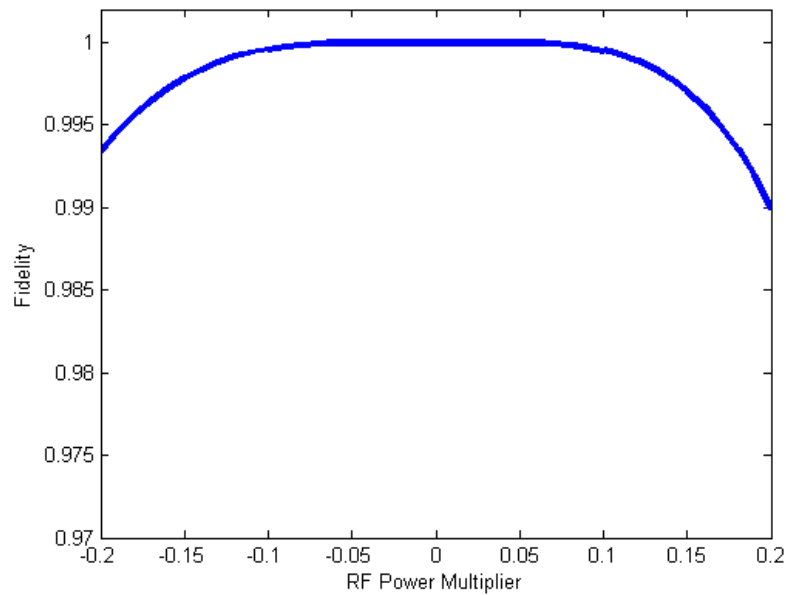


Fig. 3.3: The robustness of the pulse to radio frequency field inhomogeneities. The amplitude in the Fig. (3.2) is changed and then the fidelity (the overlap of the output state from the simulated unitary and the output from the ideal unitary) is calculated.

4

Quantum State Tomography For Strongly Coupled Nuclear Spin Systems: Theoretical Treatment

Result I:

In quantum information processing, an important step is to characterize the system state at the end of a computational process. This step makes it possible to measure the fidelity of an initial state or often the implementation of a logic gate, or in the estimation of errors in the experimental implementation. This procedure of reconstruction of the density matrix of a system is known as the Quantum State Tomography (QST). The processes of quantum state tomography require a set of measurements on the system, since experimentally only a small part of the $4^N - 1$ elements of the density matrix are accessible.

Quantum State Tomography is the process of completely characterizing the density matrix of a quantum system. The first QST on NMR system was reported by Chuang et al.[21] for systems of two coupled spins $1/2$. Later different methods were proposed for quadrupolar nuclei [22, 23] and n weakly coupled spins [25].

In this chapter, we present results on QST in a system with strongly coupled spins, known in NMR literature as “ AB ” and “ ABX ” systems. We have found that the number of experiments necessary to perform QST in an “ ABX ” system can be reduced with respect to three weakly coupled qubits. Therefore our method can reduce the experimental effort required for the complete density matrix reconstruction.

SECTION: 4.1

Time Domain Signal

In liquid state NMR a sample in a small tube is placed in a region of strong magnetic field, and radio frequency (RF) pulses are applied in order to induce transitions between

the energy levels of the nuclear spin system [6]. The spin Hamiltonian in the laboratory frame describes the interaction of the nuclear spins with a static magnetic field, the Zeeman interaction, and the interaction among the spins, the indirect J coupling:

$$H = \sum_{k=1}^n \omega_k I_{kz} + \sum_{k,j(k<j)}^n 2\pi J_{kj} (I_{kx} I_{jx} + I_{ky} I_{jy} + I_{kz} I_{jz}), \quad (4.1)$$

where I_{km} is the m -component of the nuclear spin angular momentum operator for spin k , $\omega_k/2\pi$ is the Larmor frequency and J_{kj} is the coupling strength between the spins k and j . I_x, I_y , and I_z are the spin components which relate to the well-known Pauli matrices as:

$$I_x = \frac{\hbar}{2} \sigma_x, \quad I_y = \frac{\hbar}{2} \sigma_y, \quad I_z = \frac{\hbar}{2} \sigma_z, \quad (4.2)$$

where, in matrix notation,

$$\sigma_x \equiv \begin{bmatrix} 0 & 1 \\ 1 & 0 \end{bmatrix}, \quad \sigma_y \equiv \begin{bmatrix} 0 & -i \\ i & 0 \end{bmatrix}, \quad \sigma_z \equiv \begin{bmatrix} 1 & 0 \\ 0 & -1 \end{bmatrix}. \quad (4.3)$$

When $2\pi|J_{kj}| \ll |\omega_k - \omega_j|$, the system is said to be weakly coupled, and the Hamiltonian in the laboratory frame can be approximated by [18]:

$$H = \sum_{k=1}^n \omega_k I_{kz} + \sum_{k,j(k<j)}^n 2\pi J_{kj} I_{kz} I_{jz}. \quad (4.4)$$

During the application of quantum gates, the natural evolution of the system, driven either by the Hamiltonian (4.4) or (4.1), deviates the actual operation implemented from the target one. One approach to achieve good control consists of using an approximation that decomposes the actual operation into the ideal target operation, driven by the interaction of the spins with radio frequency magnetic fields, followed and preceded by error terms which can be tracked and corrected. In weakly coupled systems this decomposition is easier, since all terms of the Hamiltonian (Eq. (4.4)) commute with each other, allowing precise quantum operations using standard shaped pulses [20]. With this approach imple-

mentations of quantum computing have been performed on liquid state NMR samples with seven [8, 9] and twelve qubits [7]. For implementing high fidelity quantum gates and protocols on strongly coupled systems, usually, optimal control techniques must be employed.

Then, a signal due to the precessing magnetization of the sample is detected. The detected signal in NMR is the so called Free Induction Decay (FID), which corresponds to an electric current induced in tuned pick-up coils. The detected signal stores information about the instantaneous transverse magnetization of the sample during the detection process. The observed signal, in the time domain, is defined as the expectation value:

$$S(t) = \text{Tr}\{\rho(t) \sum_k I_{k+}\} = \text{Tr}\{\rho(t) \sum_k (I_{kx} + iI_{ky})\}, \quad (4.5)$$

where $I_{k+} = I_{kx} + iI_{ky}$, and I_{kx} and I_{ky} are spin operators proportional to the x and y components of magnetization due to spin k , and $\rho(t)$ is the reduced density operator at time t during the FID.

The density operator at time t is given by the transformation of an initial density operator ρ_0 at $t = 0$ under the propagator U_p , imposed by applied pulses. As it is usually done [6] we will assume that, during the application of the radio frequency pulses, we can neglect the evolution caused by the internal Hamiltonian, and consider only the radio frequency Hamiltonian. After the pulses, the system evolves under the natural Hamiltonian:

$$\rho(t) = e^{-iHt} U_p \rho_0 U_p^\dagger e^{+iHt}. \quad (4.6)$$

In QST, the Hamiltonian of the system is given and we would like to estimate the density operator at the beginning of the measurement. It is worth to mention that U_p and the Hamiltonian H , usually do not commute with each other. By substituting Eqs. (4.6) into (4.5) and making use of the linearity of the trace and its invariance with respect to cyclic permutation of operators in a product, the observed time domain signal can be

written as a function of the initial density matrix, ρ_0 , of n spins as [25]:

$$\begin{aligned} S_p(t) &= \sum_{k=1}^n S_{p,k}(t) = \sum_{k=1}^n \text{Tr}\{\rho_0 O_{p,k}(t)\} \\ &= \sum_{k=1}^n \text{Tr}\{\rho_0 U_p^\dagger e^{+iHt} I_{k+} e^{-iHt} U_p\}, \end{aligned} \quad (4.7)$$

where k and p are the spin number and the preparatory pulses (see next section), respectively. An interesting point from Eq. (4.7) is that the FID can be used to investigate the properties of the density matrix of the system, ρ_0 .

The spectrum is obtained by taking the Fourier transform of Eq. (4.7):

$$\bar{S}_{p,k}(\omega) = \frac{1}{T} \int_0^T e^{-i\omega t} S_{p,k}(t) dt. \quad (4.8)$$

In the weak coupling limit, the observed spectrum is called first-order spectrum and the intensities of resonance lines in a multiplet are uniform. For first order system, J coupling and chemical shift values are directly measurable from line positions. Upon strong coupling, second-order effects appear and the intensities of the NMR peaks vary across the multiplet. If first order behavior assume here we will find incorrect coupling constants and chemical shifts. Furthermore, additional transitions, not allowed in the weakly coupled systems, can leave the spectra of strongly coupled spins more complex to analyze. It's notable that the FID has information on various frequencies of the spectrum.

In this chapter, we will assume two strongly coupled spin- $\frac{1}{2}$ systems, “ AB ” and “ ABX ” spin systems. For this reason, in order to evaluate $O_{p,k}(t)$, some mathematical preliminaries are necessary. The Hamiltonian matrix for strongly coupled spin systems is not diagonal and it will be difficult to produce an exponential matrix operator. On the other hand, diagonal matrices allow easy construction of exponential operator matrices. For these reasons, we should diagonalize the Hamiltonian.

According to the unitary transformation (see Appendix (A)):

$$\hat{B} = \hat{T}^{-1} \hat{A} \hat{T}, \quad (4.9)$$

we have:

$$H_{diag} = \hat{V}^{-1} H \hat{V}, \quad (4.10)$$

or

$$H = \hat{V} H_{diag} \hat{V}^{-1}, \quad (4.11)$$

where V is the unitary matrix of eigenvectors.

By replacing Eqs. (4.11) into (4.7), the signal can be written as:

$$S_p(t) = \sum_{k=1}^n Tr\{\rho_0 U_p^{-1} V e^{+iH_{diag}t} V^{-1} I_{k+} V e^{-iH_{diag}t} V^{-1} U_p\}. \quad (4.12)$$

SECTION: 4.2

Product-Operator Basis

To perform QST, we consider the expansion of density matrices in terms of the product operators. The basis which is generally used in describing the NMR experiments is the product-operator basis. This basis is formed by tensor products of nuclear spin operators given by:

$$\{I_0, I_1, I_2, I_3\} = \{I, 2I_x, 2I_y, 2I_z\}, \quad (4.13)$$

that denotes a basis for the space of linear operators on the single-spin- $\frac{1}{2}$ Hilbert space.

The density matrix of a single qubit is therefore written as:

$$\rho = \frac{1}{2}I + c_x I_x + c_y I_y + c_z I_z. \quad (4.14)$$

The reconstruction of the density matrix relies on the determination of each product operator coefficient (c_x, c_y, c_z in the above example). However it is not possible to characterize all coefficients in a single experiment. The operators I_x and I_y are observables and their coefficients can be determined directly by the NMR signal. Although the I_z term is not observable in the FID signal, it can still be determined by rotating the spin by 90 degree to convert the I_z term into an observable one. Note that the I term cannot be observed by any NMR experiment and therefore all NMR QST techniques can only determine the so called deviation density matrix $\Delta\rho = \rho - I/D$, where D is the Hilbert space dimension. For n 1/2-spins, each product basis operator is defined as [78]:

$$P_{n,s} = \bigotimes_{k=1}^n I_{q_k(s)}, \quad (4.15)$$

where $q_k(s)$ is the k th digit of the integer s represented in base-4 where $0 \leq s \leq 4^n - 1$. For example, the basis for two-spin system ($P_{(2)}$) is given by:

$$\begin{aligned} & \{I \otimes I, I \otimes 2I_x, I \otimes 2I_y, I \otimes 2I_z, \\ & 2I_x \otimes I, 2I_x \otimes 2I_x, 2I_x \otimes 2I_y, 2I_x \otimes 2I_z, \\ & 2I_y \otimes I, 2I_y \otimes 2I_x, 2I_y \otimes 2I_y, 2I_y \otimes 2I_z, \\ & 2I_z \otimes I, 2I_z \otimes 2I_x, 2I_z \otimes 2I_y, 2I_z \otimes 2I_z\}. \end{aligned} \quad (4.16)$$

To make the notation of Eq. (4.15) clearer, the element of the basis operator $P_{(2),21}$ is given by the element of the third row and second column, $2I_y \otimes 2I_x$. These products form a “complete set of basis operators” of a two spin 1/2 system. The number of 16 different operators is equal to the square of the Hilbert space dimensionality. We denote the basis elements as a product of matrices instead of direct product \otimes , with $P_{(2),21} = 4I_y I_x$, for example. This is the notation that will be used from now on.

The product-operator basis $P_{(n)}$ is orthonormal with respect to the scalar product in Hilbert-Schmidt space:

$$(A, P) \equiv \frac{1}{2^n} \text{Tr}\{A^\dagger P\}, \quad (4.17)$$

where n is the number of spins. This property of orthonormality allows us to expand uniquely any density matrix in terms of this basis:

$$\rho = \frac{1}{2^n} I_D + \sum_{s=1}^{4^n-1} \rho_s P_{n,s}, \quad (4.18)$$

where D in I_D denotes the order of the identity matrix and ρ_s is a real number given by:

$$\rho_s = (P_{n,s}^\dagger, \rho) = (P_{n,s}, \rho) = \text{Tr}(\rho P_{n,s}). \quad (4.19)$$

with the self-adjointness property $P_{n,s}^\dagger = P_{n,s}$.

For weakly coupled spins, the Fourier intensities of the NMR spectrum (Eq. (4.8)) are related to the coefficients ρ_s by a set of linear equations $\bar{S}_p = \mathfrak{M} \times \mathcal{C}$, where $\bar{S}_p = (S_p(\Omega_1), S_p(\Omega_2), \dots)^T$ is a column vector of Fourier intensities, observed at frequencies Ω_m , \mathcal{C} is a vector containing some coefficients of the expansion (Eq. (4.18)) and the matrix \mathfrak{M} connects the experimental observed quantity \bar{S}_p to the coefficients to be determined [25]. Note that, in order to distinguish two experiments with different applied pulses, the signal is labeled with the index p . The exact form of \mathfrak{M} depends on the spin system. For weakly coupled systems, \mathfrak{M} is given in [25]. In some cases, it is not easy to determine analytical expressions for \mathfrak{M} , and numerical calculations must be used. By inverting the system of equations, we can determine the coefficients ρ_s . As in the single qubit case, only a few coefficients can be determined in a single run. The remaining coefficients are determined by converting non-observable terms into observable ones by applying a preparatory set of operations $\{1, X, Y\}$ to each spin, where “1” denotes no pulse, and X and Y denote selective pulses that rotate the spin’s magnetization by 90 degree about the x and y axis, respectively. As there are n spins, there will be 3^n possible preparatory operations. Nevertheless, the minimum set of experiments necessary for QST in weakly coupled systems can be substantially reduced, as discussed in [25]. In strongly

coupled systems the results derived for weakly coupled systems cannot be applied and one needs to recalculate \mathfrak{M} to properly relate the coefficients of the expansion (Eq. (4.18)) and the observed Fourier intensities of the NMR spectra (Eq. (4.8)). Next, we will discuss quantum state tomography in two strongly coupled systems and, in particular, show how the number of experiments required for performing a complete tomography can be reduced in the case of “*ABX*” systems.

SECTION: 4.3

Two Nuclei “*AB*” Spin System

The simplest case to be considered is two spins strongly coupled, in NMR nomenclature called “*AB*” spin system. In NMR, an “*AB*” spin system is comprised by two strongly coupled spins and can be found when the chemical shift difference is comparable to the coupling constant between “*A*” and “*B*” spins. Examples of such molecules are shown in Table (4.2). Its Hamiltonian in the laboratory frame can be written as:

$$H = \omega_1 I_{1z} + \omega_2 I_{2z} + 2\pi J_{12}(I_{1x}I_{2x} + I_{1y}I_{2y} + I_{1z}I_{2z}). \quad (4.20)$$

Here, subscripts 1 and 2 refer to “*A*” and “*B*” respectively. I_{1m} and I_{2m} are the m components of the nuclear spin angular momentum operators for “*A*” and “*B*” nuclei; ω_1 and ω_2 are the precession frequencies of “*A*” and “*B*” nuclei and J_{12} is the scalar coupling constant. The four eigenstates of the “*AB*” spin system are shown in Table (4.1). The energy level diagram with the eigenstates of the “*AB*” spin system is shown in Fig. (4.1). In the weak coupling limit (when $2\pi|J_{12}| \ll |\omega_1 - \omega_2|$), the angle $\theta \approx 0$ and the four eigenstates will be $|00\rangle$, $|01\rangle$, $|10\rangle$ and $|11\rangle$, where $|0\rangle$ and $|1\rangle$ denote the eigenstates of the spin operator I_z . In this case the spectrum consists of a pair of doublets with equal amplitudes. If the chemical shift is zero, we have a pair of equivalent nuclei, and only a single line will be observed. But in the strong coupling regime the spectrum changes from two simple doublets into a symmetrical group of four lines, the inner pair of lines being stronger than the outer (Fig. (4.2)).

Line	Eigenstate
1	$ \alpha\alpha\rangle$
2	$\cos\theta \alpha\beta\rangle + \sin\theta \beta\alpha\rangle$
3	$-\sin\theta \alpha\beta\rangle + \cos\theta \beta\alpha\rangle$
4	$ \beta\beta\rangle$

Tab. 4.1: The four eigenstates for two nuclei “AB”. Where $\alpha = 0$, $\beta = 1$ and $\theta = \frac{1}{2} \tan^{-1}\left(\frac{2\pi J_{12}}{\omega_1 - \omega_2}\right)$ is the mixing angle.

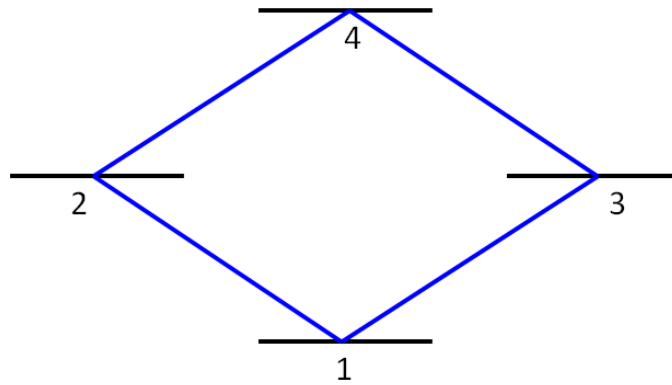
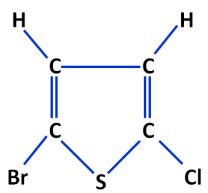
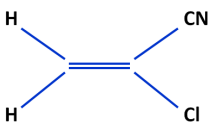
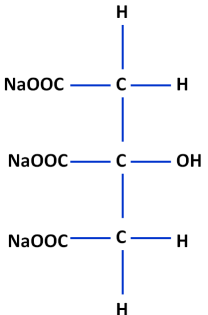
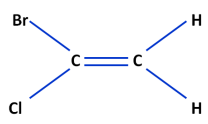


Fig. 4.1: Energy level diagram of an “AB” spin system. The numbers correspond to the eigenstates given in Table (4.1).

Formula	Name
	<ul style="list-style-type: none"> • 2-Bromo-5-Chlorothiophene (C_4H_2BrClS)
	<ul style="list-style-type: none"> • 2-Chloroacrylonitrile (C_3H_2ClN)
	<ul style="list-style-type: none"> • Trisodium Citrate ($C_6H_5O_7Na_3$)
	<ul style="list-style-type: none"> • 1-Bromo-1-Chloroethene (C_2H_2BrCl)

Tab. 4.2: Examples of NMR “AB” spin systems.

Hence, for two strongly coupled spins, the Hamiltonian in the matrix form can be written as:

$$H = \begin{bmatrix} \frac{(\omega_1 + \omega_2)}{2} + \frac{\pi J_{12}}{2} & 0 & 0 & 0 \\ 0 & \frac{(\omega_1 - \omega_2)}{2} - \frac{\pi J_{12}}{2} & \pi J_{12} & 0 \\ 0 & \pi J_{12} & -\frac{(\omega_1 - \omega_2)}{2} - \frac{\pi J_{12}}{2} & 0 \\ 0 & 0 & 0 & -\frac{(\omega_1 + \omega_2)}{2} + \frac{\pi J_{12}}{2} \end{bmatrix}. \quad (4.21)$$

The Hamiltonian matrix is not diagonal and we aim to diagonalize this matrix. We

recognize that the first and last terms of the Hamiltonian will not change a diagonalization procedure as there are no off-diagonals associated with them. Only the second and third terms will change. Using the unitary transformation,

$$H_{diag} = \hat{V}^{-1} H \hat{V}, \quad (4.22)$$

Hamiltonian for “ AB ” spin system can be diagonalized. Where V is the unitary matrix that it contains eigenvectors of “ AB ” spin systems and can be chosen as:

$$V = \begin{bmatrix} 1 & 0 & 0 & 0 \\ 0 & \cos \theta & -\sin \theta & 0 \\ 0 & \sin \theta & \cos \theta & 0 \\ 0 & 0 & 0 & 1 \end{bmatrix}, \quad V^{-1} = \begin{bmatrix} 1 & 0 & 0 & 0 \\ 0 & \cos \theta & \sin \theta & 0 \\ 0 & -\sin \theta & \cos \theta & 0 \\ 0 & 0 & 0 & 1 \end{bmatrix}, \quad (4.23)$$

where $\hat{V}\hat{V}^{-1} = \hat{1}$ and $\theta = \frac{1}{2} \tan^{-1}(\frac{2\pi J_{12}}{\omega_1 - \omega_2})$. Then, the fully diagonalized Hamiltonian matrix by using Eq. (4.22) is as follows:

$$H_{diag} = \begin{bmatrix} \frac{(\omega_1 + \omega_2)}{2} + \frac{\pi J_{12}}{2} & 0 & 0 & 0 \\ 0 & a & b & 0 \\ 0 & b & c & 0 \\ 0 & 0 & 0 & -\frac{(\omega_1 + \omega_2)}{2} + \frac{\pi J_{12}}{2} \end{bmatrix}, \quad (4.24)$$

where

$$a = \frac{(\omega_1 - \omega_2)}{2} \cos(2\theta) - \pi J_{12} \sin(2\theta) - \frac{\pi J_{12}}{2},$$

$$b = -\frac{(\omega_1 - \omega_2)}{2} \sin(2\theta) + \pi J_{12} \cos(2\theta),$$

$$c = -\frac{(\omega_1 - \omega_2)}{2} \cos(2\theta) + \pi J_{12} \sin(2\theta) - \frac{\pi J_{12}}{2}.$$

If this matrix is to be diagonal then:

$$b = 0 \Rightarrow -\frac{(\omega_1 - \omega_2)}{2} \sin(2\theta) + \pi J_{12} \cos(2\theta) = 0, \quad (4.25)$$

$$\tan(2\theta) = \frac{2\pi J_{12}}{(\omega_1 - \omega_2)} \Rightarrow \theta = \frac{1}{2} \tan^{-1}\left(\frac{2\pi J_{12}}{\omega_1 - \omega_2}\right). \quad (4.26)$$

Using the general equation for eigenvalues of 2×2 matrix, the eigenvalues are:

$$\lambda = \mp \frac{1}{2} \sqrt{4(\pi J_{12})^2 + (\omega_1 - \omega_2)^2} - \frac{\pi J_{12}}{2}, \quad (4.27)$$

and therefore, the full diagonalized Hamiltonian matrix is:

$$H_{diag} = \begin{bmatrix} \frac{(\omega_1 + \omega_2)}{2} + \frac{\pi J_{12}}{2} & 0 & 0 & 0 \\ 0 & \frac{M}{2} - \frac{\pi J_{12}}{2} & 0 & 0 \\ 0 & 0 & -\frac{M}{2} - \frac{\pi J_{12}}{2} & 0 \\ 0 & 0 & 0 & -\frac{(\omega_1 + \omega_2)}{2} + \frac{\pi J_{12}}{2} \end{bmatrix}, \quad (4.28)$$

where $M = \sqrt{4(\pi J_{12})^2 + (\omega_1 - \omega_2)^2}$.

For “ AB ” spin $1/2$ systems, there are only four allowed transitions. The allowed transitions of the “ AB ” spin system with transition energies and relative intensities are given in Table (4.3). The relative intensities are proportional to the squares of the appropriate matrix elements of the x component of the spin $I_x(A) + I_x(B)$. Thus for the transition $2 \rightarrow 1$, for example, we have:

$$[\cos \theta(\alpha\beta) | I_x(A) + I_x(B) | \alpha\alpha]^2 = \frac{1}{4}(\cos \theta + \sin \theta)^2 = \frac{1}{4}(1 + \sin 2\theta). \quad (4.29)$$

Transition	Energy	Relative intensity
1)3 \rightarrow 1	$\frac{(\omega_1 + \omega_2)}{2} + \frac{M}{2} + \pi J_{12}$	$1 - \sin(2\theta)$
2)4 \rightarrow 2	$\frac{(\omega_1 + \omega_2)}{2} + \frac{M}{2} - \pi J_{12}$	$1 + \sin(2\theta)$
3)2 \rightarrow 1	$\frac{(\omega_1 + \omega_2)}{2} - \frac{M}{2} + \pi J_{12}$	$1 + \sin(2\theta)$
4)4 \rightarrow 3	$\frac{(\omega_1 + \omega_2)}{2} - \frac{M}{2} - \pi J_{12}$	$1 - \sin(2\theta)$

Tab. 4.3: Transition Energies and Intensities for two nuclei spins “ AB ”.

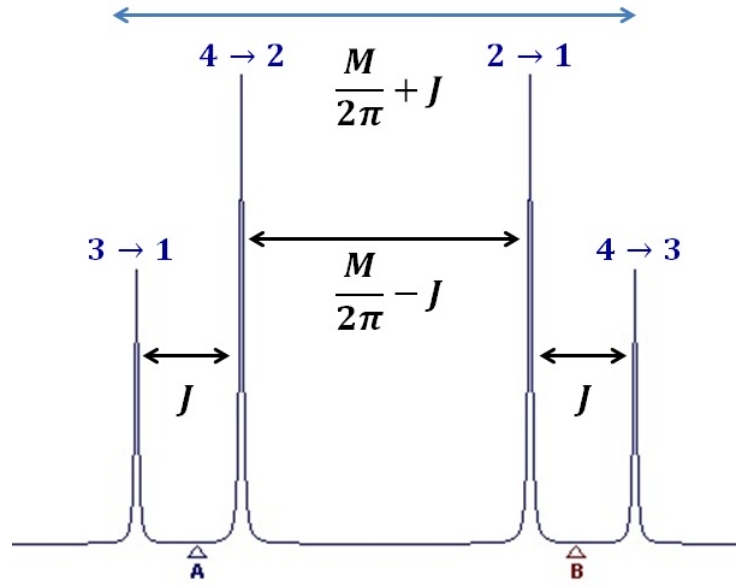


Fig. 4.2: Typical spectrum for two nuclei “AB”. It is assumed that $\omega_A > \omega_B$ and $J > 0$.

As we mentioned, the NMR signal can therefore be rewritten in terms of the diagonalized Hamiltonian, H_{diag} , as:

$$S_p(t) = \sum_{k=1}^n Tr\{\rho_0 U_p^{-1} V e^{+iH_{diag}t} V^{-1} I_{k+} V e^{-iH_{diag}t} V^{-1} U_p\}. \quad (4.30)$$

After an explicit calculation of Eq. (4.30) by substituting Eqs. (4.23) and (4.28) into (4.30), the signal due to spins “AB” can be written in the form:

$$S_{p,1,2}(t) = \frac{1}{4}(\bar{1}, \bar{2}, \bar{3}, \bar{4}) \times \begin{pmatrix} (2 \sin^2(\theta) - \sin(2\theta)) & -(2 \sin^2(\theta) - \sin(2\theta)) & (2 \cos^2(\theta) - \sin(2\theta)) & -(2 \cos^2(\theta) - \sin(2\theta)) \\ (2 \sin^2(\theta) + \sin(2\theta)) & (2 \sin^2(\theta) + \sin(2\theta)) & (2 \cos^2(\theta) + \sin(2\theta)) & (2 \cos^2(\theta) + \sin(2\theta)) \\ (2 \cos^2(\theta) + \sin(2\theta)) & -(2 \cos^2(\theta) + \sin(2\theta)) & (2 \sin^2(\theta) + \sin(2\theta)) & -(2 \sin^2(\theta) + \sin(2\theta)) \\ (2 \cos^2(\theta) - \sin(2\theta)) & (2 \cos^2(\theta) - \sin(2\theta)) & (2 \sin^2(\theta) - \sin(2\theta)) & (2 \sin^2(\theta) - \sin(2\theta)) \end{pmatrix} \times \begin{pmatrix} Tr\{\rho_0 \tilde{I}_{1+}\} \\ Tr\{\rho_0 2\tilde{I}_{1+}\tilde{I}_{2z}\} \\ Tr\{\rho_0 \tilde{I}_{2+}\} \\ Tr\{\rho_0 2\tilde{I}_{1z}\tilde{I}_{2+}\} \end{pmatrix}, \quad (4.31)$$

where

$$\begin{aligned}\bar{\mathcal{I}} &= \frac{(\omega_1 + \omega_2)}{2} - \frac{M}{2} - \pi J_{12}, & \bar{\mathcal{Q}} &= \frac{(\omega_1 + \omega_2)}{2} - \frac{M}{2} + \pi J_{12}, \\ \bar{\mathcal{P}} &= \frac{(\omega_1 + \omega_2)}{2} + \frac{M}{2} - \pi J_{12} & \text{and} & \quad \bar{\mathcal{A}} = \frac{(\omega_1 + \omega_2)}{2} + \frac{M}{2} + \pi J_{12}.\end{aligned}$$

Here, $\tilde{A} = U_p^{-1} A U_p$ is the operator A transformed by the unitary operator U_p^{-1} due to the applied preparatory pulses. Taking the Fourier transform of Eq. (4.31) at the four observed frequencies, we find that:

$$\begin{aligned}& \begin{pmatrix} \bar{S}_{p,1,2}\left(\frac{\omega_1 + \omega_2}{2} - \frac{M}{2} - \pi J_{12}\right) \\ \bar{S}_{p,1,2}\left(\frac{\omega_1 + \omega_2}{2} - \frac{M}{2} + \pi J_{12}\right) \\ \bar{S}_{p,1,2}\left(\frac{\omega_1 + \omega_2}{2} + \frac{M}{2} - \pi J_{12}\right) \\ \bar{S}_{p,1,2}\left(\frac{\omega_1 + \omega_2}{2} + \frac{M}{2} + \pi J_{12}\right) \end{pmatrix} = \frac{1}{4} \times \\ & \begin{pmatrix} (2 \sin^2(\theta) - \sin(2\theta)) & -(2 \sin^2(\theta) - \sin(2\theta)) & (2 \cos^2(\theta) - \sin(2\theta)) & -(2 \cos^2(\theta) - \sin(2\theta)) \\ (2 \sin^2(\theta) + \sin(2\theta)) & (2 \sin^2(\theta) + \sin(2\theta)) & (2 \cos^2(\theta) + \sin(2\theta)) & (2 \cos^2(\theta) + \sin(2\theta)) \\ (2 \cos^2(\theta) + \sin(2\theta)) & -(2 \cos^2(\theta) + \sin(2\theta)) & (2 \sin^2(\theta) + \sin(2\theta)) & -(2 \sin^2(\theta) + \sin(2\theta)) \\ (2 \cos^2(\theta) - \sin(2\theta)) & (2 \cos^2(\theta) - \sin(2\theta)) & (2 \sin^2(\theta) - \sin(2\theta)) & (2 \sin^2(\theta) - \sin(2\theta)) \end{pmatrix} \\ & \times \begin{pmatrix} Tr\{\rho_0 \tilde{I}_{1+}\} \\ Tr\{\rho_0 2\tilde{I}_{1+}\tilde{I}_{2z}\} \\ Tr\{\rho_0 \tilde{I}_{2+}\} \\ Tr\{\rho_0 2\tilde{I}_{1z}\tilde{I}_{2+}\} \end{pmatrix}. \end{aligned} \quad (4.32)$$

As we can see from this equation, the intensities of the lines of an NMR spectrum are related to linear combinations of the expected values of specific observable, I_{1+} , $2I_{1+}I_{2z}$, I_{2+} and $2I_{1z}I_{2+}$ for the spectrum of spins 1 and 2 in an “ AB ” spin system. We invert Eq. (4.32) and construct the expectation values directly in terms of linear combinations of fitted data:

$$\begin{aligned}
 2^{1-n} \begin{pmatrix} -A & B & C & D \\ A & B & -C & D \\ D & C & B & -A \\ -D & C & -B & -A \end{pmatrix} & \begin{pmatrix} \bar{S}_{p,1,2}(\frac{\omega_1+\omega_2}{2} - \frac{M}{2} - \pi J_{12}) \\ \bar{S}_{p,1,2}(\frac{\omega_1+\omega_2}{2} - \frac{M}{2} + \pi J_{12}) \\ \bar{S}_{p,1,2}(\frac{\omega_1+\omega_2}{2} + \frac{M}{2} - \pi J_{12}) \\ \bar{S}_{p,1,2}(\frac{\omega_1+\omega_2}{2} + \frac{M}{2} + \pi J_{12}) \end{pmatrix} \\
 & = \frac{1}{2^n} \times \begin{pmatrix} Tr\{\rho_0 2\tilde{I}_{1+}\} \\ Tr\{\rho_0 4\tilde{I}_{1+}\tilde{I}_{2z}\} \\ Tr\{\rho_0 2\tilde{I}_{2+}\} \\ Tr\{\rho_0 4\tilde{I}_{1z}\tilde{I}_{2+}\} \end{pmatrix}, \tag{4.33}
 \end{aligned}$$

where $A = \frac{\sin\theta}{\cos\theta - \sin\theta}$, $B = \frac{\sin\theta}{\cos\theta + \sin\theta}$, $C = \frac{\cos\theta}{\cos\theta + \sin\theta}$, $D = \frac{\cos\theta}{\cos\theta - \sin\theta}$. In Eq. (4.33), n denotes the number of spins in each system and for an “ AB ” spin system, n is equal to 2.

In the weak coupling limit ($2\pi|J_{12}| \ll |\omega_1 - \omega_2|$), the angle $\theta \approx 0$, $M \approx |\omega_1 - \omega_2|$ and the results of Ref. [25] for two weakly coupled spins are obtained. Since the coefficients involved in Eq. (4.33) are the same as in the weak coupling case, we can use the minimal set of preparatory pulses derived in [25] to perform a complete quantum state tomography of “ AB ” systems.

SECTION: 4.4

Three Nuclei “ ABX ” Spin System

We can extend the results of the previous section to three-spin systems known in NMR nomenclature as “ ABX ” systems. In an “ ABX ” spin system, the chemical shift difference between the “ A ” and “ B ” nuclei is comparable to their coupling to each other and both are coupled to a “ X ” nucleus but the chemical shift of “ X ” nucleus is far away from the chemical shifts of the “ A ” and “ B ” nuclei. Examples of “ ABX ” systems are shown in Table (4.5). The Hamiltonian in the laboratory frame for an “ ABX ” spin system can be

written as:

$$\begin{aligned}
 H = \omega_1 I_{1z} + \omega_2 I_{2z} &+ \omega_3 I_{3z} + 2\pi J_{12}(I_{1x}I_{2x} + I_{1y}I_{2y} \\
 &+ I_{1z}I_{2z}) + 2\pi J_{13}(I_{1z}I_{3z}) + 2\pi J_{23}(I_{2z}I_{3z}), \quad (4.34)
 \end{aligned}$$

where 1, 2 and 3 labels are related to the nuclei “A”, “B” and “X”, respectively and I_{1m} , I_{2m} , and I_{3m} are the m components of the nuclear spin angular momentum operators for “A”, “B”, and “X” nuclei; ω_1 , ω_2 , and ω_3 are the precession frequencies of the nuclei “A”, “B”, and “X”, respectively. J_{12} is the coupling between “A” and “B” nuclei, J_{13} is the coupling between “A” and “X” nuclei, and J_{23} is the coupling between “B” and “X” nuclei. The eight eigenstates of the “ABX” spin system are given in Table (4.4). The energy level diagram of the “ABX” spin system is shown in Fig. (4.3).

Line	Eigenstate
1	$ \alpha\alpha\alpha\rangle$
2	$ \alpha\alpha\beta\rangle$
3	$\cos\theta^+ \alpha\beta\alpha\rangle + \sin\theta^+ \beta\alpha\alpha\rangle$
4	$-\sin\theta^+ \alpha\beta\alpha\rangle + \cos\theta^+ \beta\alpha\alpha\rangle$
5	$\cos\theta^- \alpha\beta\beta\rangle + \sin\theta^- \beta\alpha\beta\rangle$
6	$-\sin\theta^- \alpha\beta\beta\rangle + \cos\theta^- \beta\alpha\beta\rangle$
7	$ \beta\beta\alpha\rangle$
8	$ \beta\beta\beta\rangle$

Tab. 4.4: The eight eigenstates for three nuclei “ABX”. Where $\alpha = 0$, $\beta = 1$ and $\theta^\pm = \frac{1}{2} \tan^{-1} \frac{2\pi J_{12}}{\omega_1 - \omega_2 \pm \pi(J_{13} - J_{23})}$.

When the angles θ^\pm are small, the eigenstates reduce to $|\alpha\alpha\alpha\rangle$, $|\alpha\alpha\beta\rangle$, $|\alpha\beta\alpha\rangle$, $|\alpha\beta\beta\rangle$, $|\beta\alpha\alpha\rangle$, $|\beta\alpha\beta\rangle$, $|\beta\beta\alpha\rangle$ and $|\beta\beta\beta\rangle$.

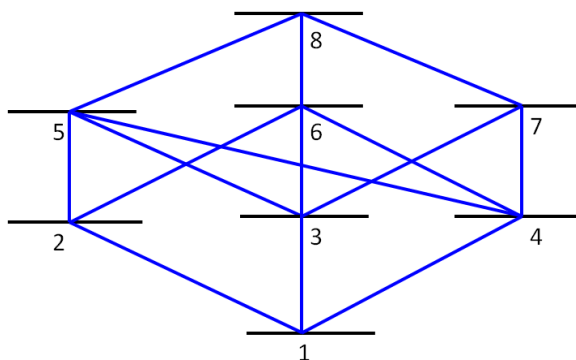


Fig. 4.3: Energy level diagram of an “ABX” spin system. The numbers correspond to the eigenstates given in Table (4.4).

Formula	Name
	<ul style="list-style-type: none"> Trichloroethylene (TCE) (C_2HCl_3)
	<ul style="list-style-type: none"> 2-Fluoro-4,6-Dichlorophenol ($C_6H_3FCl_2O$)
	<ul style="list-style-type: none"> 2,3-Lutidine (C_7H_9N)
	<ul style="list-style-type: none"> Styrene Oxide (C_8H_8O)

Tab. 4.5: Examples of NMR “ABX” spin systems.

For an “ ABX ” system, the Hamiltonian in the matrix form can be written as:

$$H = \begin{bmatrix} A_1 & 0 & 0 & 0 & 0 & 0 & 0 & 0 \\ 0 & A_2 & 0 & 0 & 0 & 0 & 0 & 0 \\ 0 & 0 & A_3 & 0 & A_7 & 0 & 0 & 0 \\ 0 & 0 & 0 & A_5 & 0 & A_9 & 0 & 0 \\ 0 & 0 & A_4 & 0 & A_8 & 0 & 0 & 0 \\ 0 & 0 & 0 & A_6 & 0 & A_{10} & 0 & 0 \\ 0 & 0 & 0 & 0 & 0 & 0 & A_{11} & 0 \\ 0 & 0 & 0 & 0 & 0 & 0 & 0 & A_{12} \end{bmatrix}, \quad (4.35)$$

where

$$\begin{aligned} A_1 &= \frac{(\omega_1 + \omega_2 + \omega_3)}{2} + \frac{\pi J_{12} + \pi J_{13} + \pi J_{23}}{2}, \\ A_2 &= \frac{(\omega_1 + \omega_2 - \omega_3)}{2} + \frac{\pi J_{12} - \pi J_{13} - \pi J_{23}}{2}, \\ A_3 &= \frac{(\omega_1 - \omega_2 + \omega_3)}{2} + \frac{-\pi J_{12} + \pi J_{13} - \pi J_{23}}{2}, \\ A_4 &= \pi J_{12}, \\ A_5 &= \frac{(\omega_1 - \omega_2 - \omega_3)}{2} + \frac{-\pi J_{12} - \pi J_{13} + \pi J_{23}}{2}, \\ A_6 &= \pi J_{12}, \quad A_7 = \pi J_{12}, \\ A_8 &= \frac{(-\omega_1 + \omega_2 + \omega_3)}{2} + \frac{-\pi J_{12} - \pi J_{13} + \pi J_{23}}{2}, \\ A_9 &= \pi J_{12}, \\ A_{10} &= \frac{(-\omega_1 + \omega_2 - \omega_3)}{2} + \frac{-\pi J_{12} + \pi J_{13} - \pi J_{23}}{2}, \\ A_{11} &= \frac{(-\omega_1 - \omega_2 + \omega_3)}{2} + \frac{\pi J_{12} - \pi J_{13} - \pi J_{23}}{2}, \\ A_{12} &= \frac{(-\omega_1 - \omega_2 - \omega_3)}{2} + \frac{\pi J_{12} + \pi J_{13} + \pi J_{23}}{2}. \end{aligned}$$

In an “ ABX ” spin system, we also use the unitary transformation $H_{diag} = V^{-1}HV$ for diagonalization the Hamiltonian, where “ V ” is the unitary matrix of eigenvectors (columns):

$$V = \begin{bmatrix} 0 & 0 & 0 & 0 & 0 & 0 & 0 & 1 \\ 0 & 0 & 0 & 0 & 0 & 1 & 0 & 0 \\ 0 & 0 & -\sin \theta^+ & 0 & \cos \theta^+ & 0 & 0 & 0 \\ -\sin \theta^- & 0 & 0 & 0 & 0 & 0 & \cos \theta^- & 0 \\ 0 & 0 & \cos \theta^+ & 0 & \sin \theta^+ & 0 & 0 & 0 \\ \cos \theta^- & 0 & 0 & 0 & 0 & 0 & \sin \theta^- & 0 \\ 0 & 1 & 0 & 0 & 0 & 0 & 0 & 0 \\ 0 & 0 & 0 & 1 & 0 & 0 & 0 & 0 \end{bmatrix}. \quad (4.36)$$

The Hamiltonian in its diagonal form is therefore given by:

$$H_{diag} = \begin{bmatrix} B_1 & 0 & 0 & 0 & 0 & 0 & 0 & 0 \\ 0 & B_2 & 0 & 0 & 0 & 0 & 0 & 0 \\ 0 & 0 & B_3 & 0 & 0 & 0 & 0 & 0 \\ 0 & 0 & 0 & B_4 & 0 & 0 & 0 & 0 \\ 0 & 0 & 0 & 0 & B_5 & 0 & 0 & 0 \\ 0 & 0 & 0 & 0 & 0 & B_6 & 0 & 0 \\ 0 & 0 & 0 & 0 & 0 & 0 & B_7 & 0 \\ 0 & 0 & 0 & 0 & 0 & 0 & 0 & B_8 \end{bmatrix}, \quad (4.37)$$

where

$$B_1 = -\frac{\omega_3}{2} - \frac{\pi J_{12}}{2} - \frac{M^-}{2},$$

$$B_2 = \frac{(-\omega_1 - \omega_2 + \omega_3)}{2} + \frac{\pi J_{12} - \pi J_{13} - \pi J_{23}}{2},$$

$$B_3 = \frac{\omega_3}{2} - \frac{\pi J_{12}}{2} - \frac{M^+}{2},$$

$$B_4 = \frac{(-\omega_1 - \omega_2 - \omega_3)}{2} + \frac{\pi J_{12} + \pi J_{13} + \pi J_{23}}{2},$$

$$B_5 = \frac{\omega_3}{2} - \frac{\pi J_{12}}{2} + \frac{M^+}{2},$$

$$B_6 = \frac{(\omega_1 + \omega_2 - \omega_3)}{2} + \frac{\pi J_{12} - \pi J_{13} - \pi J_{23}}{2},$$

$$B_7 = -\frac{\omega_3}{2} - \frac{\pi J_{12}}{2} + \frac{M^-}{2},$$

$$B_8 = \frac{(\omega_1 + \omega_2 + \omega_3)}{2} + \frac{\pi J_{12} + \pi J_{13} + \pi J_{23}}{2},$$

and

$$M^\pm = \sqrt{4(\pi J_{12})^2 + ((\omega_1 - \omega_2) \pm \pi(J_{13} - J_{23}))^2}.$$

According to the selection rules, there are 14 allowed transitions. The first 12 out of 14 transitions are first order transitions and the last two transitions are multiple quantum transitions, in which all three spins flip; they are called combination lines. Therefore an “ABX” spectrum consists of 14 lines. The combination lines (lines 14 and 15) become large when $J_{AB} > (\omega_A - \omega_B)$ and these are the “X” lines. So the “AB” part of “ABX” spectrum contains 8 lines that consists of two separate quartets and the “X” part of “ABX” spectrum contains 6 lines. The allowed transitions with the transition energies and relative intensities are given in Table (4.6).

Transition	Energy	Relative intensity
1)8 → 6	$\bar{\omega} + \frac{\pi}{2}(-2J_{12} - J_{13} - J_{23}) - \frac{M^-}{2}$	$1 - \sin(2\theta^+)$
2)5 → 2	$\bar{\omega} + \frac{\pi}{2}(2J_{12} - J_{13} - J_{23}) - \frac{M^-}{2}$	$1 + \sin(2\theta^-)$
3)7 → 4	$\bar{\omega} + \frac{\pi}{2}(-2J_{12} + J_{13} + J_{23}) - \frac{M^+}{2}$	$1 - \sin(2\theta^-)$
4)3 → 1	$\bar{\omega} + \frac{\pi}{2}(2J_{12} + J_{13} + J_{23}) - \frac{M^+}{2}$	$1 + \sin(2\theta^+)$
5)8 → 5	$\bar{\omega} + \frac{\pi}{2}(-2J_{12} - J_{13} - J_{23}) + \frac{M^-}{2}$	$1 + \sin(2\theta^-)$
6)7 → 3	$\bar{\omega} + \frac{\pi}{2}(-2J_{12} + J_{13} + J_{23}) + \frac{M^+}{2}$	$1 + \sin(2\theta^+)$
7)6 → 2	$\bar{\omega} + \frac{\pi}{2}(2J_{12} - J_{13} - J_{23}) + \frac{M^-}{2}$	$1 - \sin(2\theta^-)$
8)4 → 1	$\bar{\omega} + \frac{\pi}{2}(2J_{12} + J_{13} + J_{23}) + \frac{M^+}{2}$	$1 - \sin(2\theta^+)$
9)8 → 7	$\omega_3 - \pi(J_{13} + J_{23})$	1
10)5 → 3	$\omega_3 + \frac{(M^+ - M^-)}{2}$	$\cos^2(\theta^+ - \theta^-)$
11)6 → 4	$\omega_3 + \frac{(-M^+ + M^-)}{2}$	$\cos^2(\theta^+ - \theta^-)$
12)2 → 1	$\omega_3 + \pi(J_{13} + J_{23})$	1
13)7 → 2	Forbidden Transition	0
14)5 → 4	$\omega_3 - \frac{(M^+ + M^-)}{2}$	$\sin^2(\theta^+ - \theta^-)$
15)6 → 3	$\omega_3 + \frac{(M^+ + M^-)}{2}$	$\sin^2(\theta^+ - \theta^-)$

Tab. 4.6: Transition Energies and Intensities for three nuclei “ABX”, where $\bar{\omega} = \frac{(\omega_1 + \omega_2)}{2}$ and $\theta^\pm = \frac{1}{2} \tan^{-1} \frac{2\pi J_{12}}{\omega_1 - \omega_2 \pm \pi(J_{13} - J_{23})}$.

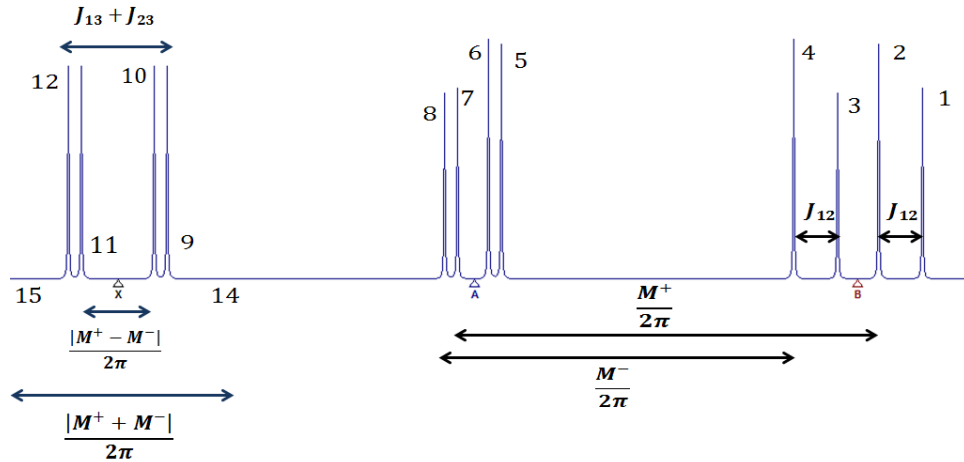


Fig. 4.4: Typical spectrum for three nuclei “ABX”. The lines 1, 2, 3, 4 are “B” lines; 5, 6, 7, 8 are “A” lines and 9, 10, 11, 12, 14, 15 are “X” lines. The numbering of lines applies if $\omega_A > \omega_B$ and $J_{23} > J_{13}$. The numbers in the figure are related to the transitions indicated in Table (4.6).

First, the “AB” part of the “ABX” spin system is considered. To derive the “AB” part of the spectrum we analytically calculate the signal (4.7) for the I_1^+ and I_2^+ terms in an “ABX” spin system. By substituting Eqs. (4.36) and (4.37) into (4.12), we find that the signal due to spins 1 and 2 can be written as:

$$S_{p,1,2}(t) = \frac{1}{8}(\overline{\mathbf{1}}, \overline{\mathbf{2}}, \overline{\mathbf{3}}, \overline{\mathbf{4}}, \overline{\mathbf{5}}, \overline{\mathbf{6}}, \overline{\mathbf{7}}, \overline{\mathbf{8}}) \times$$

$$\begin{pmatrix}
 D_1 & -D_1 & -D_1 & D_1 & D_7 & -D_7 & -D_7 & D_7 \\
 D_2 & D_2 & -D_2 & -D_2 & D_5 & D_5 & -D_5 & -D_5 \\
 D_3 & -D_3 & D_3 & -D_3 & D_8 & -D_8 & D_8 & -D_8 \\
 D_4 & D_4 & D_4 & D_4 & D_6 & D_6 & D_6 & D_6 \\
 D_5 & -D_5 & -D_5 & D_5 & D_2 & -D_2 & -D_2 & D_2 \\
 D_6 & -D_6 & D_6 & -D_6 & D_4 & -D_4 & D_4 & -D_4 \\
 D_7 & D_7 & -D_7 & -D_7 & D_1 & D_1 & -D_1 & -D_1 \\
 D_8 & D_8 & D_8 & D_8 & D_3 & D_3 & D_3 & D_3
 \end{pmatrix}$$

$$\times \begin{pmatrix}
 Tr\{\rho_0 \tilde{I}_{1+}\} \\
 Tr\{\rho_0 2\tilde{I}_{1+} \tilde{I}_{2z}\} \\
 Tr\{\rho_0 2\tilde{I}_{1+} \tilde{I}_{3z}\} \\
 Tr\{\rho_0 4\tilde{I}_{1+} \tilde{I}_{2z} \tilde{I}_{3z}\} \\
 Tr\{\rho_0 \tilde{I}_{2+}\} \\
 Tr\{\rho_0 2\tilde{I}_{1z} \tilde{I}_{2+}\} \\
 Tr\{\rho_0 2\tilde{I}_{2+} \tilde{I}_{3z}\} \\
 Tr\{\rho_0 4\tilde{I}_{1z} \tilde{I}_{2+} \tilde{I}_{3z}\}
 \end{pmatrix}, \quad (4.38)$$

where

$$\overline{\mathbf{1}} = \frac{(\omega_1 + \omega_2)}{2} - \frac{M^-}{2} - \frac{\pi(J_{13} + J_{23})}{2} - \pi J_{12},$$

$$\overline{\mathbf{2}} = \frac{(\omega_1 + \omega_2)}{2} - \frac{M^-}{2} - \frac{\pi(J_{13} + J_{23})}{2} + \pi J_{12},$$

$$\overline{\mathbf{3}} = \frac{(\omega_1 + \omega_2)}{2} - \frac{M^+}{2} + \frac{\pi(J_{13} + J_{23})}{2} - \pi J_{12},$$

$$\overline{\mathbf{4}} = \frac{(\omega_1 + \omega_2)}{2} - \frac{M^+}{2} + \frac{\pi(J_{13} + J_{23})}{2} + \pi J_{12},$$

$$\overline{\mathbf{5}} = \frac{(\omega_1 + \omega_2)}{2} + \frac{M^-}{2} - \frac{\pi(J_{13} + J_{23})}{2} - \pi J_{12},$$

$$\overline{\mathbf{6}} = \frac{(\omega_1 + \omega_2)}{2} + \frac{M^+}{2} + \frac{\pi(J_{13} + J_{23})}{2} - \pi J_{12},$$

$$\overline{\mathbf{7}} = \frac{(\omega_1 + \omega_2)}{2} + \frac{M^-}{2} - \frac{\pi(J_{13} + J_{23})}{2} + \pi J_{12},$$

$$\overline{\mathbf{8}} = \frac{(\omega_1 + \omega_2)}{2} + \frac{M^+}{2} + \frac{\pi(J_{13} + J_{23})}{2} + \pi J_{12},$$

and

$$D_1 = (2 \sin^2(\theta^-) - \sin(2\theta^-)), \quad D_2 = (2 \sin^2(\theta^-) + \sin(2\theta^-)),$$

$$D_3 = (2 \sin^2(\theta^+) - \sin(2\theta^+)), \quad D_4 = (2 \sin^2(\theta^+) + \sin(2\theta^+)),$$

$$D_5 = (2 \cos^2(\theta^-) + \sin(2\theta^-)), \quad D_6 = (2 \cos^2(\theta^+) + \sin(2\theta^+)),$$

$$D_7 = (2 \cos^2(\theta^-) - \sin(2\theta^-)), \quad D_8 = (2 \cos^2(\theta^+) - \sin(2\theta^+)).$$

Here, $\tilde{A} = U_p^{-1} A U_p$ is also the operator A transformed by the unitary operator U_p^{-1} due to the applied preparatory pulses. Taking the Fourier transform of Eq. (4.38) at the eight observed frequencies, we find that:

$$\begin{aligned}
 & \begin{pmatrix} \bar{S}_{p,1,2}(\frac{\omega_1+\omega_2}{2} - \frac{M^-}{2} - \frac{\pi(J_{13}+J_{23})}{2} - \pi J_{12}) \\ \bar{S}_{p,1,2}(\frac{\omega_1+\omega_2}{2} - \frac{M^-}{2} - \frac{\pi(J_{13}+J_{23})}{2} + \pi J_{12}) \\ \bar{S}_{p,1,2}(\frac{\omega_1+\omega_2}{2} - \frac{M^+}{2} + \frac{\pi(J_{13}+J_{23})}{2} - \pi J_{12}) \\ \bar{S}_{p,1,2}(\frac{\omega_1+\omega_2}{2} - \frac{M^+}{2} + \frac{\pi(J_{13}+J_{23})}{2} + \pi J_{12}) \\ \bar{S}_{p,1,2}(\frac{\omega_1+\omega_2}{2} + \frac{M^-}{2} - \frac{\pi(J_{13}+J_{23})}{2} - \pi J_{12}) \\ \bar{S}_{p,1,2}(\frac{\omega_1+\omega_2}{2} + \frac{M^+}{2} + \frac{\pi(J_{13}+J_{23})}{2} - \pi J_{12}) \\ \bar{S}_{p,1,2}(\frac{\omega_1+\omega_2}{2} + \frac{M^-}{2} - \frac{\pi(J_{13}+J_{23})}{2} + \pi J_{12}) \\ \bar{S}_{p,1,2}(\frac{\omega_1+\omega_2}{2} + \frac{M^+}{2} + \frac{\pi(J_{13}+J_{23})}{2} + \pi J_{12}) \end{pmatrix} \\
 &= \frac{1}{8} \begin{pmatrix} D_1 & -D_1 & -D_1 & D_1 & D_7 & -D_7 & -D_7 & D_7 \\ D_2 & D_2 & -D_2 & -D_2 & D_5 & D_5 & -D_5 & -D_5 \\ D_3 & -D_3 & D_3 & -D_3 & D_8 & -D_8 & D_8 & -D_8 \\ D_4 & D_4 & D_4 & D_4 & D_6 & D_6 & D_6 & D_6 \\ D_5 & -D_5 & -D_5 & D_5 & D_2 & -D_2 & -D_2 & D_2 \\ D_6 & -D_6 & D_6 & -D_6 & D_4 & -D_4 & D_4 & -D_4 \\ D_7 & D_7 & -D_7 & -D_7 & D_1 & D_1 & -D_1 & -D_1 \\ D_8 & D_8 & D_8 & D_8 & D_3 & D_3 & D_3 & D_3 \end{pmatrix} \\
 & \quad \times \begin{pmatrix} Tr\{\rho_0 \tilde{I}_{1+}\} \\ Tr\{\rho_0 2\tilde{I}_{1+} \tilde{I}_{2z}\} \\ Tr\{\rho_0 2\tilde{I}_{1+} \tilde{I}_{3z}\} \\ Tr\{\rho_0 4\tilde{I}_{1+} \tilde{I}_{2z} \tilde{I}_{3z}\} \\ Tr\{\rho_0 \tilde{I}_{2+}\} \\ Tr\{\rho_0 2\tilde{I}_{1z} \tilde{I}_{2+}\} \\ Tr\{\rho_0 2\tilde{I}_{2+} \tilde{I}_{3z}\} \\ Tr\{\rho_0 4\tilde{I}_{1z} \tilde{I}_{2+} \tilde{I}_{3z}\} \end{pmatrix}. \tag{4.39}
 \end{aligned}$$

We invert Eq. (4.39) and construct the expectation values directly in terms of linear

combinations of fitted data:

$$\begin{aligned}
 & 2^{1-n} \begin{pmatrix} -A & B & -C & D & E & F & G & K \\ A & B & C & D & -E & -F & G & K \\ A & -B & -C & D & -E & F & -G & K \\ -A & -B & C & D & E & -F & -G & K \\ G & E & K & F & B & D & -A & -C \\ -G & E & -K & F & -B & -D & -A & -C \\ -G & -E & K & F & -B & D & A & -C \\ G & -E & -K & F & B & -D & A & -C \end{pmatrix} \times \\
 & \begin{pmatrix} \bar{S}_{p,1,2}(\frac{\omega_1+\omega_2}{2} - \frac{M^-}{2} - \frac{\pi(J_{13}+J_{23})}{2} - \pi J_{12}) \\ \bar{S}_{p,1,2}(\frac{\omega_1+\omega_2}{2} - \frac{M^-}{2} - \frac{\pi(J_{13}+J_{23})}{2} + \pi J_{12}) \\ \bar{S}_{p,1,2}(\frac{\omega_1+\omega_2}{2} - \frac{M^+}{2} + \frac{\pi(J_{13}+J_{23})}{2} - \pi J_{12}) \\ \bar{S}_{p,1,2}(\frac{\omega_1+\omega_2}{2} - \frac{M^+}{2} + \frac{\pi(J_{13}+J_{23})}{2} + \pi J_{12}) \\ \bar{S}_{p,1,2}(\frac{\omega_1+\omega_2}{2} + \frac{M^-}{2} - \frac{\pi(J_{13}+J_{23})}{2} - \pi J_{12}) \\ \bar{S}_{p,1,2}(\frac{\omega_1+\omega_2}{2} + \frac{M^+}{2} + \frac{\pi(J_{13}+J_{23})}{2} - \pi J_{12}) \\ \bar{S}_{p,1,2}(\frac{\omega_1+\omega_2}{2} + \frac{M^-}{2} - \frac{\pi(J_{13}+J_{23})}{2} + \pi J_{12}) \\ \bar{S}_{p,1,2}(\frac{\omega_1+\omega_2}{2} + \frac{M^+}{2} + \frac{\pi(J_{13}+J_{23})}{2} + \pi J_{12}) \end{pmatrix} \\
 & = \frac{1}{2^n} \times \begin{pmatrix} Tr\{\rho_0 2\tilde{I}_{1+}\} \\ Tr\{\rho_0 4\tilde{I}_{1+}\tilde{I}_{2z}\} \\ Tr\{\rho_0 4\tilde{I}_{1+}\tilde{I}_{3z}\} \\ Tr\{\rho_0 8\tilde{I}_{1+}\tilde{I}_{2z}\tilde{I}_{3z}\} \\ Tr\{\rho_0 2\tilde{I}_{2+}\} \\ Tr\{\rho_0 4\tilde{I}_{1z}\tilde{I}_{2+}\} \\ Tr\{\rho_0 4\tilde{I}_{2+}\tilde{I}_{3z}\} \\ Tr\{\rho_0 8\tilde{I}_{1z}\tilde{I}_{2+}\tilde{I}_{3z}\} \end{pmatrix}, \tag{4.40}
 \end{aligned}$$

where

$$\begin{aligned}
 A &= \frac{\sin \theta^-}{\cos \theta^- - \sin \theta^-}, & B &= \frac{\sin \theta^-}{\cos \theta^- + \sin \theta^-}, & C &= \frac{\sin \theta^+}{\cos \theta^+ - \sin \theta^+}, & D &= \frac{\sin \theta^+}{\cos \theta^+ + \sin \theta^+}, \\
 E &= \frac{\cos \theta^-}{\cos \theta^- + \sin \theta^-}, & F &= \frac{\cos \theta^+}{\cos \theta^+ + \sin \theta^+}, & G &= \frac{\cos \theta^-}{\cos \theta^- - \sin \theta^-}, & K &= \frac{\cos \theta^+}{\cos \theta^+ - \sin \theta^+} \text{ and } n = 3.
 \end{aligned}$$

Now, let us consider the ‘‘X’’ part of the ‘‘ABX’’ spin system. The ‘‘X’’ part of

the spectrum contains 6 lines corresponding to 4 first order and 2 multiple quantum transitions. When $2\pi|J_{12}| < |\omega_1 - \omega_2|$ the intensities of the multiple quantum transitions become small and may not be observed in some cases. We consider I_{3+} term in an “ ABX ” spin system (the “ X ” part of the “ ABX ” spin system) and by substituting Eqs. (4.36) and (4.37) into (4.12), we find that the signal due to spin 3 can be written as:

$$\begin{aligned}
 S_{p,3}(t) = & \frac{1}{4}(\bar{\mathbf{1}}, \bar{\mathbf{2}}, \bar{\mathbf{3}}, \bar{\mathbf{4}}, \bar{\mathbf{5}}, \bar{\mathbf{6}}) \times \\
 & \begin{pmatrix} E_1 & -E_3 & E_3 & -E_1 & E_5 & -E_8 \\ 1 & -1 & -1 & 1 & 0 & 0 \\ E_2 & E_4 & -E_4 & -E_2 & E_6 & E_7 \\ E_2 & -E_4 & E_4 & -E_2 & -E_7 & -E_6 \\ 1 & 1 & 1 & 1 & 0 & 0 \\ E_1 & E_3 & -E_3 & -E_1 & E_8 & -E_5 \end{pmatrix} \\
 & \times \begin{pmatrix} Tr\{\rho_0 \tilde{I}_{3+}\} \\ Tr\{\rho_0 2\tilde{I}_{1z}\tilde{I}_{3+}\} \\ Tr\{\rho_0 2\tilde{I}_{2z}\tilde{I}_{3+}\} \\ Tr\{\rho_0 4\tilde{I}_{1z}\tilde{I}_{2z}\tilde{I}_{3+}\} \\ Tr\{\rho_0 4\tilde{I}_{1-}\tilde{I}_{2+}\tilde{I}_{3+}\} \\ Tr\{\rho_0 4\tilde{I}_{1+}\tilde{I}_{2-}\tilde{I}_{3+}\} \end{pmatrix}, \tag{4.41}
 \end{aligned}$$

where

$$\bar{\mathbf{1}} = \omega_3 + \frac{-M^+ - M^-}{2},$$

$$\bar{\mathbf{2}} = \omega_3 - \pi(J_{13} + J_{23}),$$

$$\bar{\mathbf{3}} = \omega_3 + \frac{M^+ - M^-}{2},$$

$$\bar{\mathbf{4}} = \omega_3 + \frac{-M^+ + M^-}{2},$$

$$\bar{\mathbf{5}} = \omega_3 + \pi(J_{13} + J_{23}),$$

$$\bar{\mathbf{6}} = \omega_3 + \frac{M^+ + M^-}{2},$$

and

$$E_1 = \sin^2(\theta^- - \theta^+),$$

$$E_2 = \cos^2(\theta^- - \theta^+),$$

$$E_3 = \sin(\theta^- - \theta^+) \sin(\theta^- + \theta^+),$$

$$\begin{aligned}
 E_4 &= \cos(\theta^- - \theta^+) \cos(\theta^- + \theta^+), \\
 E_5 &= \cos(\theta^-) \cos(\theta^+) \sin(\theta^- - \theta^+), \\
 E_6 &= \cos(\theta^-) \sin(\theta^+) \cos(\theta^- - \theta^+), \\
 E_7 &= \sin(\theta^-) \cos(\theta^+) \cos(\theta^- - \theta^+), \\
 E_8 &= \sin(\theta^-) \sin(\theta^+) \sin(\theta^- - \theta^+).
 \end{aligned}$$

Taking the Fourier transform of Eq. (4.41) at the six observed frequencies, we find that:

$$\begin{aligned}
 & \begin{pmatrix} \bar{S}_{p,3}(\omega_3 + \frac{-M^+ - M^-}{2}) \\ \bar{S}_{p,3}(\omega_3 - \pi(J_{13} + J_{23})) \\ \bar{S}_{p,3}(\omega_3 + \frac{M^+ - M^-}{2}) \\ \bar{S}_{p,3}(\omega_3 + \frac{-M^+ + M^-}{2}) \\ \bar{S}_{p,3}(\omega_3 + \pi(J_{13} + J_{23})) \\ \bar{S}_{p,3}(\omega_3 + \frac{M^+ + M^-}{2}) \end{pmatrix} \\
 &= \frac{1}{4} \begin{pmatrix} E_1 & -E_3 & E_3 & -E_1 & E_5 & -E_8 \\ 1 & -1 & -1 & 1 & 0 & 0 \\ E_2 & E_4 & -E_4 & -E_2 & E_6 & E_7 \\ E_2 & -E_4 & E_4 & -E_2 & -E_7 & -E_6 \\ 1 & 1 & 1 & 1 & 0 & 0 \\ E_1 & E_3 & -E_3 & -E_1 & E_8 & -E_5 \end{pmatrix} \\
 & \times \begin{pmatrix} Tr\{\rho_0 \tilde{I}_{3+}\} \\ Tr\{\rho_0 2\tilde{I}_{1z} \tilde{I}_{3+}\} \\ Tr\{\rho_0 2\tilde{I}_{2z} \tilde{I}_{3+}\} \\ Tr\{\rho_0 4\tilde{I}_{1z} \tilde{I}_{2z} \tilde{I}_{3+}\} \\ Tr\{\rho_0 4\tilde{I}_{1-} \tilde{I}_{2+} \tilde{I}_{3+}\} \\ Tr\{\rho_0 4\tilde{I}_{1+} \tilde{I}_{2-} \tilde{I}_{3+}\} \end{pmatrix}. \tag{4.42}
 \end{aligned}$$

We invert Eq. (4.42) and construct the expectation values directly in terms of linear combinations of fitted data. Therefore, the relation between the Fourier intensities and

product basis coefficients at the six observed frequencies is given by:

$$\begin{aligned}
 & 2^{1-n} \begin{pmatrix} 1 & 1 & 1 & 1 & 1 & 1 \\ -S & -1 & P & -P & 1 & S \\ S & -1 & -P & P & 1 & -S \\ -1 & 1 & -1 & -1 & 1 & -1 \\ Q & 0 & -Y & -R & 0 & M \\ -M & 0 & R & Y & 0 & -Q \end{pmatrix} \times \\
 & \begin{pmatrix} \bar{S}_{p,3}(\omega_3 + \frac{-M^+ - M^-}{2}) \\ \bar{S}_{p,3}(\omega_3 - \pi(J_{13} + J_{23})) \\ \bar{S}_{p,3}(\omega_3 + \frac{M^+ - M^-}{2}) \\ \bar{S}_{p,3}(\omega_3 + \frac{-M^+ + M^-}{2}) \\ \bar{S}_{p,3}(\omega_3 + \pi(J_{13} + J_{23})) \\ \bar{S}_{p,3}(\omega_3 + \frac{M^+ + M^-}{2}) \end{pmatrix} \\
 & = \frac{1}{2^n} \times \begin{pmatrix} Tr\{\rho_0 2\tilde{I}_{3+}\} \\ Tr\{\rho_0 4\tilde{I}_{1z}\tilde{I}_{3+}\} \\ Tr\{\rho_0 4\tilde{I}_{2z}\tilde{I}_{3+}\} \\ Tr\{\rho_0 8\tilde{I}_{1z}\tilde{I}_{2z}\tilde{I}_{3+}\} \\ Tr\{\rho_0 8\tilde{I}_{1-}\tilde{I}_{2+}\tilde{I}_{3+}\} \\ Tr\{\rho_0 8\tilde{I}_{1+}\tilde{I}_{2-}\tilde{I}_{3+}\} \end{pmatrix}, \tag{4.43}
 \end{aligned}$$

where

$$\begin{aligned}
 S &= \frac{\sin(\theta^- + \theta^+)}{\sin(\theta^- - \theta^+)}, \quad P = \frac{\cos(\theta^- + \theta^+)}{\cos(\theta^- - \theta^+)}, \\
 Q &= \frac{(2 \cos(\theta^- - \theta^+) + 2 \cos(\theta^- + \theta^+))}{\sin(\theta^- - \theta^+)}, \\
 Y &= \frac{(2 \sin(\theta^- - \theta^+) - 2 \sin(\theta^- + \theta^+))}{\cos(\theta^- - \theta^+)}, \\
 R &= \frac{(2 \sin(\theta^- - \theta^+) + 2 \sin(\theta^- + \theta^+))}{\cos(\theta^- - \theta^+)}, \\
 M &= \frac{(2 \cos(\theta^- - \theta^+) - 2 \cos(\theta^- + \theta^+))}{\sin(\theta^- - \theta^+)} \text{ and } n = 3.
 \end{aligned}$$

The multiple quantum transitions, which are not present in weakly coupled systems, add further information to a single spectrum. This feature allows one to reduce the number of experiments needed to complete the tomography of the density matrix.

Thus, using Eq. (4.33) in “ AB ” spin system and Eqs. (4.40) and (4.43) in “ ABX ” spin system, the density matrix can be reconstructed for “ AB ” and “ ABX ” spin systems. To prove the accuracy of the results obtained in this section and the previous section, several experiments have been performed on the “ AB ” and “ ABX ” spin systems which are described fully in the next chapter.

5

Experimental Benchmarks

Result II:

We report in this chapter two experimental benchmarks on a three-qubit liquid state nuclear magnetic resonance quantum information processor aimed at testing the technique developed in the previous chapter. In both cases, full quantum state tomography was performed at the different steps. In the first case, i.e. for “ AB ” spin system, the density matrix is reconstructed in two steps $|11\rangle$ and $|10\rangle$ while in the second case, i.e. for the “ ABX ” spin system, the density matrix is reconstructed in each step of the quantum teleportation protocol.

SECTION: 5.1

“ AB ” Spin System

As we have obtained in the previous chapter, the NMR signal due to spins “ AB ” can be written in the form (see Eq. (4.33)):

$$\begin{aligned}
 & 2^{1-n} \begin{pmatrix} -A & B & C & D \\ A & B & -C & D \\ D & C & B & -A \\ -D & C & -B & -A \end{pmatrix} \begin{pmatrix} \bar{S}_{p,1,2}(\frac{\omega_1+\omega_2}{2} - \frac{M}{2} - \pi J_{12}) \\ \bar{S}_{p,1,2}(\frac{\omega_1+\omega_2}{2} - \frac{M}{2} + \pi J_{12}) \\ \bar{S}_{p,1,2}(\frac{\omega_1+\omega_2}{2} + \frac{M}{2} - \pi J_{12}) \\ \bar{S}_{p,1,2}(\frac{\omega_1+\omega_2}{2} + \frac{M}{2} + \pi J_{12}) \end{pmatrix} \\
 &= \frac{1}{2^n} \times \begin{pmatrix} Tr\{\rho_0 2\tilde{I}_{1+}\} \\ Tr\{\rho_0 4\tilde{I}_{1+}\tilde{I}_{2z}\} \\ Tr\{\rho_0 2\tilde{I}_{2+}\} \\ Tr\{\rho_0 4\tilde{I}_{1z}\tilde{I}_{2+}\} \end{pmatrix}, \tag{5.1}
 \end{aligned}$$

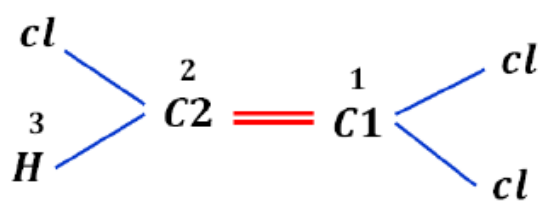
where $A = \frac{\sin \theta}{\cos \theta - \sin \theta}$, $B = \frac{\sin \theta}{\cos \theta + \sin \theta}$, $C = \frac{\cos \theta}{\cos \theta + \sin \theta}$, $D = \frac{\cos \theta}{\cos \theta - \sin \theta}$ and $n = 2$.

Since the coefficients involved in Eq. (5.1) are the same as in the weak coupling case, we can use the minimal set of preparatory pulses shown in Table (5.1) to perform a complete state tomography of “ AB ” systems.

Pulse set
$XX, 11, 1X, 1Y$

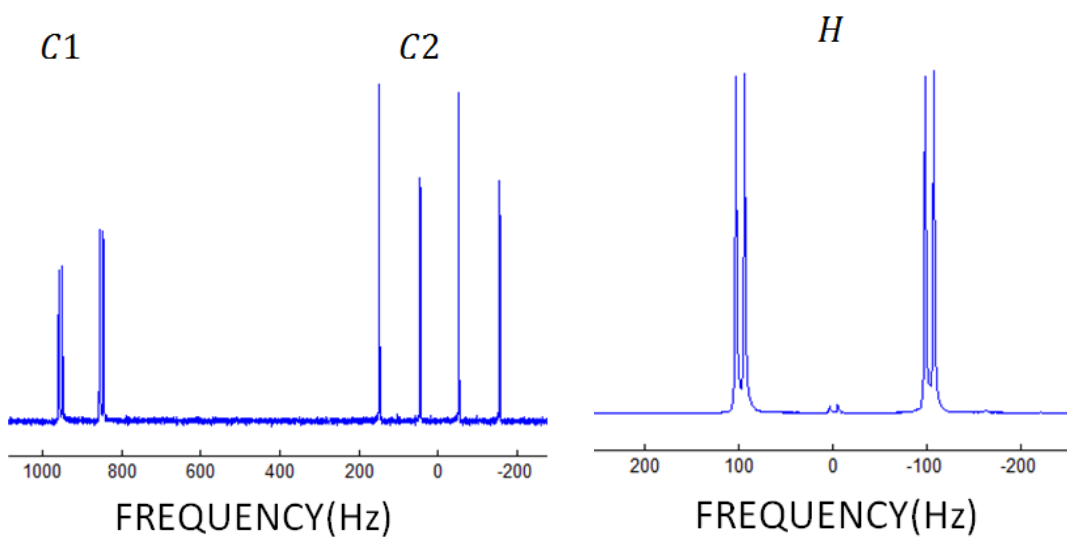
Tab. 5.1: The pulse set, together, yield the complete tomography of two-spin homonuclear system. The pulse set labeled $1X$ applied to the two-spin system, for example, specifies no pulse on spin 1, and an X pulse on spin 2.

To prove Eq. (5.1), we have reconstructed the density matrices of two strongly coupled qubits for the state $|11\rangle$ and the subsequent application of the Controlled-NOT (CNOT) gate. The experimental density matrices of two strongly coupled qubits for these two states are shown in Fig. (5.3). This demonstration was carried out on a liquid-state NMR quantum information processor, using a sample of trichloroethylene dissolved in deuterated chloroform (Fig. (5.1)). In this sample, the chemical shift difference between two carbons is comparable to their coupling to each other, and both are coupled to a Hydrogen with Larmor frequency far away from the ones of the two carbons. The coupling constants are $J_{12} = 103.1Hz$, $J_{13} = 8.59Hz$, and $J_{23} = 201.31Hz$ and the difference between the C_1 and C_2 Larmor frequencies is $\Delta\nu_{12} = 899.67Hz$. The phase decoherence times (T_2) for C_1 and C_2 and Hydrogen are approximately 0.4s and 0.6s and 4s, respectively. The spin system is actually an “ ABX ” system. However, when the proton spin is decoupled from the two carbons, the system becomes an “ AB ” system (this is what we have used in this section). The molecule structure and NMR spectra of the thermal equilibrium state are shown in Figs. (5.1) and (5.2).



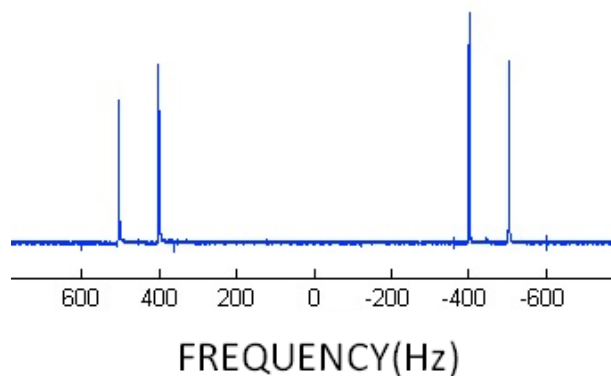
(Hz)	C1	C2	H
C1	15553.1	103.1	8.59
C2	103.1	3234.5	201.3
H	8.59	201.3	14653.4

Fig. 5.1: The structure and the parameters of carbon and proton labeled trichloroethylene (TCE) molecule. The diagonal terms in the table are the chemical shifts (in Hz) of the carbons and proton. The nondiagonal terms are the coupling constants, also in Hz. The numbers above the carbons and proton specify the number of qubits.



(a)

(b)



(c)

Fig. 5.2: Thermal equilibrium spectra of trichloroethylene (a) Carbon spectrum when the proton is not decoupled, (b) proton spectrum and (c) carbon spectrum when proton is decoupled, obtained by applying selective readout pulses to the system in its thermal equilibrium state.

All quantum operations were implemented using Gradient Ascent Pulse Engineering (GRAPE) method (see chapter (3)). The total duration of each pulse used in our experiment was between $1ms$ to $2ms$. Table (5.2) show the control parameters for each GRAPE pulse used in this experiment.

Pulse	Time step	Total time	$\frac{1}{2J}$	Fidelity
$R_x^1(\frac{\pi}{2})$	$1 \mu s$	$1000 \mu s$	-	0.9999
$R_x^2(\frac{\pi}{2})$	$1.5 \mu s$	$1500 \mu s$	-	1
Hadamard for first qubit	$1 \mu s$	$1000 \mu s$	-	0.9999
Hadamard for second qubit	$1.5 \mu s$	$1500 \mu s$	-	1
$CNOT_{12}$	$2 \mu s$	$4000 \mu s$	$2.5 ms$	0.9999
$CNOT_{23}$	$3 \mu s$	$6000 \mu s$	$4.9 ms$	0.9999

Tab. 5.2: Control parameters input into the GRAPE algorithm for trichloroethylene molecule (see Chapter (3)).

To measure the efficacy with which the experiment was carried out, we calculated the fidelity, i.e.

$$F = \frac{\text{tr}(\rho_{exp}\rho_{theory}^\dagger)}{\sqrt{\text{tr}(\rho_{exp}^2)\text{tr}(\rho_{theory}^2)}}, \quad (5.2)$$

where ρ_{exp} and ρ_{theory} are experimental and theoretical density matrices, respectively. Using this formula, the fidelities of the state $|11\rangle$ and the subsequent application of the $CNOT$ gate, with the first qubit ($C1$) as the control and the second qubit ($C2$) as the target, were found to be over 0.99. The result demonstrates that satisfactory accuracy in the density matrix reconstruction can be achieved with this method.

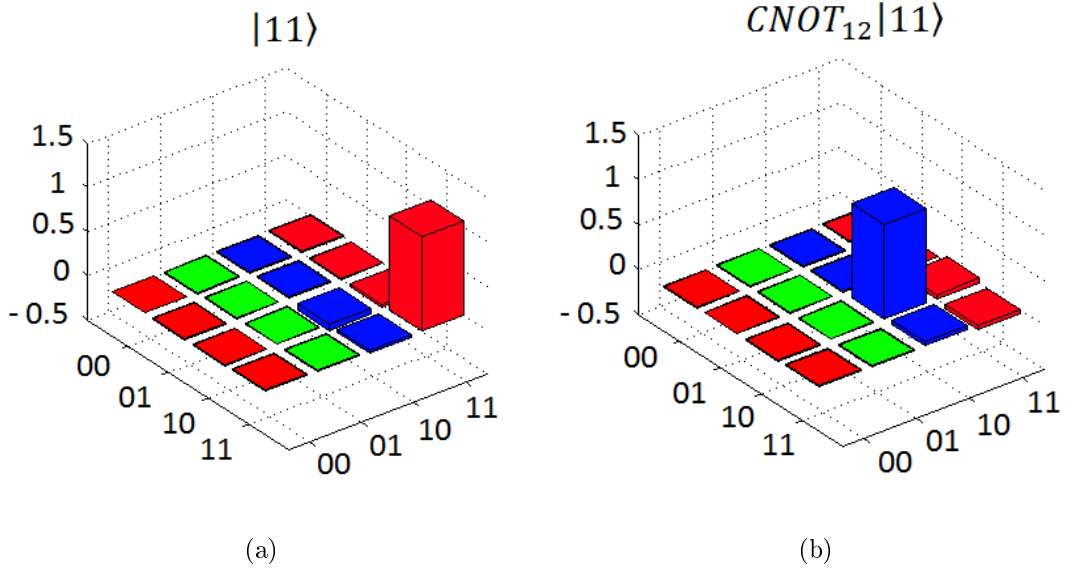


Fig. 5.3: Real parts of the reconstructed density matrices for an “ AB ” system. (a) State $|11\rangle$ and (b) after the application of the $CNOT$ gate over the state $|11\rangle$, resulting in the state $|10\rangle$, where $CNOT_{ij}$ denotes a Controlled-NOT gate with the qubit i as control and the qubit j as target. The fidelity was over 0.99 in both cases. The rows and columns represent the standard computational basis in binary order, with $|00\rangle$ starting from the leftmost column and $|11\rangle$ being the rightmost column.

SECTION: 5.2

“ ABX ” Spin System

As we obtained in the previous chapter, the signal due to spins “ AB ” and “ X ” in the “ ABX ” spin system can be written in the form of the following equations, respectively (see Eqs. (4.40) and (4.43)):

$$\begin{aligned}
& 2^{1-n} \begin{pmatrix} -A & B & -C & D & E & F & G & K \\ A & B & C & D & -E & -F & G & K \\ A & -B & -C & D & -E & F & -G & K \\ -A & -B & C & D & E & -F & -G & K \\ G & E & K & F & B & D & -A & -C \\ -G & E & -K & F & -B & -D & -A & -C \\ -G & -E & K & F & -B & D & A & -C \\ G & -E & -K & F & B & -D & A & -C \end{pmatrix} \times \\
& \begin{pmatrix} \bar{S}_{p,1,2}(\frac{\omega_1+\omega_2}{2} - \frac{M^-}{2} - \frac{\pi(J_{13}+J_{23})}{2} - \pi J_{12}) \\ \bar{S}_{p,1,2}(\frac{\omega_1+\omega_2}{2} - \frac{M^-}{2} - \frac{\pi(J_{13}+J_{23})}{2} + \pi J_{12}) \\ \bar{S}_{p,1,2}(\frac{\omega_1+\omega_2}{2} - \frac{M^+}{2} + \frac{\pi(J_{13}+J_{23})}{2} - \pi J_{12}) \\ \bar{S}_{p,1,2}(\frac{\omega_1+\omega_2}{2} - \frac{M^+}{2} + \frac{\pi(J_{13}+J_{23})}{2} + \pi J_{12}) \\ \bar{S}_{p,1,2}(\frac{\omega_1+\omega_2}{2} + \frac{M^-}{2} - \frac{\pi(J_{13}+J_{23})}{2} - \pi J_{12}) \\ \bar{S}_{p,1,2}(\frac{\omega_1+\omega_2}{2} + \frac{M^+}{2} + \frac{\pi(J_{13}+J_{23})}{2} - \pi J_{12}) \\ \bar{S}_{p,1,2}(\frac{\omega_1+\omega_2}{2} + \frac{M^-}{2} - \frac{\pi(J_{13}+J_{23})}{2} + \pi J_{12}) \\ \bar{S}_{p,1,2}(\frac{\omega_1+\omega_2}{2} + \frac{M^+}{2} + \frac{\pi(J_{13}+J_{23})}{2} + \pi J_{12}) \end{pmatrix} \\
& = \frac{1}{2^n} \times \begin{pmatrix} Tr\{\rho_0 2\tilde{I}_{1+}\} \\ Tr\{\rho_0 4\tilde{I}_{1+}\tilde{I}_{2z}\} \\ Tr\{\rho_0 4\tilde{I}_{1+}\tilde{I}_{3z}\} \\ Tr\{\rho_0 8\tilde{I}_{1+}\tilde{I}_{2z}\tilde{I}_{3z}\} \\ Tr\{\rho_0 2\tilde{I}_{2+}\} \\ Tr\{\rho_0 4\tilde{I}_{1z}\tilde{I}_{2+}\} \\ Tr\{\rho_0 4\tilde{I}_{2+}\tilde{I}_{3z}\} \\ Tr\{\rho_0 8\tilde{I}_{1z}\tilde{I}_{2+}\tilde{I}_{3z}\} \end{pmatrix}, \tag{5.3}
\end{aligned}$$

where

$$\begin{aligned}
A &= \frac{\sin\theta^-}{\cos\theta^- - \sin\theta^-}, & B &= \frac{\sin\theta^-}{\cos\theta^- + \sin\theta^-}, \\
C &= \frac{\sin\theta^+}{\cos\theta^+ - \sin\theta^+}, & D &= \frac{\sin\theta^+}{\cos\theta^+ + \sin\theta^+}, \\
E &= \frac{\cos\theta^-}{\cos\theta^- + \sin\theta^-}, & F &= \frac{\cos\theta^+}{\cos\theta^+ + \sin\theta^+}, \\
G &= \frac{\cos\theta^-}{\cos\theta^- - \sin\theta^-}, & K &= \frac{\cos\theta^+}{\cos\theta^+ - \sin\theta^+} \text{ and } n = 3.
\end{aligned}$$

$$\begin{aligned}
& 2^{1-n} \begin{pmatrix} 1 & 1 & 1 & 1 & 1 & 1 \\ -S & -1 & P & -P & 1 & S \\ S & -1 & -P & P & 1 & -S \\ -1 & 1 & -1 & -1 & 1 & -1 \\ Q & 0 & -Y & -R & 0 & M \\ -M & 0 & R & Y & 0 & -Q \end{pmatrix} \times \\
& \begin{pmatrix} \bar{S}_{p,3}(\omega_3 + \frac{-M^+ - M^-}{2}) \\ \bar{S}_{p,3}(\omega_3 - \pi(J_{13} + J_{23})) \\ \bar{S}_{p,3}(\omega_3 + \frac{M^+ - M^-}{2}) \\ \bar{S}_{p,3}(\omega_3 + \frac{-M^+ + M^-}{2}) \\ \bar{S}_{p,3}(\omega_3 + \pi(J_{13} + J_{23})) \\ \bar{S}_{p,3}(\omega_3 + \frac{M^+ + M^-}{2}) \end{pmatrix} \\
& = \frac{1}{2^n} \times \begin{pmatrix} Tr\{\rho_0 2\tilde{I}_{3+}\} \\ Tr\{\rho_0 4\tilde{I}_{1z}\tilde{I}_{3+}\} \\ Tr\{\rho_0 4\tilde{I}_{2z}\tilde{I}_{3+}\} \\ Tr\{\rho_0 8\tilde{I}_{1z}\tilde{I}_{2z}\tilde{I}_{3+}\} \\ Tr\{\rho_0 8\tilde{I}_{1-}\tilde{I}_{2+}\tilde{I}_{3+}\} \\ Tr\{\rho_0 8\tilde{I}_{1+}\tilde{I}_{2-}\tilde{I}_{3+}\} \end{pmatrix}, \tag{5.4}
\end{aligned}$$

where

$$\begin{aligned}
S &= \frac{\sin(\theta^- + \theta^+)}{\sin(\theta^- - \theta^+)}, & P &= \frac{\cos(\theta^- + \theta^+)}{\cos(\theta^- - \theta^+)}, \\
Q &= \frac{(2\cos(\theta^- - \theta^+) + 2\cos(\theta^- + \theta^+))}{\sin(\theta^- - \theta^+)}, & Y &= \frac{(2\sin(\theta^- - \theta^+) - 2\sin(\theta^- + \theta^+))}{\cos(\theta^- - \theta^+)}, \\
R &= \frac{(2\sin(\theta^- - \theta^+) + 2\sin(\theta^- + \theta^+))}{\cos(\theta^- - \theta^+)}, & M &= \frac{(2\cos(\theta^- - \theta^+) - 2\cos(\theta^- + \theta^+))}{\sin(\theta^- - \theta^+)} \text{ and } n = 3.
\end{aligned}$$

As we mentioned in the previous chapter, there are 14 allowed transitions. The first 12 out of 14 transitions are first order transitions and the last two transitions are multiple quantum transitions. The multiple quantum transitions, which are not present in weakly coupled systems, add further information to a single spectrum. This feature allows one to reduce the number of experiments needed to complete the tomography of the density matrix. Equation (5.3) contains 8 coefficients of the expansion $(\rho = \frac{1}{2^n} I_D + \sum_{s=1}^{4^n-1} \rho_s P_{n,s})$,

while Eq. (5.4) contains 6 coefficients. Solving these two equations, we can determine 14 coefficients of the density matrix with one measurement. To determine the remaining coefficients we need additional measurements with different preparatory pulses. For three weakly coupled spins, we need twelve separate measurements, ten measurements to observe spins 1 and 2 and two measurements to observe spin 3 [25]. In “*ABX*” systems, we found that it can be reduced for example to nine experiments which are shown in Table (5.3).

Observe on spins 1 and 2 (“ <i>AB</i> ”)	Observe on spin 3 (“ <i>X</i> ”)
<i>III, IIX, IYY, IXI, IYI, XXX</i>	<i>III, IIX, IYY</i>

Tab. 5.3: Nine pulse sets that, together, yield complete tomography on an “*ABX*” spin system.

We have found that the number of experiments necessary to perform QST in an “*ABX*” system can be reduced in respect to three weakly coupled qubits. Therefore our method can reduce the experimental effort required for the complete density matrix reconstruction. To test the method derived in the previous chapter (or Eqs. (5.3) and (5.4)), we have implemented the quantum teleportation protocol, a process by which quantum information is transmitted without sending the physical system initially carrying the information [79]. The results demonstrate that good accuracy in the density matrix reconstruction can be achieved with the method.

— SUBSECTION: 5.2.1 —

Quantum Teleportation

Quantum teleportation is one of the most striking phenomena on quantum information processing. Discovered in 1993 [79], it was described in a quantum circuit by Brassard et al. [80] in 1998 (see Fig. (5.4)). The protocol implements a process by which quantum

information is transmitted from one location to another without sending the physical system initially carrying the information along the path connecting the two locations [79]. It has applications in quantum communications [81] and fault-tolerant quantum computing [82], among others. Therefore it is desirable to peruse high precision quantum teleportation at long distance and as well as at atomic scale. The first reported teleportation experiments were performed with photons in 1997 [83, 84]. The first complete teleportation experiment was done by Nielsen et al. using NMR in 1998 [85].

The quantum teleportation protocol is described ideally in terms of two parties, Alice and Bob. Alice has in her possession an unknown state $|\psi\rangle = a|0\rangle - b|1\rangle$ of a single quantum bit, labeled here as qubit 1. Here, a and b are normalization factors. The goal of teleportation is to transport the state of that qubit to Bob. To run the protocol, Alice performs joint measurements on her qubit and a second qubit, which is entangled with a qubit in Bob's possession. Then, Bob's qubit is unitarily transformed according to the result of Alice's measurements. The protocol described as a quantum circuit which was proposed by Brassard, Braunstein, and Cleve [80], is shown in Fig. (5.4).

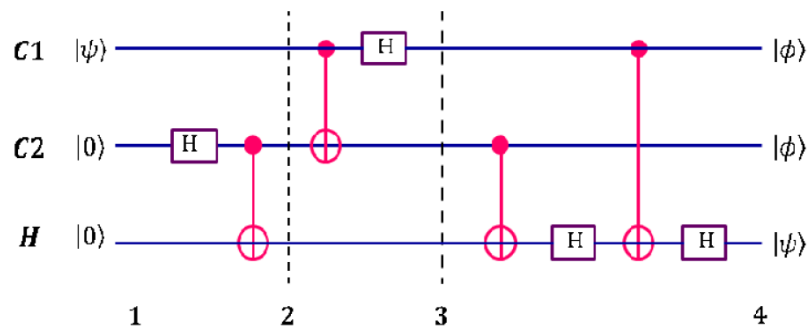


Fig. 5.4: Quantum circuit diagram for the teleportation protocol. Here $C1$ and $C2$ are denoted as qubit 1 and qubit 2, respectively and H is denoted as qubit 3. Numbers written at the bottom of the picture are marks that indicate the steps of the teleportation. H 's inside the rectangles are Hadamard gates and $|\phi\rangle = (|0\rangle + |1\rangle)/\sqrt{2}$.

The top line of the circuit in Fig. (5.4) represents the qubit that Alice wants to teleport, the second and third lines represent the entangled pair that will be shared by Bob and Alice, while the second qubit is with Alice and the third with Bob. The circuit

is divided into different blocks. We will now go through each step in the circuit. In the first step, the qubit to be teleported is prepared in the state $|\psi\rangle = (a|0\rangle - b|1\rangle)$, where a and b are equal to $\frac{1}{\sqrt{2}}$. So, the overall quantum state starts in a tensor product of the three individual states; let's call this $|\psi_1\rangle$:

$$|\psi_1\rangle = |\psi\rangle_A |0\rangle_A |0\rangle_B = a|000\rangle - b|100\rangle, \quad (5.5)$$

where subscript A is used to denote Alice's systems, and subscript B to denote Bob's system. At the second step, qubits 2 and 3 are entangled, a Hadamard gate on second qubit and then a CNOT gate with the second qubit as control and the third qubit as target are applied, resulting in the state:

$$|\psi_2\rangle = |\psi\rangle_A (|0\rangle_A |0\rangle_B + |1\rangle_A |1\rangle_B) / \sqrt{2}. \quad (5.6)$$

Then, Alice and Bob share a two qubit entangled state. In the next step, qubits 1 and 2 are rotated to the Bell basis leading to the state:

$$\begin{aligned} |\psi_3\rangle = & \frac{1}{2} [|00\rangle (a|0\rangle - b|1\rangle) + |01\rangle (a|1\rangle - b|0\rangle) \\ & + |10\rangle (a|0\rangle + b|1\rangle) + |11\rangle (a|1\rangle + b|0\rangle)]. \end{aligned} \quad (5.7)$$

In the last step, Bob's qubit is changed according to the Alice's qubits state. This step can be done performing controlled operations with Alice's qubits as controls and Bob's qubit as the target. At the final, we will have:

$$|\psi_4\rangle = |\phi\rangle_A |\phi\rangle_A |\psi\rangle_B, \quad (5.8)$$

where $\phi = \frac{|0\rangle+|1\rangle}{\sqrt{2}}$ and $\psi = \frac{|0\rangle-|1\rangle}{\sqrt{2}}$. So, the state $|\psi\rangle$ will be transferred to the lower output, whereas both other outputs will come out in the state $\phi = \frac{|0\rangle+|1\rangle}{\sqrt{2}}$. In other words, the output will be $|\phi\phi\psi\rangle$.

For the present experimental implementation we have used a sample of trichloroethy-

lene dissolved in deuterated chloroform (see previous section). Experiment was performed at room temperature using Varian 500-MHz spectrometer. Quantum gates were optimized using the GRAPE algorithm (see Table (5.2)), and the density matrices were reconstructed using the results of the previous chapter. To perform teleportation we make use of the Hydrogen nucleus (H), and the two Carbon nuclei ($C1$ and $C2$), teleporting the state of $C1$ to H . In the beginning of the experiment we must create the pseudo-pure state from the thermal equilibrium state. The thermal equilibrium density matrix for three spins in the high temperature limit, given by:

$$\rho_{eq} \approx \frac{I}{2^3} + \frac{\hbar\beta}{2^3} \sum_{k=1}^3 \omega_k I_z^k = \frac{I}{8} + \frac{\hbar\beta\gamma_c B_0}{8} [I_z^1 + I_z^2 + \frac{\omega_H}{\omega_C} I_z^3], \quad (5.9)$$

can be transformed into a pseudo-pure ground state:

$$\rho = \frac{1-\epsilon}{8} I + \epsilon |000\rangle\langle 000|, \quad (5.10)$$

where $\beta = 1/k_B T$ is the Boltzmann factor, ω_k are respective chemical shifts, I is the identity matrix, I_z^k is the z component of the nuclear spin angular momentum operator for the k th spin and $\epsilon = \hbar\omega_k\beta \simeq 10^{-5}$ at room temperature. We have used spatial averaging for the preparation of the pseudo-pure state (see chapter (2)). The sequence used to initialize the spin system to the pseudo-pure state is given in Fig. (5.5).

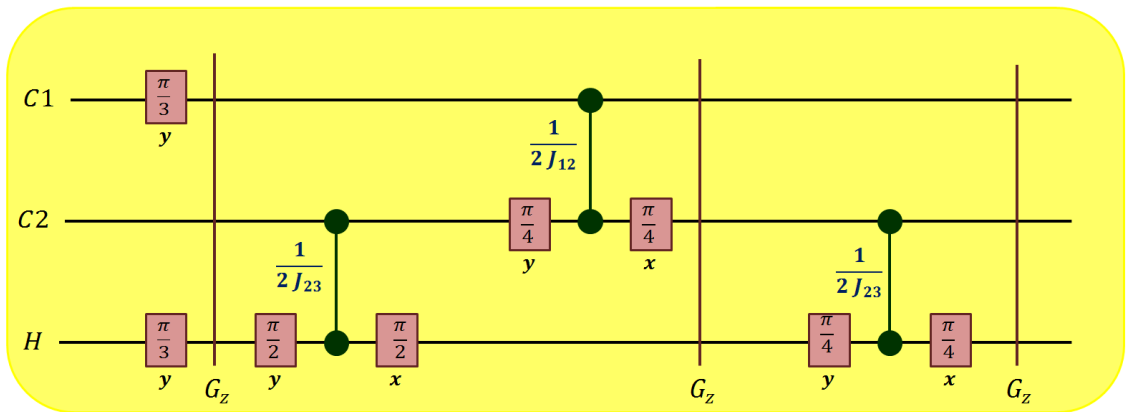


Fig. 5.5: Pulse sequence used to prepare three-qubit pseudo-pure state, where G_z is the magnetic field gradient along z axis.

So the spin system is initialized in the pseudo-pure state $|\psi_0\rangle = |000\rangle$ (Fig. (5.6)(a)). Then after the initialization, the first two steps of the circuit in Fig. (5.4) are implemented: In the first step the state to be teleported $|\psi\rangle = a|0\rangle - b|1\rangle$, with $a = b = 1/\sqrt{2}$, is prepared on the first qubit and both other inputs to $|0\rangle$ and, in the second step, a pseudoentangled pair is created between the second and third qubits. In Fig. (5.6), we show the experimental density matrices for the pseudo-pure state, $|\psi_0\rangle = |000\rangle$, and after the first two steps, $|\psi_1\rangle = |\psi 00\rangle$ and $|\psi_2\rangle = (|\psi 00\rangle + |\psi 11\rangle)/\sqrt{2}$. The fidelity was over 0.97 in all these cases according to Eq. (5.2).

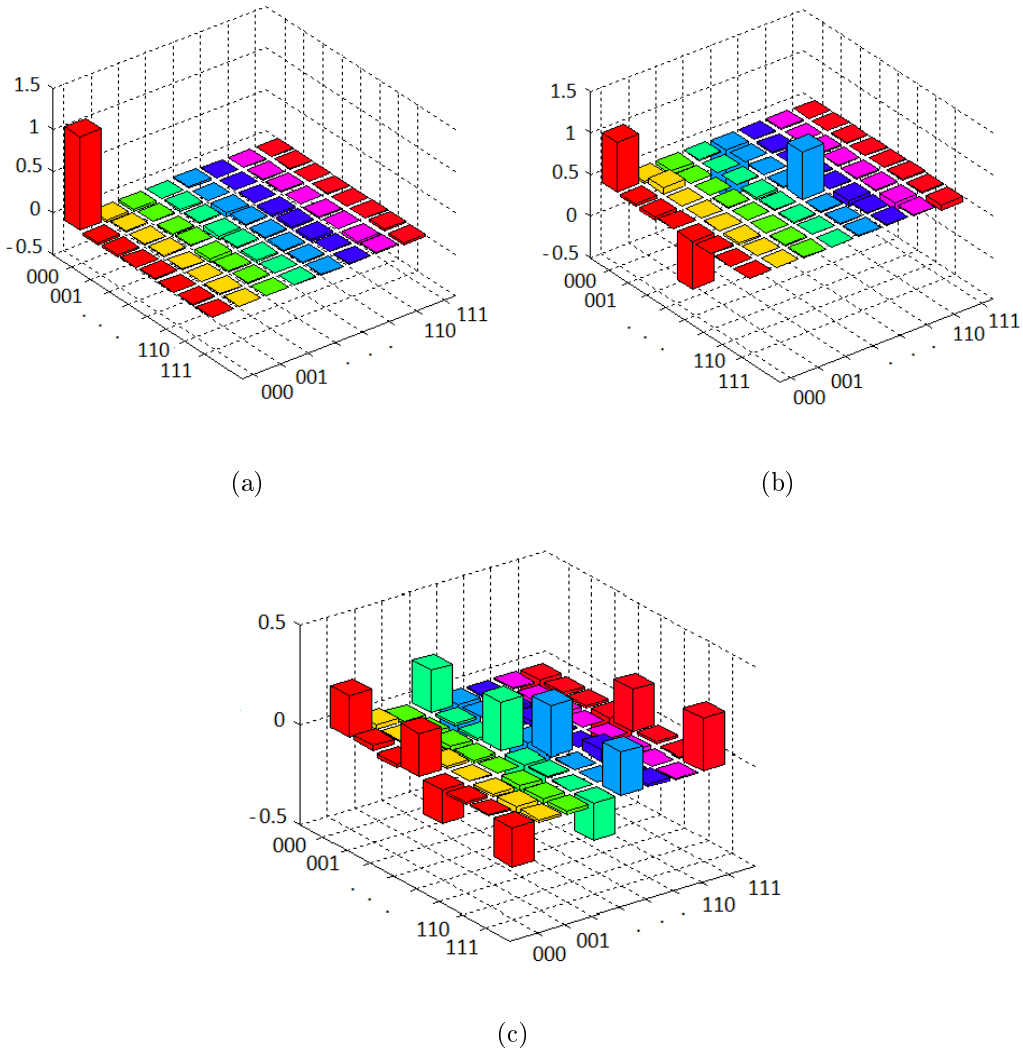
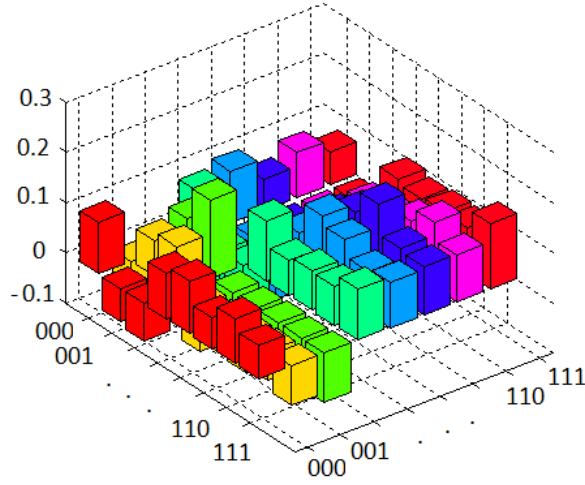
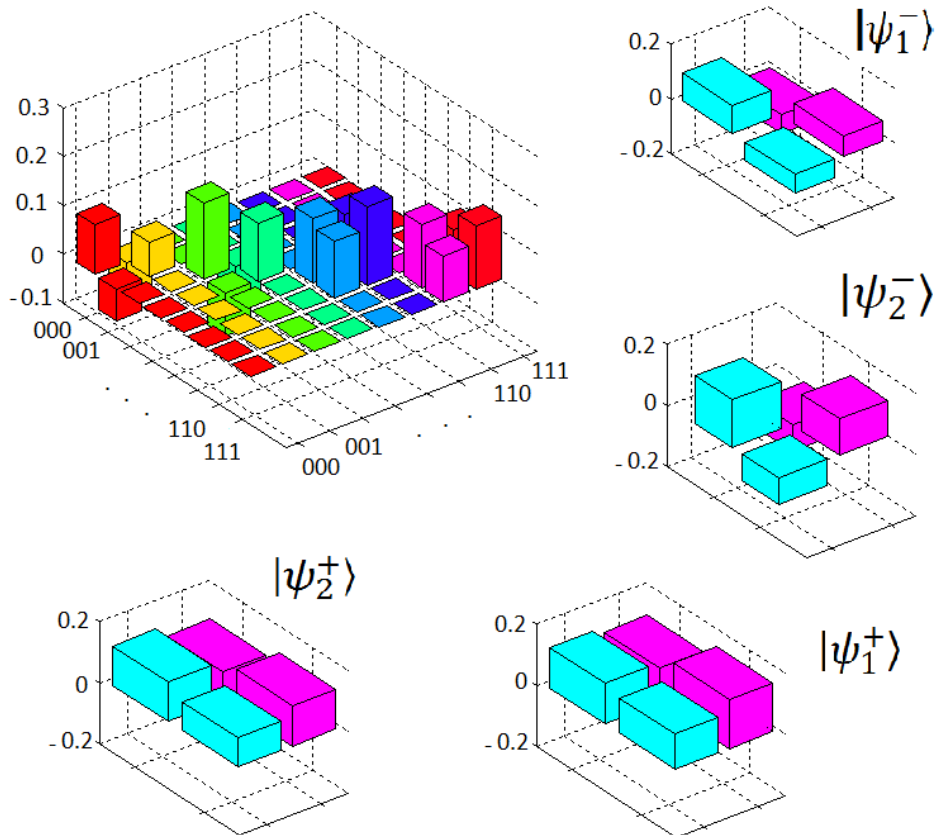


Fig. 5.6: Experimental three-qubit density matrices for the teleport experiment. From (a) to (c) are shown the real parts of the reconstructed density matrices of the pseudo-pure state, $|\psi_0\rangle = |000\rangle$, first step, $|\psi_1\rangle = |\psi 00\rangle$, and second step, $|\psi_2\rangle = \frac{(|\psi 00\rangle + |\psi 11\rangle)}{\sqrt{2}}$, of the teleportation, respectively. The rows and columns represent the standard computational basis in binary order, with $\langle 000|$ starting from the leftmost column and $\langle 111|$ being the rightmost column.

The result for the third step is shown in the computational basis and in the Bell basis in Fig. (5.7). As it can be seen in the Fig. (5.7), the state of the third qubit is conditioned to the state of the two first qubits, and the fidelity of the third step was 0.96.



(a)



(b)

Fig. 5.7: Experimental density matrices: The real part of the reconstructed density matrix of the third step of the teleportation in (a) the computational basis, $|\psi_3\rangle$, (b) the Bell basis. The state is in an equal mixture of the four different possible combinations. For clarity, we zoomed on the submatrices along the diagonal to show the four different states in Eq. (5.7) more clearly ($|\psi_1^\pm\rangle = (1/\sqrt{2})(|0\rangle \pm |1\rangle)$) and $|\psi_2^\pm\rangle = (1/\sqrt{2})(|1\rangle \pm |0\rangle)$). The rows and columns represent the standard computational basis in binary order, with $|000\rangle$ starting from the leftmost column and $|111\rangle$ being the rightmost column.

To complete the teleportation, we need to implement the controlled-NOT operation between the Alice's qubits and Bob's qubit. Since the strength of the interaction between qubits one and three is very small in our case, we have implemented the final step, shown in Fig. (5.4), in a different manner. The $CNOT_{13}$ gate with the first qubit as control and the third qubit as target can be entirely constructed out of two $SWAP_{12}$ gates and one $CNOT_{23}$ gate with the second qubit as control and the third qubit as target [86]: $CNOT_{13} = SWAP_{12} CNOT_{23} SWAP_{12}$, where $SWAP_{12} = CNOT_{12} CNOT_{21} CNOT_{12}$ swaps qubits 1 and 2. The second SWAP gate does not need to be implemented since we can leave qubits 1 and 2 swapped. Therefore, we have implemented the final step as in Fig. (5.8). The final density matrix is shown in Fig. (5.9), the third qubit is in the $|\psi\rangle = (|0\rangle - |1\rangle)/\sqrt{2}$ state, independently of the two other qubits. The fidelity of the final density matrix was found to be 0.94.

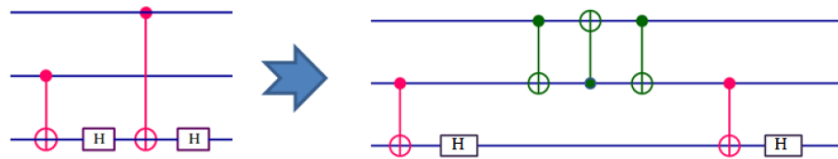


Fig. 5.8: Final step of the teleportation protocol.

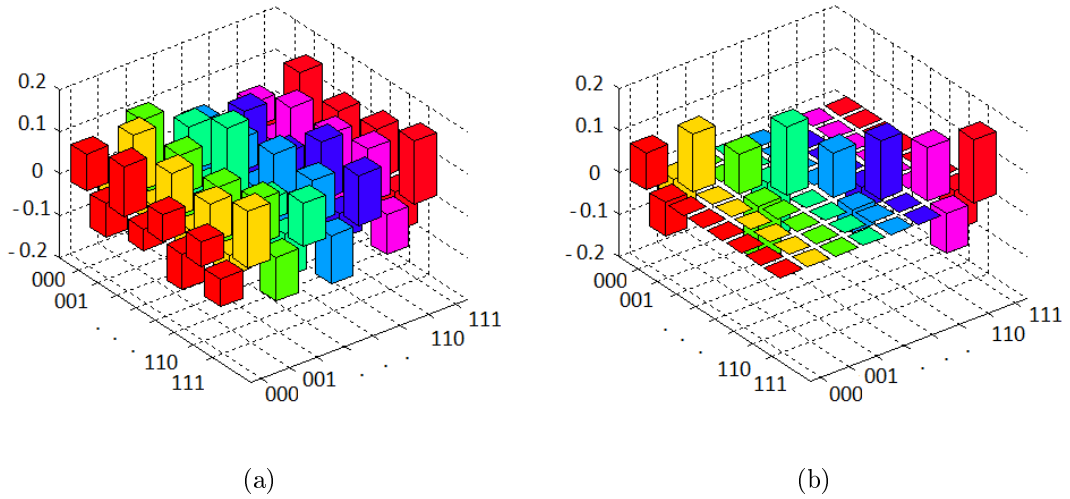


Fig. 5.9: Experimental density matrix: the real part of the final reconstructed density matrix in (a) the computational basis, $|\psi_4\rangle = \left(\frac{|0\rangle+|1\rangle}{\sqrt{2}}\right)\left(\frac{|0\rangle+|1\rangle}{\sqrt{2}}\right)|\psi\rangle = \left(\frac{|0\rangle+|1\rangle}{\sqrt{2}}\right)\left(\frac{|0\rangle+|1\rangle}{\sqrt{2}}\right)\left(\frac{|0\rangle-|1\rangle}{\sqrt{2}}\right)$ and (b) the Bell basis. The rows and columns represent the standard computational basis in binary order, with $\langle 000|$ starting from the leftmost column and $\langle 111|$ being the rightmost column.

It is important to note that all NMR experiments were performed using regular shaped pulses. As we showed, the number of experiments needed to implement QST in “*ABX*” systems can be reduced with respect to three weakly coupled spins. Therefore our method can reduce the experimental effort required for complete density matrix reconstruction.

6

NMR Implementation of Two-Dimensional YANG-BAXTER Equation

The Yang-Baxter Equation (YBE) is a sufficient condition for the integrability of a model. This means that if a model is constructed from the Yang-Baxter Equation, it will be called an integrable model, which means that it can be solved exactly, i.e., we will know its eigenvalues and eigenfunctions. This mathematical construction was introduced by C.N. Yang and R. Baxter in different contexts. So, the Yang-Baxter Equation originally arose in Yang's study of the many body problem in one-dimension with repulsive delta-function interaction [1], and Baxter's solution of the eight vertex model from statistical mechanics [2, 3]. It turned out to be one of the basic equations in mathematical physics, and more precisely for introducing the theory of quantum groups. The Yang-Baxter Equation also plays an important role in quantum field theory, statistical mechanics, group theory, completely integrable statistical models, Knot theory, braided categories, quantum computing, etc [87, 88, 89, 90, 91, 92, 93, 94, 95, 96, 97, 98]. Recently it turns up gradually that

the Yang-Baxter Equation is naturally linked to the quantum information and computing [38, 39]. It is found that the Yang-Baxter Equation is closely related to quantum entangled states [40, 41], the braiding operations in the Yang-Baxter Equation are universal quantum gates [42, 43, 44, 45, 46]. The Yang-Baxter Equation attracts much attention in recent years and is being studied in the context of quantum correlation and entanglement, and topological quantum computing intensively [47, 48, 49, 50, 51, 52, 53, 54]. The YBE is a universal gate for quantum computation; some solutions of the YBE are unitary and therefore can be seen as a quantum gate.

Hu, Xue and Ge in 2008 gave an explicit optical realization of the Yang-Baxter Equation [4]. By the use of the Temperley-Lieb algebra, they made a remarkable reduction that obtained a Yang-Baxter Equation with dimension 2, the minimum dimensional Yang-Baxter Equation so far. This makes it possible to be implemented in quantum optics with current technology. In this chapter, we test the two-dimensional (2D) Yang-Baxter Equation (YBE) using Nuclear Magnetic Resonance (NMR). We present a practical scheme to test the YBE in the framework of quantum information. Then we experimentally test the validity of 2D YBE in NMR. The equality of the two sides of the Yang-Baxter equation is directly verified.

At the first, we start with quantum optics and introduce simplest form of the Yang-Baxter Equation in two-dimension and show how we can implement the 2D Yang-Baxter Equation in quantum optics, then we go to Nuclear Magnetic Resonance part and also show how we can implement the 2D Yang-Baxter Equation in NMR with experimental results.

SECTION: 6.1

Implementation of the Yang-Baxter Equation in Quantum Optics

In this part, we show how we can implement the 2D Yang-Baxter Equation in quantum optics. For implementation of the 2D Yang-Baxter Equation in quantum optics, there are two ways, polarization qubit and location qubit. we briefly describe these two ways.

SUBSECTION: 6.1.1

Reduction of the 4D YBE to the 2D YBE

The basic formula of the 4D Yang-Baxter Equation states that a matrix \check{R} acting on the tensor product $\nu \otimes \nu$, satisfies [4]:

$$\check{R}_{12}(u) \check{R}_{23}\left(\frac{u+v}{1+\beta^2 uv}\right) \check{R}_{12}(v) = \check{R}_{23}(v) \check{R}_{12}\left(\frac{u+v}{1+\beta^2 uv}\right) \check{R}_{23}(u), \quad (6.1)$$

where $\check{R}_{12} = \check{R} \otimes 1$, $\check{R}_{23} = 1 \otimes \check{R}$, u and v are parameters, which usually range over all positive real numbers (they are called spectral parameters), and $\beta^{-1} = ic$ (c is the light speed in vacuum).

\check{R} is the two-particle scattering matrix depending on the relative rapidity $\tanh^{-1}(\beta u)$. When $\beta u = 1$, $\check{R} = b$ which is a braid matrix, and the Yang-Baxter Equation reduces to the braid relation $b_{12} b_{23} b_{12} = b_{23} b_{12} b_{23}$. This equation implies the scattering of particles 1 and 2, followed by scattering of particles 2 and 3, and then scattering of particles 1 and 2, is equal to the scattering of particles 2 and 3, followed by scattering of particles 1 and 2, and then scattering of particles 2 and 3, when they satisfy the Yang-Baxter Equation with suitable spectral parameters.

The Yang-Baxter Equation is an abstract equation and the quantities in the equation may have different meanings in different problems. For instance, it has been found re-

cently that the braid matrix and the Yang-Baxter Equation are connected to entangled quantum states [99]. The Bell-basis entangled states in four-dimension can be obtained by applying braid operation that satisfies the Yang-Baxter Equation on the computational basis. Here the matrix in the Yang-Baxter Equation becomes a transformation that transforms the computational basis to the Bell-basis states. There have been active studies in this direction, interested readers can refer to [100] and references therein for more details.

The 4D Yang-Baxter matrices have 2D counterparts which are unitary and much simpler. Furthermore, the 4D YBE, after some calculations and simplifications, as described in [4], can be reduced to the corresponding 2D YBE. Therefore, we have used the 2D YBE for our experimental implementation.

After some calculations described in [4], the 2D YBE can be written as:

$$A(u) B\left(\frac{u+v}{1+\beta^2 uv}\right) A(v) = B(v) A\left(\frac{u+v}{1+\beta^2 uv}\right) B(u), \quad (6.2)$$

$$A(u) = \rho(u) \begin{bmatrix} \frac{1+\beta^2 u^2+2i\epsilon\beta u}{1+\beta^2 u^2-2i\epsilon\beta u} & 0 \\ 0 & 1 \end{bmatrix}, \quad (6.3)$$

$$B(u) = \frac{\rho(u)}{1+\beta^2 u^2-2i\epsilon\beta u} \begin{bmatrix} 1+\beta^2 u^2 & 2i\epsilon\beta u \\ 2i\epsilon\beta u & 1+\beta^2 u^2 \end{bmatrix}, \quad (6.4)$$

where $A(u)$ and $B(u)$ are unitary matrices, $\rho(u)$ is a normalization factor and $\epsilon = \pm 1$. Since these matrices $A(u)$ and $B(u)$ are unitary, then the implementation of the 2D Yang-Baxter Equation is easier than the 4D Yang-Baxter Equation. For the convenience of an experimental test, A and B are represented as functions of an optical parameter θ , the angle between the optical axes of an optical device and the vertical direction. The two sets of parameters are related by using the following transformation:

$$\frac{1+\beta^2 u^2+2i\epsilon\beta u}{1+\beta^2 u^2-2i\epsilon\beta u} \equiv e^{-2i\theta}, \quad (6.5)$$

and

$$\rho(u) \equiv e^{i\theta}. \quad (6.6)$$

Then, $A(u)$ and $B(u)$ unitary matrices become simple matrices in two-dimension:

$$A(u) = \begin{bmatrix} e^{-i\theta} & 0 \\ 0 & e^{i\theta} \end{bmatrix} \equiv A(\theta), \quad (6.7)$$

and

$$B(u) = \begin{bmatrix} \cos(\theta) & -i \sin(\theta) \\ -i \sin(\theta) & \cos(\theta) \end{bmatrix} \equiv B(\theta). \quad (6.8)$$

Therefore in terms of these new parameters (Eqs. (6.5) and (6.6)), the 2D Yang-Baxter Equation can be re-written as:

$$A(\theta_1) B(\theta_2) A(\theta_3) = B(\theta_3) A(\theta_2) B(\theta_1), \quad (6.9)$$

where the angles θ_i are related to a rotation orientation from the vertical direction. These three parameters in the Yang-Baxter Equation θ_1 , θ_2 and θ_3 are not independent, and they are related to each other through the following equation [4]:

$$(e^{-2i\theta_2} + 1)[i - \sec(\theta_1 - \theta_3) \sin(\theta_1 + \theta_3)] = 2i. \quad (6.10)$$

After simplifying Eq. (6.10), relation between the optical angle parameters can be written as:

$$\tan(\theta_2) = \frac{\sin(\theta_1 + \theta_3)}{\cos(\theta_1 - \theta_3)}. \quad (6.11)$$

This equation holds for the angle parameters appearing in the Right-Hand-Side and the Left-Hand-Side of YBE. For the equality in the Eq. (6.9) to be established, the angle parameters (θ_1 , θ_2 and θ_3) must satisfy Eq. (6.11).

The method, that we have used for finding the final form of the $A(\theta)$ and $B(\theta)$ versus

the rotation are the same. The two unitary matrices $A(\theta)$ and $B(\theta)$ can be optically performed with the aid of the polarization qubit or location qubit of a single photon. Therefore, there are two ways to implement the 2D YBE, polarization qubit and location qubit. In the following subsections, we briefly describe these two methods.

SUBSECTION: 6.1.2

Using the Polarization Qubit to Implement the 2D YBE

The polarization qubit can be achieved by encoding the qubit in the photon's polarization with the corresponding transformations implemented by wave plates, such as Half-Wave Plates (HWP) and Quarter-Wave Plates (QWPs). A wave plate is an optical device that alters the polarization state of a light wave travelling through it. Two common types of wave plates are the Half-Wave Plate (HWP), which shifts the polarization direction of linearly polarized light, and the Quarter-Wave Plate (QWP), which converts linearly polarized light into circularly polarized light and vice-versa. A Quarter-Wave Plate can be used to produce elliptical polarization, as well. HWP and QWP are shown in Fig. (6.1).

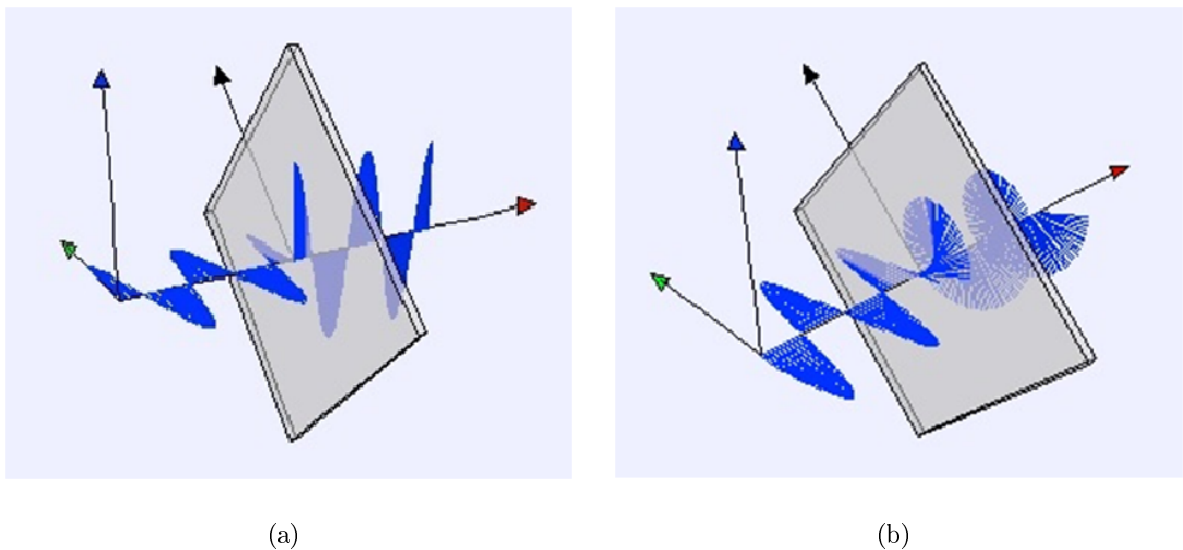


Fig. 6.1: (a) Half-Wave Plate (HWP) and (b) Quarter-Wave Plate (QWP).

The action of a QWP upon the basis states of a polarization qubit is given by [22]:

$$U_Q(\delta) = e^{-i\delta\sigma_y} e^{-i(\frac{\pi}{4})\sigma_z} e^{i\delta\sigma_y} = \frac{1}{\sqrt{2}} \begin{bmatrix} 1 - i \cos(2\delta) & -i \sin(2\delta) \\ -i \sin(2\delta) & 1 + i \cos(2\delta) \end{bmatrix}, \quad (6.12)$$

where σ_i are Pauli matrices and δ is the angle between the QWP axis and the vertical direction. Then, the action of a HWP upon the basis states of a polarization qubit is given by:

$$U_H(\delta) = U_Q^2(\delta) = -i \begin{bmatrix} \cos(2\delta) & \sin(2\delta) \\ \sin(2\delta) & -\cos(2\delta) \end{bmatrix}. \quad (6.13)$$

According to [22], the sandwich configuration of one HWP and two QWPs enables one to perform any unitary change of the photons polarization state. So, the terms $A(\theta)$ and $B(\theta)$ can be decomposed into a combinations of operators of a qubit in linear optics as the following manner:

$$A(\theta) = U_Q(\frac{\pi}{4}) U_H(\frac{\theta}{2} - \frac{\pi}{4}) U_Q(\frac{\pi}{4}), \quad (6.14)$$

$$B(\theta) = U_Q(\frac{\pi}{2}) U_H(\frac{\theta}{2}) U_Q(\frac{\pi}{2}). \quad (6.15)$$

Eq. (6.13) implies that Eqs. (6.14) and (6.15) can be associated to the action of the QWP (U_Q). We need $U_Q(\frac{\pi}{4})$, $U_Q(\frac{\pi}{2})$, $U_Q(\frac{\theta}{2} - \frac{\pi}{4})$ and $U_Q(\frac{\theta}{2})$ for the calculation of $A(\theta)$ and $B(\theta)$ matrices. The sequence of pulses to implement them in a experimental setup can be written as (time goes from left to right):

$$U_Q(\frac{\pi}{4}) = (\frac{\pi}{2})_y \rightarrow (\frac{\pi}{2})_z \rightarrow (\frac{\pi}{2})_{-y}, \quad (6.16)$$

$$U_Q(\frac{\pi}{2}) = (\pi)_y \rightarrow (\frac{\pi}{2})_z \rightarrow (\pi)_{-y}, \quad (6.17)$$

$$\begin{aligned}
U_H\left(\frac{\theta}{2} - \frac{\pi}{4}\right) &= U_Q\left(\frac{\theta}{2} - \frac{\pi}{4}\right) U_Q\left(\frac{\theta}{2} - \frac{\pi}{4}\right) \\
&= (\theta)_y \rightarrow \left(\frac{\pi}{2}\right)_{-y} \rightarrow (\pi)_z \rightarrow \left(\frac{\pi}{2}\right)_y \rightarrow (\theta)_{-y}, \quad (6.18)
\end{aligned}$$

$$U_H\left(\frac{\theta}{2}\right) = U_Q\left(\frac{\theta}{2}\right) U_Q\left(\frac{\theta}{2}\right) = (\theta)_y \rightarrow (\pi)_z \rightarrow (\theta)_{-y}, \quad (6.19)$$

where $(\theta)_x = e^{-i\theta I_x}$, $(\theta)_y = e^{-i\theta I_y}$ and $(\theta)_z = e^{-i\theta I_z}$. Using the above equations, we can write the Left-Hand-Side and the Right-Hand-Side of the YBE. For calculation the both sides of the YBE, first we must calculate $A(\theta)$ and $B(\theta)$. First, we calculate $A(\theta)$. By substituting Eqs. (6.16) and (6.18) into the Eq. (6.14) and by considering the relation below:

$$(\theta)_x = \left(\frac{\pi}{2}\right)_{-y} \rightarrow (\theta)_z \rightarrow \left(\frac{\pi}{2}\right)_y, \quad (6.20)$$

$A(\theta)$ can be calculated as follows:

$$A(\theta) = \left(\frac{\pi}{2}\right)_{-x} \rightarrow (2\theta)_y \rightarrow \left(\frac{\pi}{2}\right)_x = (2\theta)_z. \quad (6.21)$$

Let us now calculate $B(\theta)$. By substituting Eqs. (6.17) and (6.19) into the Eq. (6.15) and by considering the relation below:

$$(\theta)_{-z} = (\pi)_y \rightarrow (\theta)_z \rightarrow (\pi)_{-y}, \quad (6.22)$$

$B(\theta)$ can be calculated as follows:

$$B(\theta) = \left(\frac{\pi}{2}\right)_{-z} \rightarrow (2\theta)_y \rightarrow \left(\frac{\pi}{2}\right)_z = (2\theta)_{-x}. \quad (6.23)$$

The optical operations of $A(\theta)$ and $B(\theta)$ in terms of Quarter-Wave Plates (QWP) and Half-Wave Plates (HWP) are shown in Fig. (6.2).

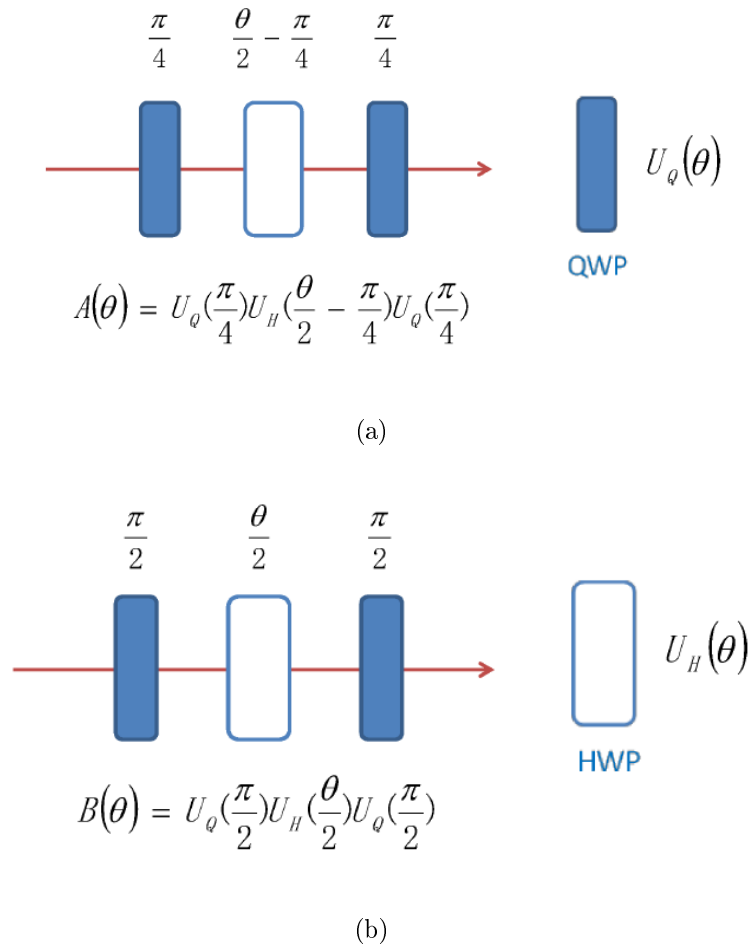
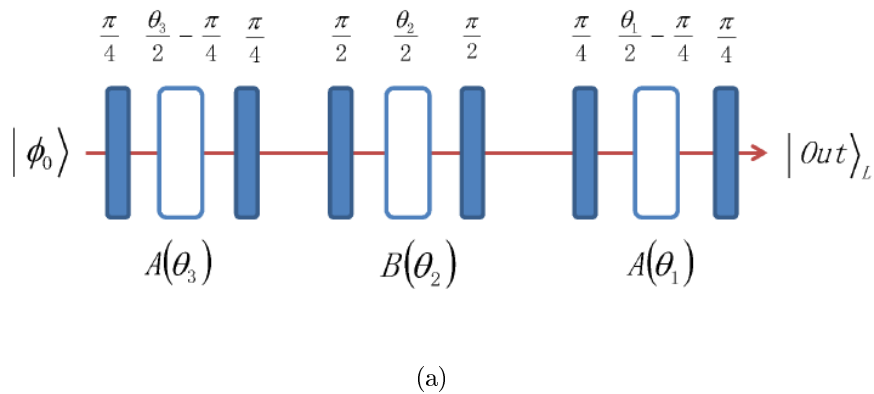


Fig. 6.2: Realization of operations (a) $A(\theta)$ and (b) $B(\theta)$ by optical elements. $U_Q(\theta)$ and $U_H(\theta)$ are the matrices of QWP and HWP, respectively, and θ is the angle between the optical device axes and the vertical direction.

The two sides of the Yang-Baxter Equation are implemented by two series of wave plates as illustrated in Fig. (6.3).



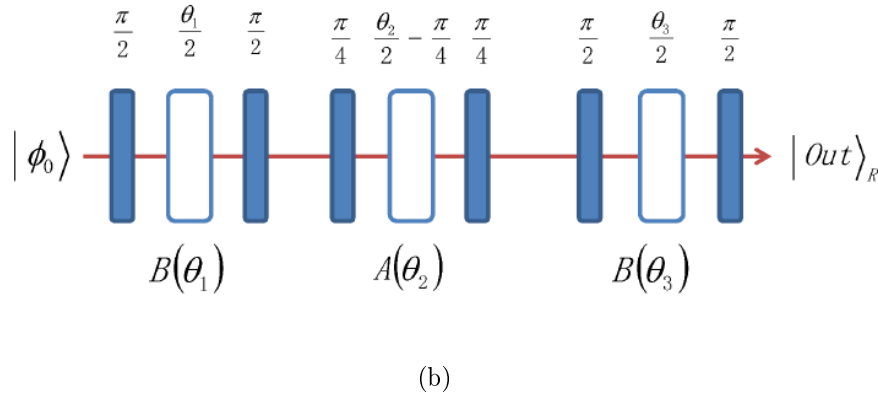


Fig. 6.3: Optical realization of the (a) Left-Hand-Side and Right-Hand-Side of the Yang-Baxter equation. The angles of these QWPs (filled) and HWPs (empty) must satisfy the relation given in Eq. (6.11).

SUBSECTION: 6.1.3

Using the Location Qubit to Implement the 2D YBE

The location qubit can be implemented by encoding the qubit in the single-photon path with the corresponding transformations implemented by beam splitters (BSs), phase shifters (PSs), and mirrors. A beam splitter is an optical device that splits a beam of light in two.

In this case the action of operators $A(\theta)$ and $B(\theta)$ are related to the unitary action of the Mach-Zehnder interferometer with angles correspondences as:

$$A(\theta) = U_{MZ}(\varphi_2 = \varphi_1 = 0, \phi_1 = -\phi_2 = \theta), \quad (6.24)$$

$$B(\theta) = U_{MZ}(\varphi_2 = -\varphi_1 = \theta, \phi_1 = \phi_2 = 0). \quad (6.25)$$

The Mach-Zehnder interferometer is a device used to determine the relative phase shift variations between two collimated beams derived by splitting light from a single source. The unitary action of Mach-Zehnder interferometer is given by:

$$U_{MZ} = e^{i\frac{\Phi}{2}} \begin{bmatrix} e^{-i\phi_1 - \phi_2/2} \cos(\frac{\lambda}{2}) & ie^{-i\phi_1 - \phi_2/2} \sin(\frac{\lambda}{2}) \\ ie^{-i\phi_1 - \phi_2/2} \sin(\frac{\lambda}{2}) & e^{-i\phi_1 - \phi_2/2} \cos(\frac{\lambda}{2}) \end{bmatrix}, \quad (6.26)$$

where the total phase $\Phi = \phi_1 + \phi_2 + \varphi_1 + \varphi_2$ and phase difference $\lambda = \varphi_2 - \varphi_1$. The schematic of the Mach-Zehnder interferometer is shown in Fig. (6.4).

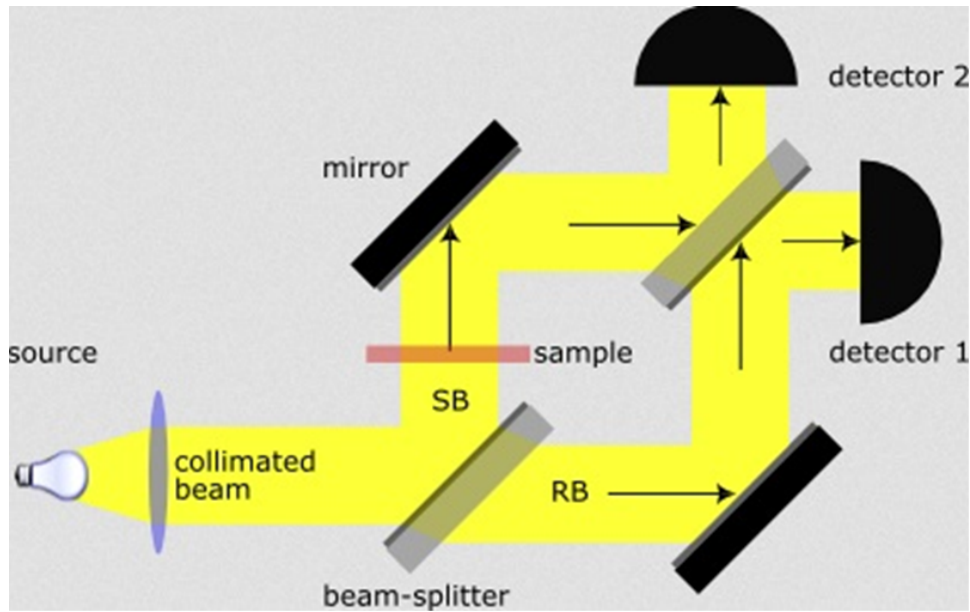


Fig. 6.4: Schematic of the Mach-Zehnder interferometer.

After some calculation, $A(\theta)$ and $B(\theta)$ (Eqs. (6.24) and (6.25)) can be written as:

$$A(\theta) = e^{\frac{\theta}{2}} \begin{bmatrix} e^{-i\theta} & 0 \\ 0 & e^{i\theta} \end{bmatrix} = e^{\frac{\theta}{2}} e^{-i\theta\sigma_z} \cong (2\theta)_z, \quad (6.27)$$

$$B(\theta) = \begin{bmatrix} \cos(\theta) & i \sin(\theta) \\ i \sin(\theta) & \cos(\theta) \end{bmatrix} = e^{i\theta\sigma_x} = (2\theta)_{-x}. \quad (6.28)$$

The whole optical setup to implement both sides of the 2D YBE, Eqs. (6.28) and (6.27), is shown in Fig. (6.5). The angle parameters obey the same relation in Eq. (6.11).

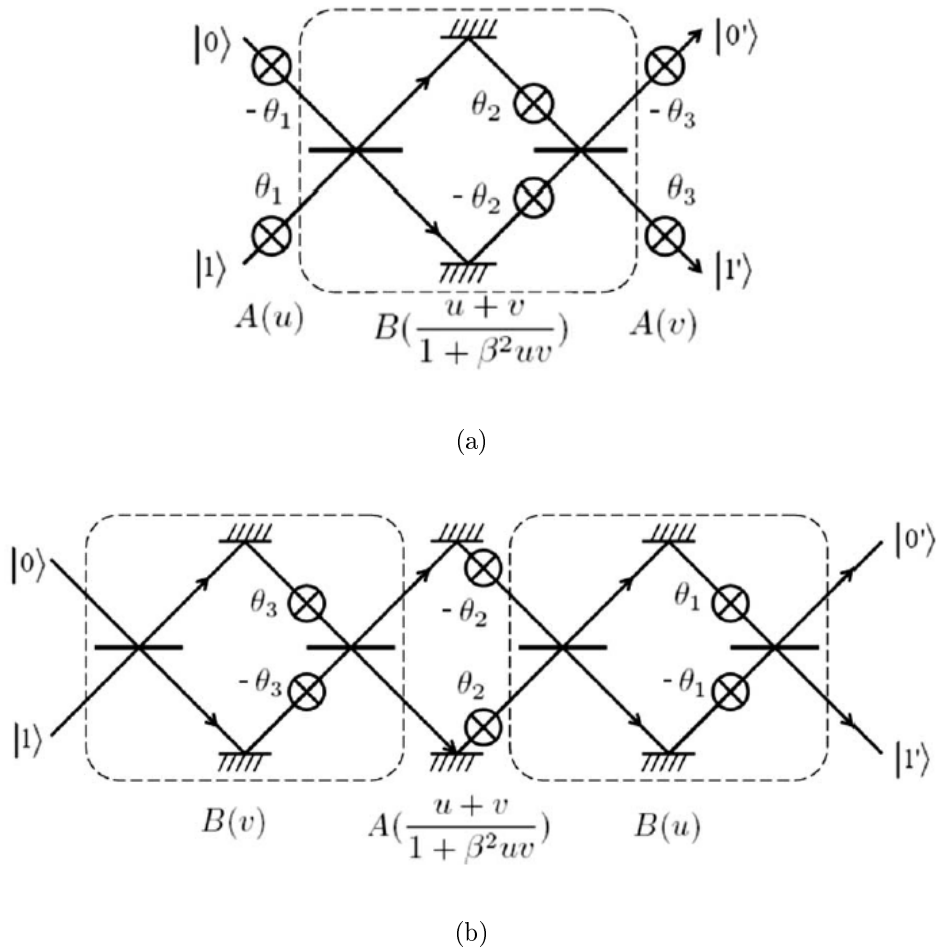


Fig. 6.5: Schematic setup for implementing either side of the 2D YBE, Eqs. (6.28) and (6.27), by means of location qubit. (a) Implementation of the Left-Hand-Side. (b) Implementation of the Right-Hand-Side. The relations of different parameters are referred to Eq. (6.11).

As we can see, the final forms of the $A(\theta)$ and $B(\theta)$ operators for these two qubit options, polarization qubit and location qubit, are the same (Eqs. (6.21) and (6.23) in polarization qubit and Eqs. (6.27) and (6.28) in location qubit). Therefore, the Left-Hand-Side and the Right-Hand-Side of the 2D YBE for polarization qubit and location qubit are the same. Hence for experimental implementation of the 2D YBE in quantum optics, there is not any difference between these two ways. For more details about the implementation of the 2D YBE in quantum optics see [4]. But in this thesis, we have implemented the 2D YBE using Nuclear Magnetic Resonance. In the next section we thoroughly explain how we can implement the 2D YBE using NMR and then we have shown the experimental results.

SECTION: 6.2

Implementation of the 2D YBE in NMR

In this section, we describe the experimental implementation of the 2D YBE using NMR. We want to show that when we apply the Left-Hand-Side of the 2D YBE to one qubit and the Right-Hand-Side of the 2D YBE to another qubit, then we must have the same state for those qubits. At the first, we must calculate the Left-Hand-Side and the Right-Hand-Side of the 2D YBE as a sequence of RF pulses. Our experiment is based on the results described in [4].

In the previous section, we have found the final forms of the $A(\theta)$ and $B(\theta)$ operators (Eqs. (6.21) and (6.23) in polarization qubit and Eqs. (6.27) and (6.28) in location qubit). Now we can calculate each side of the 2D YBE. For the Left-Hand-Side of the 2D YBE, we have:

$$A(\theta_1) B(\theta_2) A(\theta_3) = (2\theta_1)_z \rightarrow (2\theta_2)_{-x} \rightarrow (2\theta_3)_z. \quad (6.29)$$

After some calculation and using these relations:

$$(\theta)_{-z} = \left(\frac{\pi}{2}\right)_y \rightarrow (\theta)_{-x} \rightarrow \left(\frac{\pi}{2}\right)_{-y}, \quad (6.30)$$

$$\left(\frac{\pi}{2}\right)_y \rightarrow (\theta)_z = (\theta)_z \rightarrow \left(\frac{\pi}{2}\right)_{y+\theta}, \quad (6.31)$$

the Left-Hand-Side of the YBE takes the form below:

$$A(\theta_1) B(\theta_2) A(\theta_3) = (2\theta_1 - 2\theta_2 + 2\theta_3)_z \rightarrow \left(\frac{\pi}{2}\right)_{-y-2\theta_2+2\theta_3} \rightarrow \left(\frac{\pi}{2}\right)_{y+2\theta_3}. \quad (6.32)$$

The Right-Hand-side of the YBE, after some calculation the same as above, becomes:

$$B(\theta_3) A(\theta_2) B(\theta_1) = \left(\frac{\pi}{2}\right)_{-y} \rightarrow (-2\theta_3 + 2\theta_2 - 2\theta_1)_z \rightarrow \left(\frac{\pi}{2}\right)_{y+2\theta_2-2\theta_1} \rightarrow \left(\frac{\pi}{2}\right)_{-y-2\theta_1} \rightarrow \left(\frac{\pi}{2}\right)_y. \quad (6.33)$$

Now it is straightforward to design the NMR experimental setup for implementation of the 2D YBE, as described in the this section. For the experimental implementation, we have used a sample of iodotrifluoroethylene dissolved in deuterated-acetone (see Fig. (6.6)). Data were taken with a Varian 500-MHz spectrometer at room temperature, quantum gates were optimized using the GRAPE algorithm (see chapter (3))[11] and the method which is explained in [101]. In this sample, the phase decoherence times (T_2) for F_1 , F_2 and F_3 are approximately 0.08 s, 0.09 s and 0.08 s, respectively. The coupling constants and chemical shifts are given in Table (6.1). Table (6.2) show the control parameters for each GRAPE pulse used in this experiment (see chapter (3)).

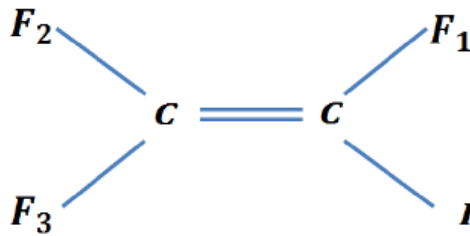


Fig. 6.6: The structure of the iodotrifluoroethylene molecule.

(Hz)	F_1	F_2	F_3
F_1	11834.8	69.86	47.65
F_2	69.86	0	-128.1
F_3	47.65	-128.1	-17325.7

Tab. 6.1: The parameters of fluorine labeled iodotrifluoroethylene molecule. The diagonal terms in the table are the chemical shifts (in Hz) of the fluorines. The off-diagonal terms are the coupling constants, also in Hz.

Pulse	Time step	Total time	Fidelity
$R_x^1(\frac{\pi}{2})$	1 μs	1000 μs	0.9999
$R_x^2(\frac{\pi}{2})$	1 μs	1000 μs	1
$R_x^3(\frac{\pi}{2})$	1 μs	1000 μs	0.9999

Tab. 6.2: Control parameters input into the GRAPE algorithm for iodotrifluoroethylene molecule.

We have done this experiment three times. In the first time, all quantum gates were optimized using GRAPE algorithm and the results were not good. In the second time, GRAPE algorithm was improved and the results were better than the first time. In the last time, we have improved again GRAPE algorithm and we have also considered the errors before and after each pulse [101] and the results were very good. Now, we want to explain each step of the 2D YBE experiment and show the results.

In the beginning of the experiment, we must create a pseudo-pure state from the thermal equilibrium state. The thermal equilibrium density operator for three spins (homonuclear) in the high temperature limit, given by:

$$\rho_{eq} \approx \frac{I}{2^3} + \frac{\hbar\beta}{2^3} \sum_{k=1}^3 \omega_k I_z^k = \frac{I}{8} + \frac{\hbar\beta\omega_F}{8} [I_z^1 + I_z^2 + I_z^3], \quad (6.34)$$

using the techniques described in chapter (2), can be transformed into a pseudo-pure ground state:

$$\rho = \frac{1-\epsilon}{8} I + \epsilon |000\rangle\langle 000|, \quad (6.35)$$

where $\omega_F = \gamma_F B_0$, $\beta = 1/k_B T$ is the Boltzmann factor, ω_k are their chemical shifts, I is the 8×8 identity matrix, I_z^k is the z component of the nuclear spin angular momentum operator for the k th spin and $\epsilon = \hbar\omega_k\beta \simeq 10^{-5}$ describes the thermal polarization of the system at room temperature (see chapter (2)). The spectrum for the system at thermal equilibrium state is shown in Fig. (6.7). In this experiment, qubit 2 is important and the results are shown just for qubit 2. The thermal equilibrium spectra of the fluorine just

for qubit 2 is shown in Fig. (6.8).

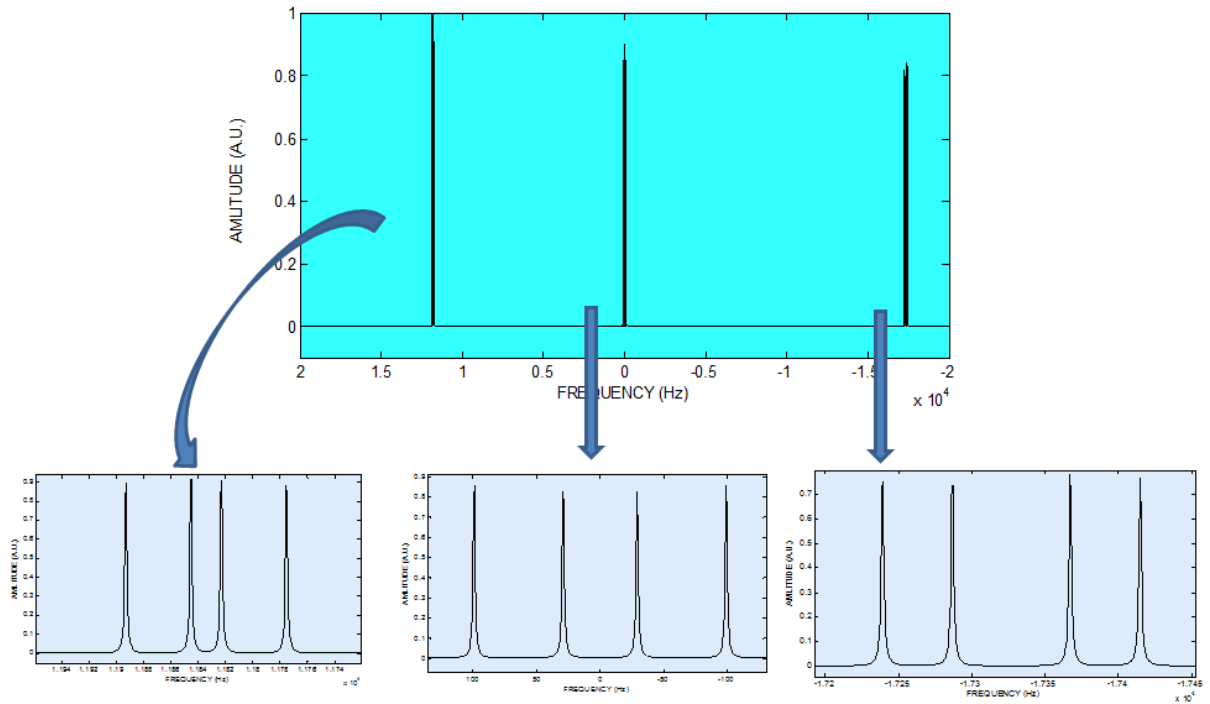


Fig. 6.7: The fluorine spectrum of the system, obtained by applying selective readout pulses to the system in its thermal equilibrium state.

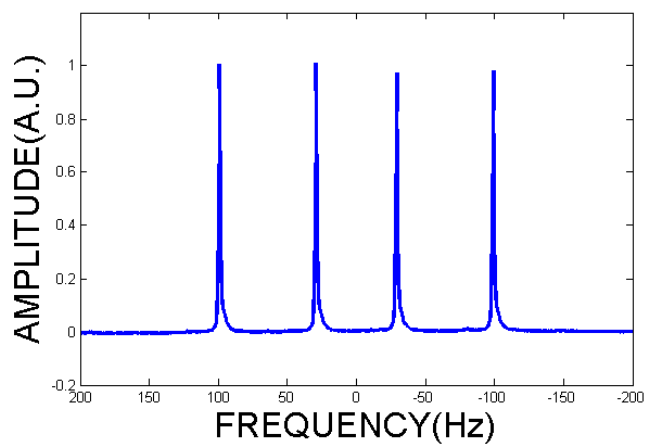


Fig. 6.8: The fluorine spectrum of second qubit, obtained by applying selective readout pulse to the system in its thermal equilibrium state.

We have used spatial averaging for preparation pseudo-pure state (see chapter (2)). So the spin system is initialized in the pseudo-pure state $|\psi_0\rangle = |000\rangle$ (see Fig. (6.11)). We have used two different pulse sequences to prepare the pseudo-pure state. In the first and second experiments, we have used the same pulse sequence to prepare pseudo-pure state and the pulse sequence for preparation the pseudo-pure state is given in Fig. (6.9).

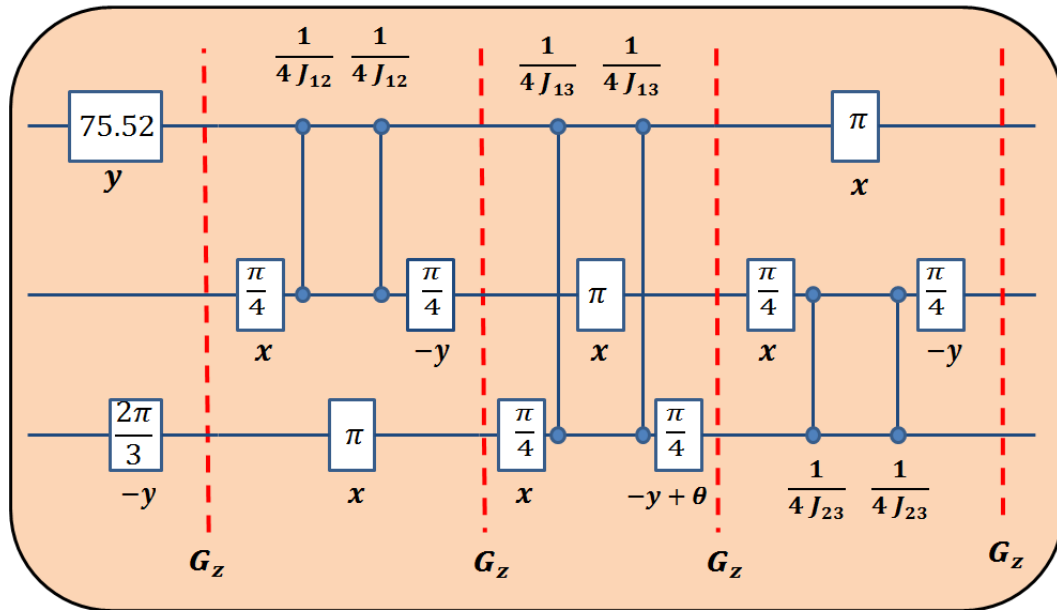


Fig. 6.9: The pulse sequence for preparation pseudo-pure state in the first and second experiments. G_z is the magnetic field gradient in the z direction. The pulse sequence does include the refocusing π pulses.

In the third experiment, the pulse sequence for preparation of the pseudo-pure state was different; we used the Controlled-transfer gates which is described in [66] (see chapter (2)). The quantum circuit for preparation of the pseudo-pure state is realized by shaped pulses, free evolution and magnetic field gradient in the z direction. When we use this method for preparation pseudo-pure state, we will obtain better results. The pulse sequence is depicted in Fig. (6.10) and the spectrum for the system (just for second qubit (F_2)) at pseudo-pure state is shown in Fig. (6.11).

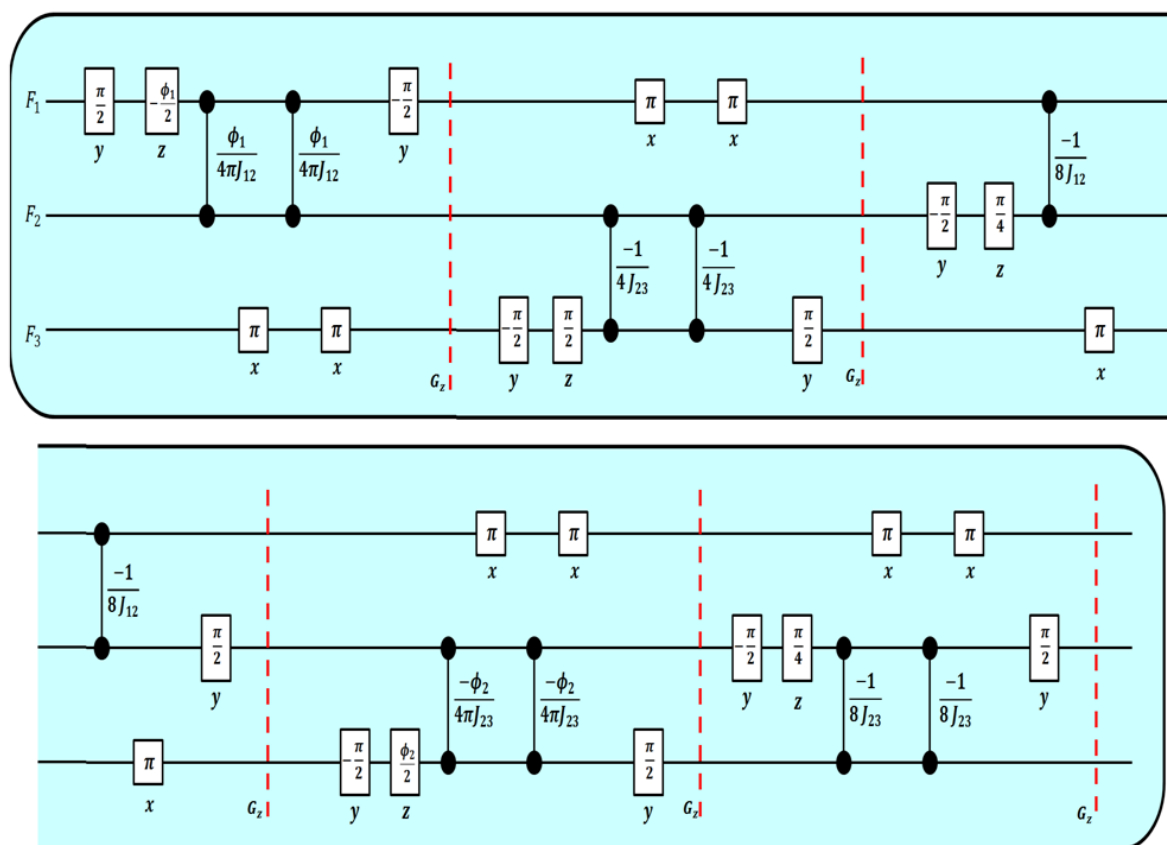


Fig. 6.10: The pulse sequence for preparation the pseudo-pure state, where $\phi_1 = 98.2^\circ$, $\phi_2 = 135.6^\circ$ and G_z is the magnetic field gradient in the z direction. The pulse sequence includes the refocusing π pulses.

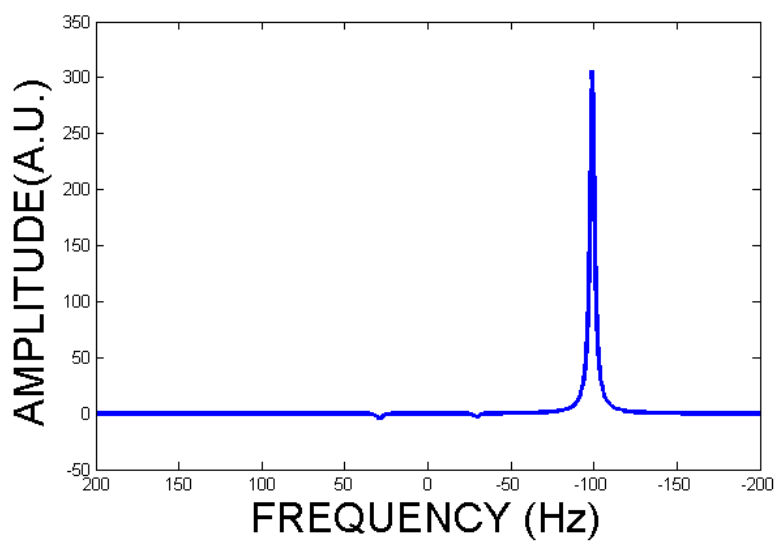


Fig. 6.11: Pseudo-pure spectrum of iodotrifluoroethylene for second qubit.

After the initialization in the pseudo-pure state, the 2D YBE circuit is applied to qubits one and three but before applying the 2D YBE, qubits one and three must be in the superposition of the states ($|\psi\rangle = \frac{1}{\sqrt{2}}(|0\rangle + |1\rangle)$). For this reason, the 90° pulse about y axis is applied on qubits one and three. After preparing the superposition of the states on qubits one and three, operations corresponding to the Left-Hand-Side and the Right-Hand-Side of the 2D YBE are applied on qubits one and three, respectively. The quantum circuit diagram for preparation of the superposition states and the Left-Hand-Side and Right-Hand-Side of the 2D YBE on the first and third qubits (first step) is shown in Fig. (6.12).

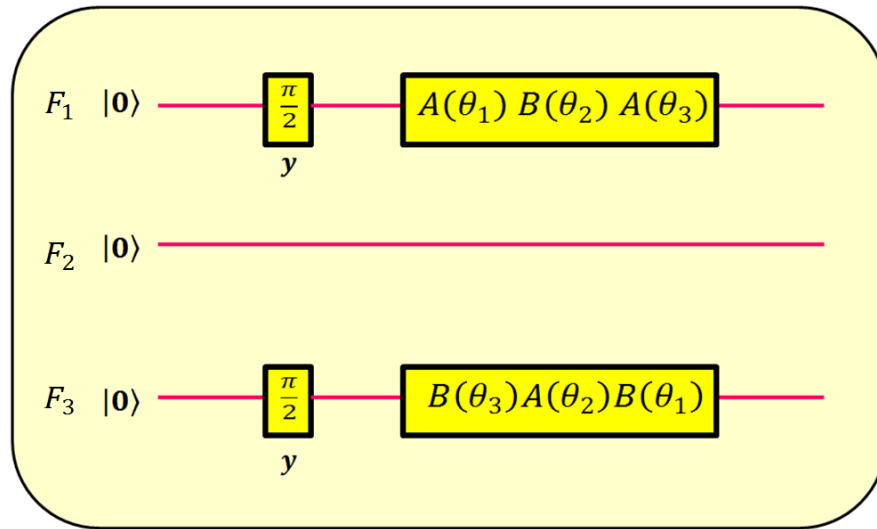


Fig. 6.12: The quantum circuit diagram for first step of the 2D YBE experiment.

In the final step, the Hadamard gate is applied to qubit two and then a Controlled-Swap gate with the second qubit as control is applied [102]. The total quantum circuit diagram for implementation of the 2D YBE is shown in Fig. (6.13).

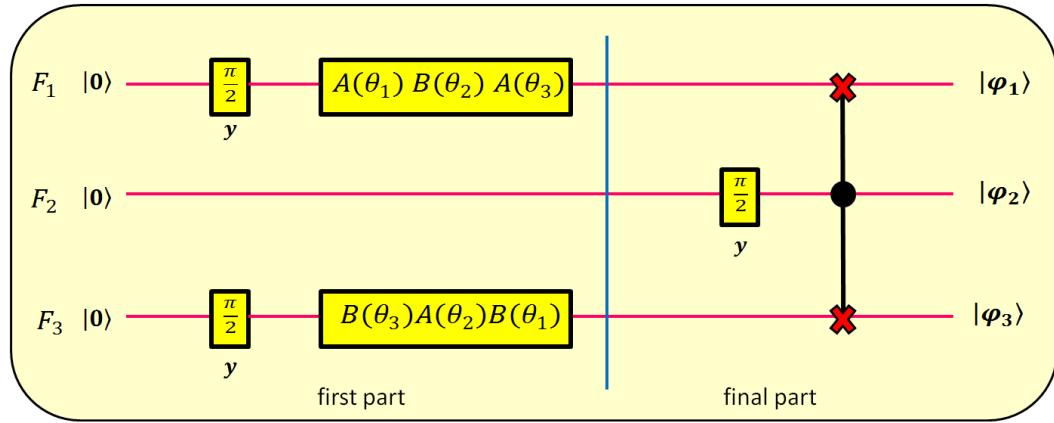


Fig. 6.13: The total quantum circuit diagram for implementation of the 2D YBE. F_1 , F_2 and F_3 are denoted as qubit 1, qubit 2 and qubit 3, respectively. The first part is separated from the final part by the blue line.

By substituting Eqs. (6.32) and (6.33) into the first part of the quantum circuit in Fig. (6.13) which are related to the Left-Hand-side and the Right-Hand-Side of the 2D YBE and doing some calculation and simplification, then the first part of the quantum circuit in Fig. (6.13) can be changed to the the quantum circuit in Fig. (6.14).

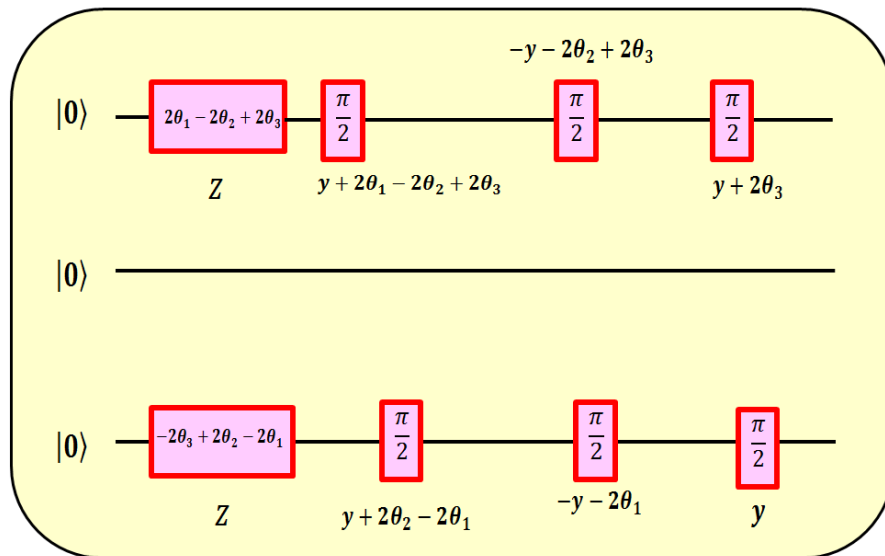


Fig. 6.14: The first part of the quantum circuit after simplification.

The Controlled-Swap gate in the final part can be obtained by applying two Controlled-NOT(CNOT) gates and one Toffoli gate as shown in Fig. (6.15).

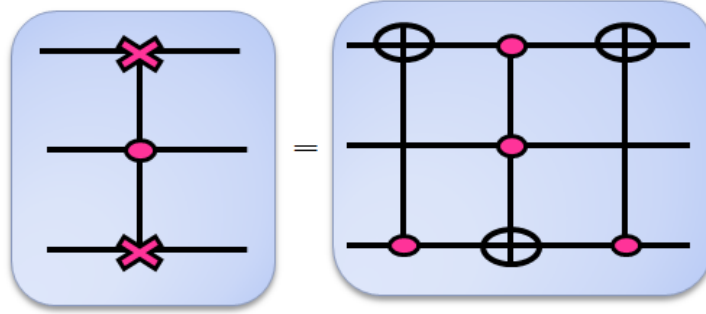


Fig. 6.15: Schematic of the Controlled-Swap gate logic circuit.

The final part of the quantum circuit diagram for implementation of the 2D YBE (Hadamard gate on second qubit and Controlled-Swap gate with second qubit as control) is shown in Fig. (6.16).

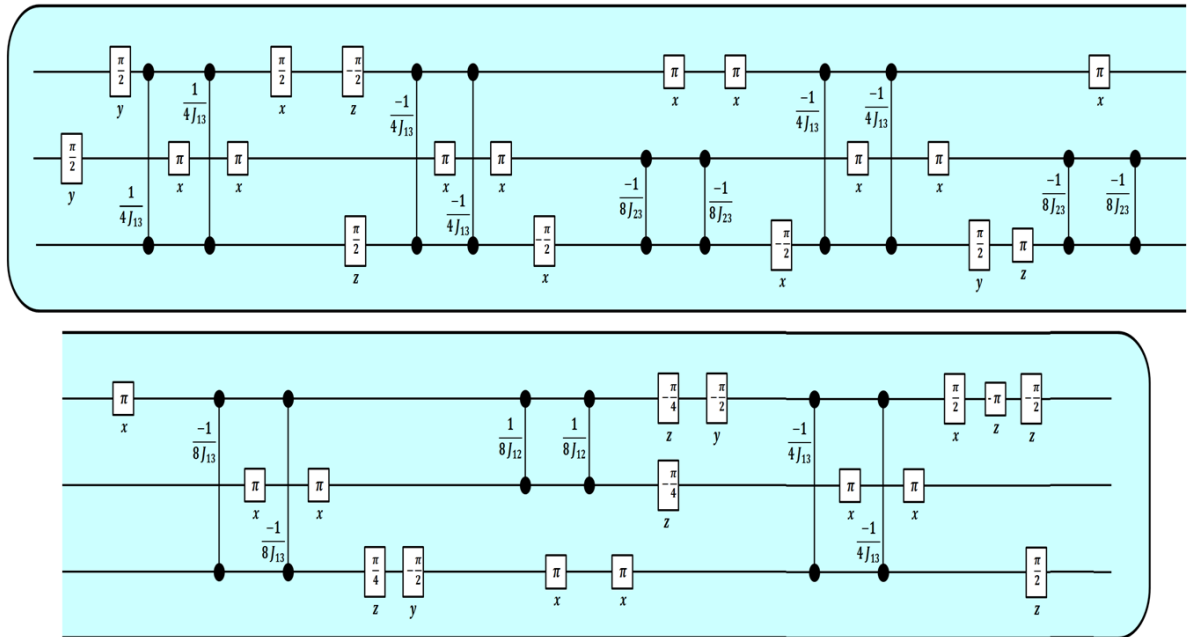


Fig. 6.16: The quantum circuit diagram for the final step of the 2D YBE experiment (it consists Hadamard gate on second qubit and Controlled-Swap gate with second qubit as control). The pulse sequence includes the refocusing π pulses.

In the final step, after applying the Hadamard gate on second qubit and the Controlled-Swap gate with the second qubit as control and when we measure qubit 2, the total magnetization of qubit 2 must be a product of the other two states ($\langle \sigma_x^2 + i\sigma_y^2 \rangle = \text{Tr}(\rho_1\rho_3)$) where $\rho_1 = |\varphi_1\rangle\langle\varphi_1|$ and $\rho_3 = |\varphi_3\rangle\langle\varphi_3|$ (see Fig. (6.13))[102]. In the first part, the 2D YBE is applied on qubits 1 and 3, it means that the states of qubit 1 and 3 must be the same as each other ($\rho_1 = \rho_3 = \rho$). Therefore the total magnetization of qubit 2 would be $\langle \sigma_x^2 + i\sigma_y^2 \rangle = \text{Tr}(\rho^2) \cong 1$ when the angle parameters (θ_1, θ_2 and θ_3) satisfy the relation in Eq. (6.11).

In the Fig. (6.14) (first part of the 2D YBE circuit), there are three angles (θ_1, θ_2 and θ_3) and the experiment is done for two different choices of these three angles, which we will call correct angles and wrong angles. Correct angles mean that the angle parameters (θ_1, θ_2 and θ_3) satisfy the relation in Eq. (6.11), whereas the wrong angles do not. First, we consider correct angles. In Fig. (6.14), $\theta_1 = -\theta_3$ and $\theta_2 = 0$ are chosen. So, the first part of the quantum circuit diagram for implementation of the 2D YBE is changed as in Fig. (6.17).

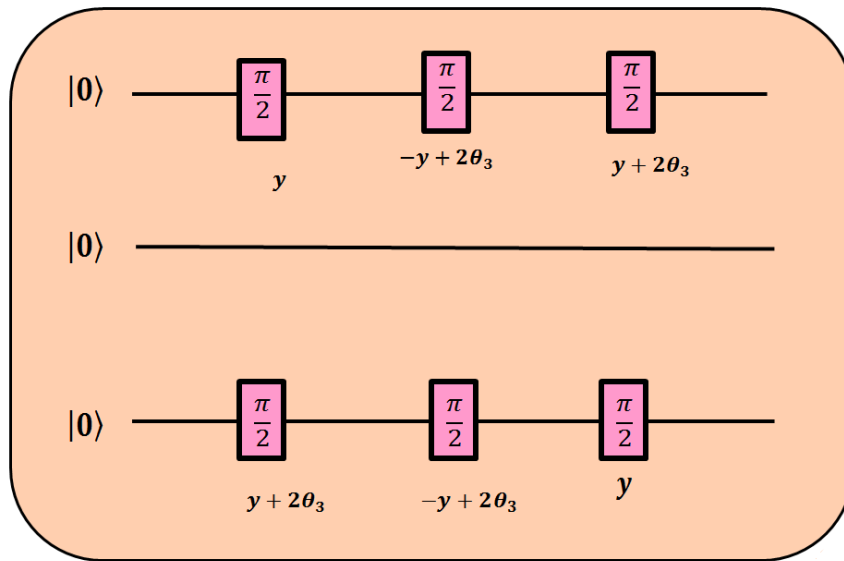


Fig. 6.17: The first part of the quantum circuit in Fig. (6.14) when $\theta_1 = -\theta_3$, $\theta_2 = 0$ and θ_3 varies between 0 and 2π .

The total magnetization of qubit 2 is shown in Fig. (6.18) when $\theta_1 = -\theta_3$, $\theta_2 = 0$ and θ_3 varies between 0 and 2π . The results are very close to 1 when the angle parameters satisfy the relation in Eq. (6.11). For the normalization, we have used the fluorine spectrum at pseudo-pure state as reference.

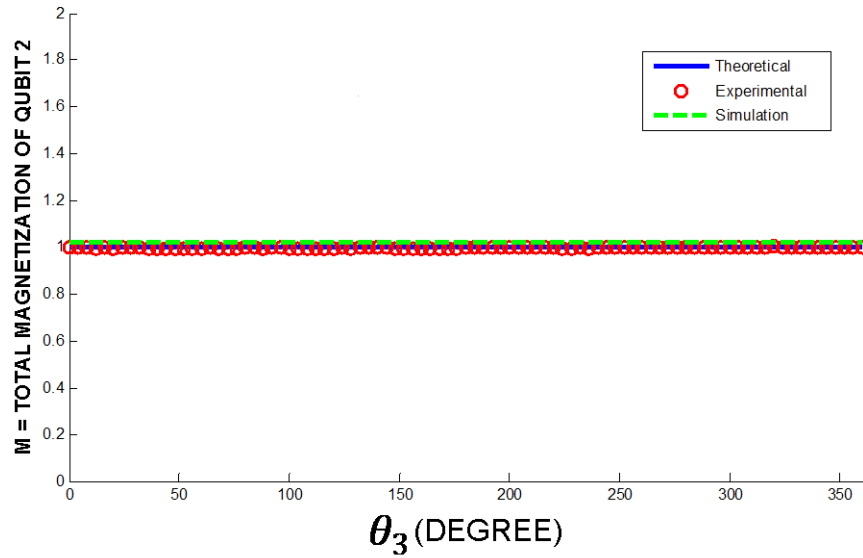


Fig. 6.18: The total magnetization of qubit 2 when $\theta_1 = -\theta_3$, $\theta_2 = 0$ and θ_3 varies between 0 and 2π . The blue line is theoretical, the green dashed line is simulation and the red circles are experimental.

The histogram in Fig. (6.19) shows the distribution of the total magnetizations of qubit 2. From this diagram, we see that the magnetization of qubit 2 is 0.998 ± 0.001 .

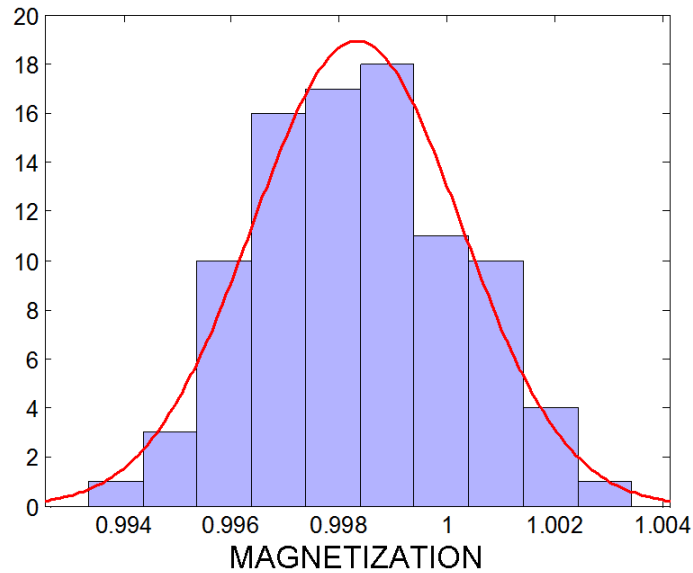


Fig. 6.19: The histogram of the experimental data when $\theta_1 = -\theta_3$, $\theta_2 = 0$ and θ_3 varies between 0 and 2π .

In Fig. (6.20), we show the results of implementation of the 2D YBE for three times when $\theta_1 = -\theta_3$, $\theta_2 = 0$ and θ_3 varies between 0 and 2π .

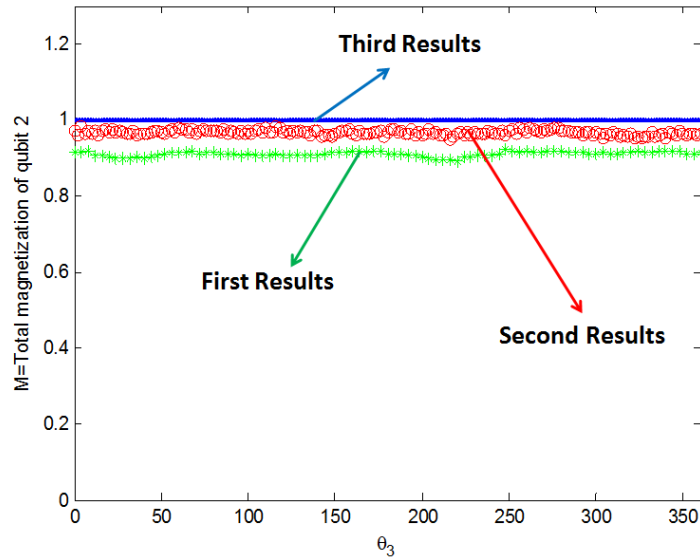


Fig. 6.20: Comparison between the three times of implementation 2D YBE for correct angles when $\theta_1 = -\theta_3$, $\theta_2 = 0$ and θ_3 varies between 0 and 2π .

Now, let us consider the wrong angle case. The experiment has been done for three different values of θ_1 , θ_2 and θ_3 when these angles do not satisfy the relation in Eq. (6.11). First, $\theta_2 = \theta_3 = 0$ and θ_1 varies between 0 and 2π , these angle parameters do not satisfy the relation in Eq. (6.11) except for $\theta_1 = 0, \pi, 2\pi$ (these three angle parameters satisfy the relation in Eq. (6.11) and the total magnetization of qubit 2 is one). Therefore, the first part of the quantum circuit diagram for implementation of the 2D YBE is changed as in Fig. (6.21).

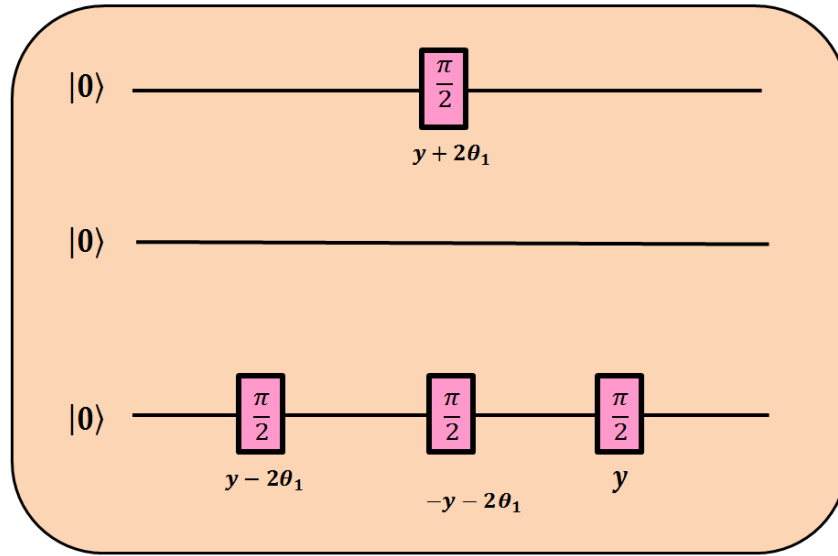


Fig. 6.21: The first part of the quantum circuit in Fig. (6.14) when $\theta_2 = \theta_3 = 0$ and θ_1 varies between 0 and 2π .

The total magnetizations of qubit 2 for these angle parameters are measured and the total magnetization of qubit 2 must be less than one except when $\theta_1 = 0, \pi, 2\pi$. The total magnetization of qubit 2 is shown in Fig. (6.22) when $\theta_2 = \theta_3 = 0$ and θ_1 varies between 0 and 2π . It is clear that, when the angle parameters do not satisfy the relation in Eq. (6.11), the total magnetization of qubit 2 is less than one.

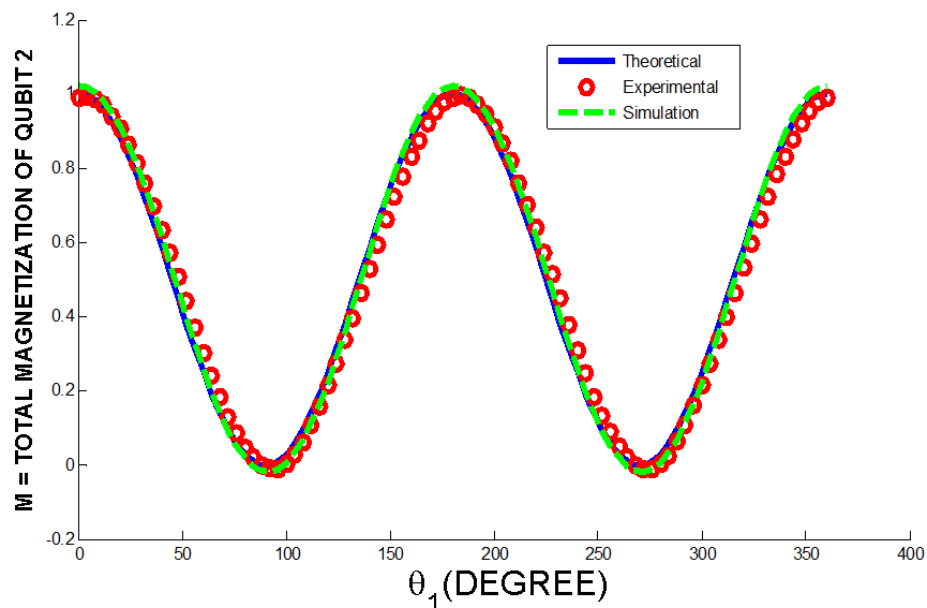


Fig. 6.22: The total magnetization of qubit 2 when $\theta_2 = \theta_3 = 0$ and θ_1 varies between 0 and 2π . The blue line is theoretical, the green dashed line is simulation and the red circles are experimental. For the wrong angles, the total magnetization of qubit 2 is less than one and for the correct angles, the total magnetization of qubit 2 is one.

We have also implemented 2D YBE for this wrong angles three times. The results of implementation 2D YBE for three times when $\theta_2 = \theta_3 = 0$ and θ_1 varies between 0 and 2π , are shown in Fig. (6.23).

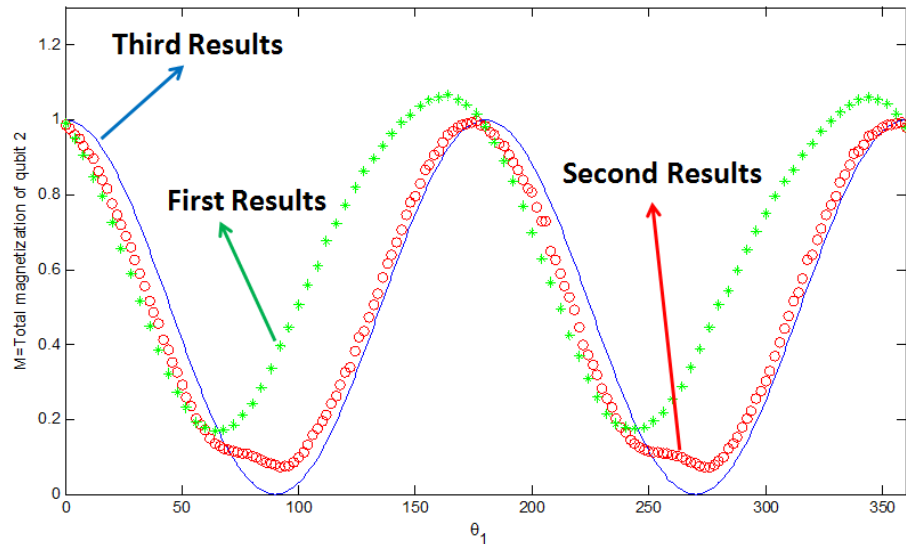


Fig. 6.23: Comparison between the three times of implementation 2D YBE for wrong angles when $\theta_2 = \theta_3 = 0$ and θ_1 varies between 0 and 2π .

Second, $\theta_1 = \frac{\pi}{2}$ and $\theta_3 = \frac{\pi}{4}$ are chosen and θ_2 varies between 0 and 2π . When θ_2 varies between 0 and 2π except for $\theta_2 = \frac{\pi}{4}, \frac{5\pi}{4}$ (these two angle parameters satisfy the relation in Eq. (6.11) and the total magnetization of qubit 2 is one), the angle parameters (θ_1, θ_2 and θ_3) do not satisfy the relation in Eq. (6.11) and the total magnetization of qubit 2 is less than one. Therefore, the first part of the quantum circuit diagram for implementation of 2D YBE is changed as in Fig. (6.24).

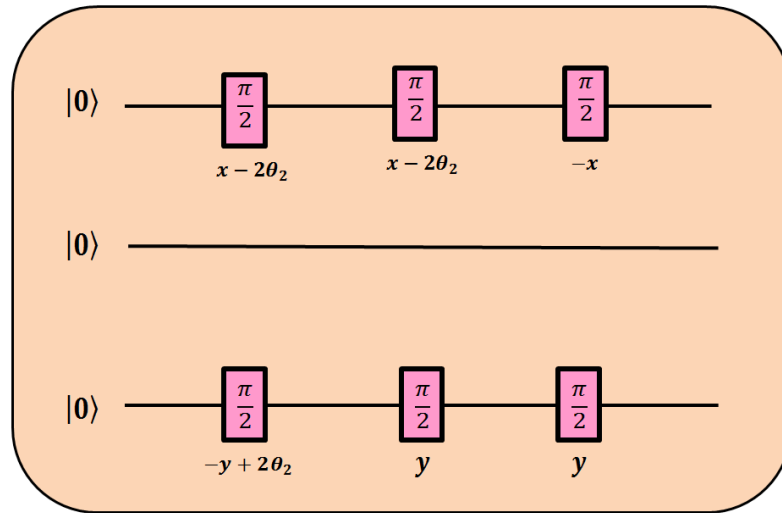


Fig. 6.24: The first part of the quantum circuit in Fig. (6.14) when $\theta_1 = \frac{\pi}{2}$, $\theta_3 = \frac{\pi}{4}$ and θ_2 varies between 0 and 2π .

The total magnetization of qubit 2 is shown in Fig. (6.25) when $\theta_1 = \frac{\pi}{2}$, $\theta_3 = \frac{\pi}{4}$ and θ_2 varies between 0 and 2π . It is clear that, when the angle parameters do not satisfy the relation in Eq. (6.11), the total magnetization of qubit 2 is less than one.

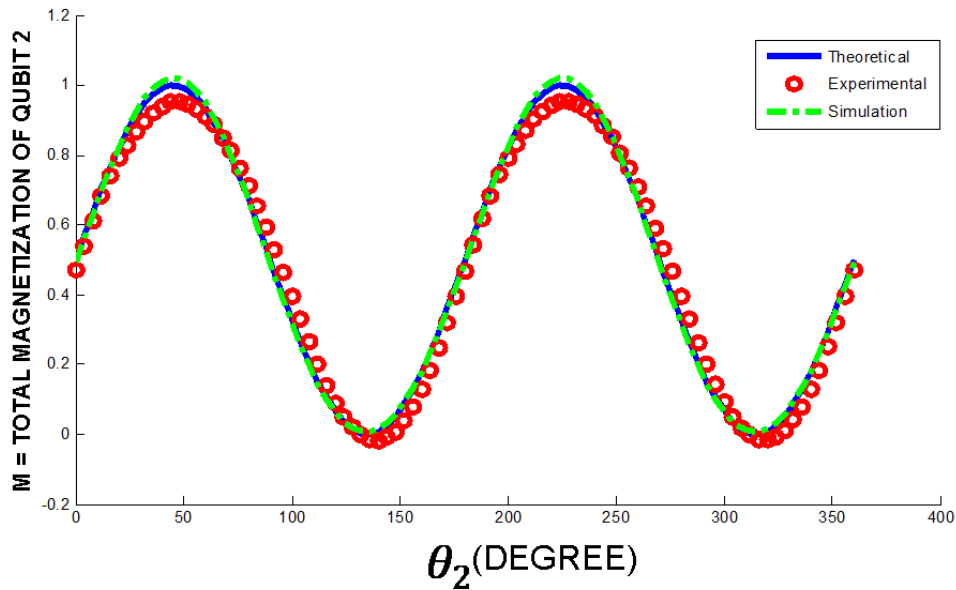


Fig. 6.25: The total magnetization of qubit 2 when $\theta_1 = \frac{\pi}{2}$, $\theta_3 = \frac{\pi}{4}$ and θ_2 varies between 0 and 2π . The blue line is theoretical, the green dashed line is simulation and the red circles are experimental. For the wrong angles, the total magnetization of qubit 2 is less than one.

Third, $\theta_1 = 2\theta_2$ and $\theta_3 = \frac{\pi}{2}$ are chosen and θ_1 varies between 0 and 2π . When θ_1 varies between 0 and 2π except for $\theta_1 = \frac{\pi}{3}, \pi, \frac{5\pi}{3}$ (these three angle parameters satisfy the relation in Eq. (6.11) and the total magnetization of qubit 2 is one), the angle parameters (θ_1, θ_2 and θ_3) do not satisfy the relation in Eq. (6.11) and the total magnetization of qubit 2 is less than one. When θ_1 and θ_3 are equal to $2\theta_2$ and $\frac{\pi}{2}$ respectively, the first part of the quantum circuit diagram for implementation of 2D YBE is changed as Fig. (6.26).

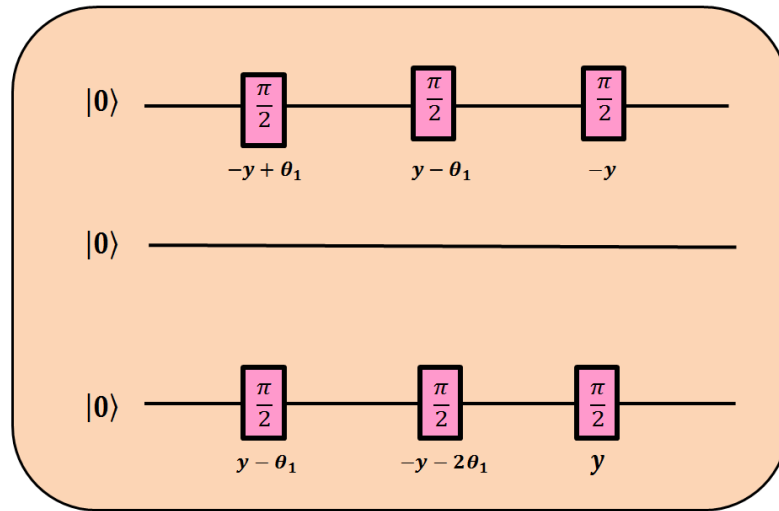


Fig. 6.26: The first part of the quantum circuit in Fig. (6.14) when $\theta_1 = 2\theta_2$, $\theta_3 = \frac{\pi}{2}$ and θ_1 varies between 0 and 2π .

The total magnetization of qubit 2 is shown in Fig. (6.27) when $\theta_1 = 2\theta_2$, $\theta_3 = \frac{\pi}{2}$ and θ_1 varies between 0 and 2π . It is clear that, when the angle parameters do not satisfy the relation in Eq. (6.11), the total magnetization of qubit 2 is less than one. The results are shown when the angle parameters change a little, the total magnetization of qubit 2 changes, as well.

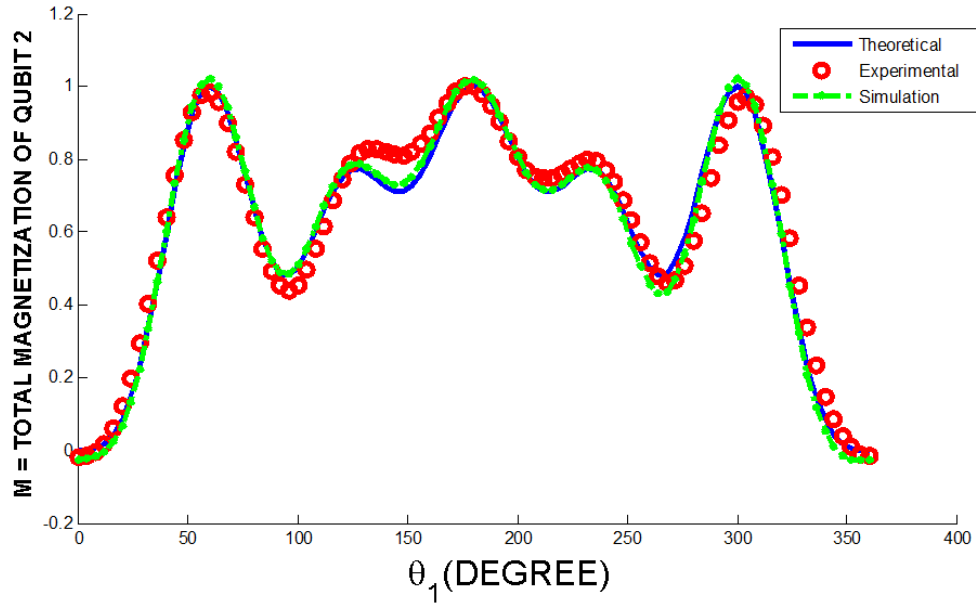


Fig. 6.27: The total magnetization of qubit 2 when $\theta_1 = 2\theta_2$, $\theta_3 = \frac{\pi}{2}$ and θ_1 varies between 0 and 2π . The blue line is theoretical, the green dashed line is simulation and the red circles are experimental. For the wrong angles, the total magnetization of qubit 2 is less than one.

The experiment in Fig. (6.27) did run for 13 times. Then the results are compared with each other in Fig. (6.28). It is clear that, the results are very close to each other.

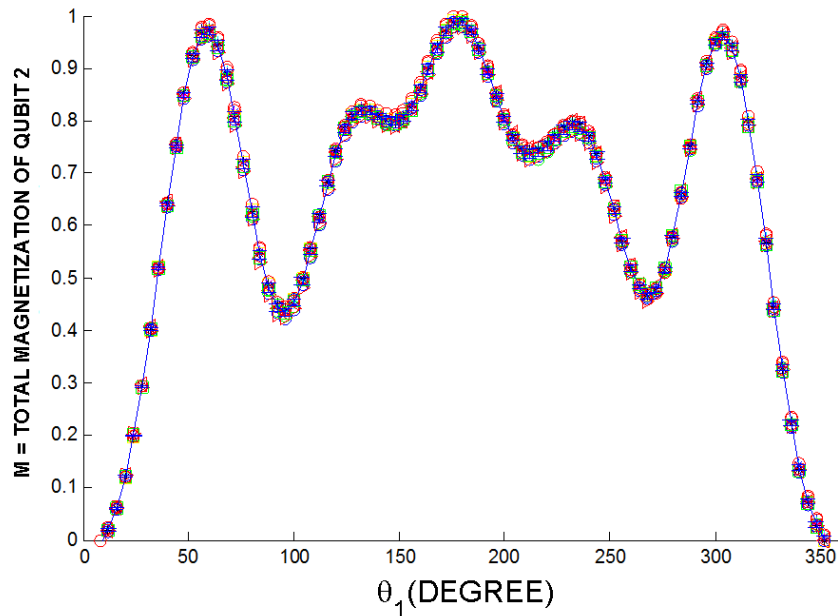


Fig. 6.28: The comparison between 13 times repeat the experiment in Fig. (6.26) with errorbar, when $\theta_1 = 2\theta_2$, $\theta_3 = \frac{\pi}{2}$ and θ_1 varies between 0 and 2π .

7

Conclusions

In this thesis, we first reviewed NMR and QIP fundamentals. Then, we presented an optimal control algorithm and explained each step of this algorithm. For computing gradients, there are several methods such as: exact methods using the eigendecomposition, finite differences, series expansions, and the standard method. For computing the control vector update, the second-order BFGS method, the first-order steepest ascent and the conjugate gradient methods can be used. The rest of the thesis consisted of two distinct works.

In the first work of this thesis, we performed Quantum State Tomography (QST) in a two and three qubits systems consisting of strongly coupled nuclear spins, known in the NMR literature as “*AB*” and “*ABX*” systems, respectively.

Quantum state tomography (QST) is commonly employed in many different NMR systems, such as quadrupolar nuclei or weakly and strongly coupled spin- $\frac{1}{2}$ systems, to characterize the results of quantum information processing experiments. The main idea of QST consists of expanding the density matrix in a set of basis operators. The connection between the theory and experiment is made by deriving relations between the

observed amplitudes in the NMR signal and the coefficients of the expansion (e.g., Eq. (5.1) in chapter (5)). Analytical solutions, for such relation, for weakly coupled system are found in Ref. [25]. Strongly coupled systems contain second order transitions, not present in weakly coupled ones, which can produce quite complex NMR spectra. In the present thesis, we have found analytical solutions for “*AB*” and “*ABX*” systems, we have shown that the number of experiments needed to implement QST in “*ABX*” systems can be reduced with respect to three weakly coupled spins, and therefore decreasing the experimental effort required for complete density matrix reconstruction. To exemplify, the quantum state tomography is performed in different steps of the full quantum teleportation protocol. Because, the correct form of the Hamiltonian for strongly coupled systems is considered, as well in the optimization of quantum gates, the results are obtained with high fidelity.

For QST, the reduction in the number of experiments is due to the fact that the NMR signal of strongly coupled systems can contain lines related to second-order transitions not observed in weakly coupled systems. Therefore a single second-order spectrum can contain more information about the quantum state of the spin system than the first-order spectrum. This additional information can be used to reduce the total number of experiments to perform QST. It may be possible to find analytical solutions for other types of strongly coupled systems, with more qubits, but certainly not all of them. In cases where analytical solutions are not possible we should use numerical methods for deriving such relations. However, it is not the purpose of this thesis to cover all possible strongly coupled systems.

We tried to have a more accurate study of the teleportation, by applying a set of pulses generated by the Gradient Ascent Pulse Engineering (GRAPE) algorithm on a spatially averaged pseudo-pure state of three-qubit. Our implementation of teleportation is performed using liquid state NMR quantum information processor and a Varian 500-MHz spectrometer for the control and acquisition, applied to an ensemble of molecules of labeled trichloroethylene. To perform teleportation we made use of the Hydrogen nu-

cleus (H), and the two Carbon 13 nuclei (C1 and C2), teleporting the state of C1 to H. Spectra from simulation are compared to experimental spectra for both of them (Carbon and Hydrogen). The sample we have used for teleportation is an “*ABX*” spin system in NMR technology because of the strong coupling between carbons. The Hamiltonian of this sample is not diagonal and it is very complicated for doing tomography. For this reason we diagonalized the Hamiltonian at the first, then we continued the research as described in the context. Quantum teleportation is theoretically perfect, yielding an output state which equals the input with a fidelity $F=1$. In practice fidelities less than one are realized due to imperfections in the EPR pair, Alice’s bell measurement, Bob’s unitary transformation, and etc. In this method which we obtained in chapters (4) and (5), any given coefficient in a product operator expansion of the density matrix can be obtained from a fit to a single spectra multiplet. Exploring both theoretically and experimentally of the real part of the reconstructed density matrices of four states shows that the method which is described in this thesis, enjoys great preciseness.

The second work of this thesis is a study on the Yang-Baxter Equation in two-dimensional. The Yang-Baxter Equation is directly verified experimentally using Nuclear Magnetic Resonance for the first time. The experiment proved the equality between the two sides of the Yang-Baxter Equation if the parameters θ_1 , θ_2 and θ_3 satisfy Eq. (6.11). It means that the validity of Yang-Baxter equation is guaranteed sufficiently when the angle parameters satisfy the relation in Eq. (6.11). It is also the necessary condition for the validity of the Yang-Baxter equation to make the angle parameters satisfy that relation. The Yang-Baxter Equation provides a sufficient condition for the prediction of the spectrum.

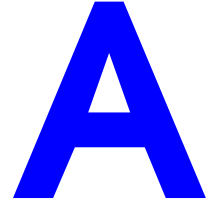
For implementation of the 2D YBE, we have used liquid state nuclear magnetic resonance, applied to an ensemble of molecule of labeled Iodotrifluoroethylene. This molecule consists of three qubits, F_1 , F_2 and F_3 . There are three angles (θ_1 , θ_2 and θ_3) in the Yang-Baxter Equation and the experiment is done for two different choices of these three

angles, correct angles and wrong angles. we have shown the results for correct angles and wrong angles. The results showed, when the angle parameters satisfy the relation in Eq. (6.11) (correct angles), the total magnetization of qubit 2 is 1 but when we have wrong angles, the total magnetization of qubit 2 is less than 1. The results are shown that when the angle parameters change a little the total magnetization of qubit 2 changes as well.

One important issue for higher dimensional is the role of entanglement in the Yang-Baxter Equation. In higher dimensions, the operations in the Yang-Baxter Equation will inevitably bring in quantum entanglement. It will be an interesting and significant subject for future study, and consequently the entangling power of the operations in the Yang-Baxter Equation, namely the operations in either sides of the Yang-Baxter Equation emerge naturally also an important topic. In higher dimensions, the operations will be more complex and entanglement also comes into play.

Discovered from solving problems in many-body systems and statistical models in the middle of the last century, variety of contexts of the Yang-Baxter Equation were revealed and it has been applied to many different area, such as quantum field theory, statistical mechanics, group theory, and etc. Now, the Yang-Baxter Equation is playing an important role in quantum information science which is a thriving area of frontier research. Using the relation between Bell basis and the Yang-Baxter Equation enables the investigation of quantum entanglement, and the relation between anyon and the Yang-Baxter Equation entails exploring topological quantum computing. Many interesting applications of the Yang-Baxter Equation lies ahead.

APPENDIX



Unitary Transformation

Let's suppose that we have the matrix equation:

$$\hat{A}x = \lambda x, \tag{A.1}$$

or:

$$\hat{A}x - \lambda x = \hat{0}. \tag{A.2}$$

Then which can be written as:

$$(\hat{A} - \lambda \hat{1})x = \hat{0}. \tag{A.3}$$

This is called the characteristic equation. The λ 's are the eigenvalues and x is the eigenvector or more properly, the right eigenvector. If:

$$\hat{A}^T x = \lambda x, \tag{A.4}$$

then:

$$\lambda x^T = (\lambda x)^T = (\hat{A}^T x)^T = x^T \hat{A}, \tag{A.5}$$

where x is now referred to as the left eigenvector. There will be non-trivial solutions for the characteristic equation only if:

$$\det(\hat{A} - \lambda \hat{1}) = 0, \quad (\text{A.6})$$

or:

$$\det \begin{pmatrix} a_{11} - \lambda & a_{12} & a_{13} & \dots \\ a_{21} & a_{22} - \lambda & a_{23} & \dots \\ a_{31} & a_{32} & \ddots & \dots \\ \dots & \dots & \dots & a_{nn} - \lambda \end{pmatrix} = 0, \quad (\text{A.7})$$

which will yield to a polynomial known as the characteristic polynomial.

SECTION: A.1

Transforms

Two $n \times n$ matrices \hat{A} and \hat{B} are said to be similar matrices if there exists an invertible $n \times n$ matrix, \hat{T} such that:

$$\hat{B} = \hat{T}^{-1} \hat{A} \hat{T}, \quad (\text{A.8})$$

and the transformation from \hat{A} and \hat{B} is called a similarity transform. We can back-transform \hat{B} to \hat{A} again:

$$\hat{T} \hat{B} \hat{T}^{-1} = \hat{T} \hat{T}^{-1} \hat{A} \hat{T} \hat{T}^{-1} = \hat{A}. \quad (\text{A.9})$$

Note that reversing the order of the \hat{T} matrices gives a different matrix, \hat{C} , but is still, of course, a similarity transformation:

$$\hat{C} = \hat{T} \hat{A} \hat{T}^{-1}. \quad (\text{A.10})$$

Note, also, that \hat{C} is similar to \hat{A} and to \hat{B} :

$$\hat{C} = \hat{T}\hat{A}\hat{T}^{-1}, \quad (\text{A.11})$$

$$\hat{A} = \hat{T}^{-1}\hat{T}\hat{A}\hat{T}^{-1}\hat{T} = \hat{T}^{-1}\hat{C}\hat{T}, \quad (\text{A.12})$$

$$\hat{B} = \hat{T}^{-1}\hat{A}\hat{T} = \hat{T}^{-1}\hat{T}^{-1}\hat{C}\hat{T}\hat{T} = (\hat{T}^{-1})^2\hat{C}(\hat{T})^2. \quad (\text{A.13})$$

The reason that \hat{A} and \hat{B} (and \hat{C}) are called similar is that they have several properties in common. First, the determinants of \hat{A} and \hat{B} are the same:

$$\hat{B} = \hat{T}^{-1}\hat{A}\hat{T}, \quad (\text{A.14})$$

$$\det\hat{B} = \det(\hat{T}^{-1}\hat{A}\hat{T}) = \det\hat{T}^{-1} \det\hat{A} \det\hat{T} = \det\hat{A}. \quad (\text{A.15})$$

Next, the trace of \hat{A} and \hat{B} are equal:

$$\hat{B} = \hat{T}^{-1}\hat{A}\hat{T}, \quad (\text{A.16})$$

$$\text{Tr}(\hat{B}) = \text{Tr}(\hat{T}^{-1}\hat{A}\hat{T}) = \text{Tr}(\hat{T}\hat{T}^{-1}\hat{A}) = \text{Tr}(\hat{A}) = \text{Tr}(\hat{A}). \quad (\text{A.17})$$

Two matrices related by a similarity transformation have the same eigenvalues. If we have matrices \hat{A} and \hat{B} related by a similarity transformation and eigenvector matrix \hat{X} then:

$$\hat{B} = \hat{T}\hat{A}\hat{T}^{-1}, \quad (\text{A.18})$$

$$\hat{A}\hat{X} = \lambda\hat{X}. \quad (\text{A.19})$$

Now, using the transformation matrix \hat{T} , we write:

$$\hat{B}\hat{T}\hat{X} = (\hat{T}\hat{A}\hat{T}^{-1})\hat{T}\hat{X} = \hat{T}(\hat{A}\hat{X}) = \hat{T}(\lambda\hat{X}) = \lambda\hat{T}\hat{X}. \quad (\text{A.20})$$

Thus, if \hat{X} is an eigenvector matrix of \hat{A} then $\hat{T}\hat{X}$ is an eigenvector of \hat{B} and \hat{B} has the same eigenvalues as \hat{A} .

From a practical point of view, the order in which the (left-to-right) multiplication of the matrices is done is irrelevant. That is, for the similarity transform:

$$\hat{B} = \hat{T}^{-1} \hat{A} \hat{T}. \quad (\text{A.21})$$

If we make the definitions:

$$\hat{X} = \hat{T}^{-1} \hat{A}, \quad (\text{A.22})$$

and

$$\hat{Y} = \hat{A} \hat{T}. \quad (\text{A.23})$$

Then we can write our similarity transform in two equivalent ways:

$$\hat{B} = \hat{X} \hat{T}, \quad (\text{A.24})$$

or:

$$\hat{B} = \hat{T}^{-1} \hat{Y}. \quad (\text{A.25})$$

Each representing a different order of multiplication of matrices \hat{T}^{-1} , \hat{A} and \hat{T} .

Another type of transform is the orthogonal transformation which uses the transpose matrix:

$$\hat{B} = \hat{T}^T \hat{A} \hat{T}. \quad (\text{A.26})$$

This only works however, if:

$$\hat{T}^T = \hat{T}^{-1}, \quad (\text{A.27})$$

and, this being the case, all of the properties of the similar matrices discussed above apply here as well.

The last type of transformation that we shall be interested in, is the unitary transformation:

$$\hat{B} = (\hat{T}^*)^T \hat{A} \hat{T}, \quad (\text{A.28})$$

where:

$$(\hat{T}^*)^T = \hat{T}^{-1}. \quad (\text{A.29})$$

In other words, the matrix \hat{T} is unitary, if all the elements of \hat{T} are real then it is also orthogonal. The determinant, trace and eigenvalues of the transformed matrix are invariant under the transformation.

Very closely related to the unitary transformation is the hermitian transformation:

$$\hat{B} = (\hat{T}^*)^T \hat{A} \hat{T}^{-1}, \quad (\text{A.30})$$

where now:

$$(\hat{T}^*)^T = \hat{T}. \quad (\text{A.31})$$

We can use these ideas in our investigation of eigenvalue equations.

If \hat{A} is hermitian then the matrices that diagonalize it will be unitary. An example of a unitary matrix is:

$$\hat{T} = \begin{bmatrix} \cos \theta & \sin \theta \\ -\sin \theta & \cos \theta \end{bmatrix}, \quad (\text{A.32})$$

$$(\hat{T}^*)^T = \begin{bmatrix} \cos \theta & -\sin \theta \\ \sin \theta & \cos \theta \end{bmatrix}. \quad (\text{A.33})$$

Simple multiplication will confirm that

$$\hat{T}(\hat{T}^*)^T = \hat{1}. \quad (\text{A.34})$$

According to this relation:

$$\hat{B} = \hat{T}^{-1} \hat{A} \hat{T}, \quad (\text{A.35})$$

we have:

$$H = \hat{X} H_{diag} \hat{X}^{-1}, \quad (\text{A.36})$$

or:

$$H_{diag} = V^{-1}HV, \tag{A.37}$$

where V is the unitary matrix of eigenvectors.

Bibliography

- [1] C. N. Yang. Some exact results for the many-body problem in one dimension with repulsive delta-function interaction. *Phys. Rev. Lett.*, 19:1312, 1967.
- [2] R. J. Baxter. Partition function of the eight-vertex lattice model. *Ann. Phys.*, 70:193–228, 1972.
- [3] R. J. Baxter. *Exactly Solved Models in Statistical Mechanics*. Academic Press: London, UK, 1982.
- [4] Shuang wei Hu, kang Xue, and Mo-Lin Ge. Optical simulation of the yang-baxter equation. *Phys. Rev. A.*, 78:022319, 2008.
- [5] R. P. Feynman. Simulating physics with computers. *International Journal of Theoretical Physics*, 21:467–488, 1982.
- [6] I. S. Oliveira, T. J. Bonagamba, R. S. Sarthour, J. C. C. Freitas, and E. R. deAzevedo. *NMR Quantum Information Processing*. Elsevier and Amsterdam, 2007.
- [7] C. Negrevergne, T. S. Mahesh, C. A. Ryan, M. Ditty, F. Cyr-Racine, W. Power, N. Boulant, T. Havel, D. G. Cory, and R. Laflamme. Benchmarking quantum control methods on a 12-qubit system. *Phys. Rev. Lett.*, 96:170501, 1 May 2006.
- [8] L. M. K. Vandersypen, M. Steffen, G. Breyta, C. S. Yannoni, M. H. Sherwood, and I. L. Chuang. Experimental realization of shor’s quantum factoring algorithm using nuclear magnetic resonance. *Nature (London)*, 414:883–887, 2001.
- [9] A. M. Souza, J. Zhang, C. A. Ryan, and R. Laflamme. Experimental magic state distillation for fault-tolerant quantum computing. *Nature Communications*, 2:169, 25 January 2011.

-
- [10] E. M. Fortunato, M. A. Pravia, N. Boulant, G. Teklemariam, T. F. Havel, and D. G. Cory. Design of strongly modulating pulses to implement precise effective hamiltonians for quantum information processing. *J. Chem. Phys.*, 116:7599, 2002.
- [11] N. Khaneja, T. Reiss, C. Kehlet, T. Schulte-Herbrüggen, and S. J. Glaser. Optimal control of coupled spin dynamics: Design of nmr pulse sequences by gradient ascent algorithms. *J. Magn. Reson.*, 172:296–305, 2005.
- [12] M. A. Pravia, E. Fortunato, Y. Weinstein, M. D. Price, G. Teklemariam, R. J. Nelson, Y. Sharf, S. Somaroo, C. H. Tseng, T. F. Havel, and D. G. Cory. Observations of quantum dynamics by solution-state nmr spectroscopy. *Concepts in Magnetic Resonance*, 11:225–238, 1999.
- [13] D. G. Cory, A. F. Fahmy, and T. F. Havel. Ensemble quantum computing by nmr spectroscopy. *Proc. Natl. Acad. Sci.*, 94:1634–1639, 4 March 1997.
- [14] N. A. Gershenfeld and I. L. Chuang. Bulk spin-resonance quantum computation. *Science*, 275:350–356, 1997.
- [15] R. Laflamme, E. Knill, D. G. Cory, E. M. Fortunato, T. F. Havel, C. Miquel, R. Martinez, C. J. Negrevergne, G. Ortiz, M. A. Pravia, Y. Sharf, S. Sinha, R. Somma, and L. Viola. Nmr and quantum information processing. *Los Alamos Science*, pages 227–259, 2002.
- [16] I. L. Chuang, L. M. K. Vandersypen, X. Zhou, D. W. Leung, and S. Lloyd. Experimental realization of a quantum algorithm. *Nature*, 393:143–146, 1998.
- [17] J. A. Jones and M. Mosca. Implementation of a quantum algorithm on a nuclear magnetic resonance quantum computer. *J. Chem. Phys.*, 109:1648, 1998.
- [18] R. R. Ernst, G. Bodenhausen, and A. Wokaun. *Principles of Nuclear Magnetic Resonance in One and Two Dimensions*. Clarendon Press and Oxford, 1990.
- [19] M. H. Levitt. *Spin Dynamics*. Wiley and England, 2001.

-
- [20] C. A. Ryan, C. Negrevergne, M. Laforest, E. Knill, and R. Laflamme. Liquid-state nuclear magnetic resonance as a testbed for developing quantum control methods. *Phys. Rev. A.*, 78:012328, 15 July 2008.
- [21] I. L. Chuang, N. Gershenfeld, M. G. Kubinec, and D. W. Leung. Bulk quantum computation with nuclear magnetic resonance: Theory and experiment. *Proc. R. Soc. Lond. A*, 457:447–467, 1998.
- [22] F. A. Bonk, R. S. Sarthour, E. R. deAzevedo, J. D. Bulnes, G. L. Mantovani, J. C. C. Freitas, T. J. Bonagamba, A. P. Guimaraes, and I. S. Oliveira. Quantum-state tomography for quadrupole nuclei and its application on a two-qubit system. *Phys. Rev. A*, 69:042322, 29 April 2004.
- [23] J. Teles, E. R. Deazevedo, R. Auccaise, R. S. Sarthour, I. S. Oliveira, and T. J. Bonagamba. Quantum state tomography for quadrupolar nuclei using global rotations of the spin system. *J. Chem. Phys.*, 126:154506, 17 April 2007.
- [24] F. A. Bonk, E. R. de Azevedo, R. S. Sarthour, J. D. Bulnes, J. C. Freitas, A. P. Guimaraes, I. S. Oliveira, and T. J. Bonagamba. Quantum logical operations for spin $3/2$ quadrupolar nuclei monitored by quantum state tomography. *J. Mag. Res.*, 175:226–234, 2005.
- [25] G. M. leskowitz and L. J. Mueller. State interrogation in nuclear magnetic resonance quantum-information processing. *Phys. Rev. A*, 69:052302, 6 May 2004.
- [26] C. N. Yang. S matrix for the one-dimensional n-body problem with repulsive or attractive function interaction. *Phys. Rev.*, 168:1920, 1968.
- [27] M. Jimbo. *Yang-Baxter Equation in Integrable Systems*. World Scientific, 1990.
- [28] I. B. Frenkel and N. Jing. Vertex representations of quantum affine algebras. *Proc. Natl. Acad. Sci. USA*, 85:9373–9377, 1988.
- [29] M. Gerstenhaber and S. D. Schack. Bialgebra cohomology, deformations, and quantum groups. *Proc. Natl. Acad. Sci. USA*, 87:478–481, 1990.

-
- [30] C. N. Yang and M. L. Ge. *Braid Group, Knot Theory and Statistical Mechanics*. World Scientific, 1994.
- [31] S. C. Billey. Kostant polynomials and the cohomology ring for g/b . *Proc. Natl. Acad. Sci. USA*, 94:29–32, 1997.
- [32] C. P. Sun. The differential realization of new solutions for yang-baxter equation. *Chin. Sci. Bull.*, 37:379–379, 1992.
- [33] P. Gui. Another solution of yang-baxter equation on set and metahomomorphisms on groups. *Chin. Sci. Bull.*, 42:1852–1855, 1997.
- [34] H. X. Chen. Cpcycle deformations, braided monoidal categories and quasitriangularity. *Chin. Sci. Bull.*, 44:510–513, 1999.
- [35] D. P. Hou and C. M. Bai. J-dendriform algebras. *Front. Math. China*, 7:29–49, 2012.
- [36] J. Dubail, J. L. Jacobsen, and H. Saleur. Exact solution of the anisotropic special transition in the $o(n)$ model in two dimensions. *Phys. Rev. Lett.*, 103:145701, 2009.
- [37] D. C. Mattis. *The Many-Body Problem*. World Scientific, 1993.
- [38] M. A. Nielsen and I. L. Chuang. *Quantum Computation Computation and Quantum Information*. Cambridge University Press, 2000.
- [39] S. S. Li, G. L. Long, F. S. Bai, S. L. Feng, and H. Z. Zheng. Quantum computing. *Proc. Natl. Acad. Sci. USA*, 98:11847–11848, 2001.
- [40] Y. Zhang and M. L. Ge. Ghz states, almost-complex structure and yang-baxter equation. *Quantum Inf. Process*, 6:363–379, 2007.
- [41] J. L. Chen, K. Xue, and M. L. Ge. Braiding transformation, entanglement swapping, and berry phase in entanglement space. *Phys. Rev. A*, 78:042324, 2007.
- [42] H. A. Dye. *Unitary solutions to the Yang-Baxter equation in dimension four*. Cambridge University Press, 2000.

-
- [43] L. H. Kauffman and S. J. Lomonaco Jr. Braiding operators are universal quantum gates. *New J. Phys.*, 6:134, 2004.
- [44] Y. Zhang, L. H. Kauffman, and M. L. Ge. Universal quantum gate, yang-baxterization and hamiltonian. *Int. J. Quantum Inf.*, 3:669–678, 2005.
- [45] J. M. Franko, E. C. Rowell, and Z. Wang. Extraspecial 2-groups and images of braid group representations. *Journal of Knot Theory and Its Ramifications*, 15:413–427, 2006.
- [46] E. C. Rowell, Y. Zhang, Y. S. Wu, and M. L. Ge. Extraspecial two-groups, generalized yang-baxter equations and braiding quantum gates. *Quantum Inf. Comput.*, 10:0685–0702, 2010.
- [47] A. Y. Kitaev. Fault-tolerant quantum computation by anyons. *Ann. Phys.*, 303:2–30, 2003.
- [48] M. H. Freedman, A. Y. Kitaev, and Z. H. Wang. Simulation of topological field theories by quantum computers. *Comm. Math. Phys.*, 227:587–603, 2002.
- [49] M. H. Freedman, A. Y. Kitaev, and Z. H. Wang. Wavefunctions for topological quantum registers. *Ann Phys*, 322:201–235, 2007.
- [50] A. Feiguin, S. Trebst, A. W. W. Ludwig, M. Troyer, A. Kitaev, Z. Wang, and M. H. Freedman. Interacting anyons in topological quantum liquids: The golden chain. *Phys. Rev. Lett.*, 98:160409, 2007.
- [51] C. Nayak, S. H. Simon, A. Stern, M. Freedman, and S. D. Sarma. Non-abelian anyons and topological quantum computation. *Rev. Mod. Phys.*, 80:1083–1159, 2008.
- [52] K. Hikami. Skein theory and topological quantum registers: Braiding matrices and topological entanglement entropy of non-abelian quantum hall states. *Ann. Phys.*, 323:1729–1769, 2008.

-
- [53] S. Bose and V. Korepin. Quantum gates between flying qubits via spin-independent scattering. *http://arxiv.org/abs*, page 1106.2329v1, 2011.
- [54] H. Z. Chen W. B. Gao A. G. Fowler R. Raussendorf Z. B. Chen N. L. Liu C. Y. Lu Y. J. Deng Y. A. Chen X. C. Yao, T. X. Wang and J. W. Pan. Experimental demonstration of topological error correction. *Nature*, 482:489–494, 2012.
- [55] D. A. Tennant, T. G. Perring, R. A. Cowley, and S. E. Nagler. Unbound spinons in the $s=1/2$ antiferromagnetic chain kcu $\bar{3}$. *Phys. Rev. Lett.*, 70:4003–4006, 1993.
- [56] D. A. Tennant, R. A. Cowley, S. E. Nagler, and A. M. Tsvelik. Measurement of the spin-excitation continuum in one-dimensional kcu $\bar{3}$ using neutron scattering. *Phys. Rev. B*, 52:13368–13380, 1995.
- [57] Y. A. Liao, A. S. C. Rittner, T. Paprotta, W. Li, G. B. Partridge, R. G. Hulet, S. K. Baur, , and E. J. Mueller. Spin-imbalance in a one-dimensional fermi gas. *Nature*, 467:567–569, 2010.
- [58] Chao Zheng, Jun lin Li, Si yu Song, , and Gui Lu Long. Direct experimental simulation of the yang-baxter equation. *arXiv*, 1305.6086v1:[quant-ph], 2013.
- [59] D. G. Cory, A. F. Fahmy, and T. F. Havel. Ensemble quantum computing by nmr spectroscopy. *Proc. Natl. Acad. Sci. USA*, 94:1634–1639, 4 March 1997.
- [60] N. A. Gershenfeld and I. L. Chuang. Bulk spin-resonance quantum computation. *Science*, 275:350–356, 17 January 1997.
- [61] C. Slichter. *The Principles of Magnetic Resonance*. Springer-Verlag and Berlim, 1990.
- [62] D. G. Cory, M. D. Price, and T. F. Havel. Nuclear magnetic resonance spectroscopy: An experimentally accessible paradigm for quantum computing. *Physica D*, 120:82–101, 1 September 1998.
- [63] E. Knill, I. L. Chuang, and R. Laflamme. Effective pure states for bulk quantum computation. *Phys. Rev. A*, 57:3348, 1 May 1998.

-
- [64] N. A. Gershenfeld and I. L. Chuang. Bulk spin-resonance quantum computation. *Science*, 275:350–356, 17 January 1997.
- [65] L. M. K. Vandersypen, C. S. Yannoni, M. H. Sherwood, and I. L. Chuang. Realization of logically labeled effective pure states for bulk quantum computation. *Phys. Rev. Lett.*, 83:3085–3088, 11 October 1999.
- [66] Minaru kawamura, Benjamin rowland, and Jonathan A. Jones. Preparing pseudopure states with controlled-transfer gates. *Phys. Rev. A.*, 82:032315, 17 September 2010.
- [67] M. Lapert, Y. Zhang, M. Braun, S. J. Glaser, and D. Sugny. Singular extremals for the time-optimal control of dissipative spin 1/2 particles. *Phys. Rev. Lett.*, 104:083001, 2010.
- [68] L. S. Pontryagin, V. G. Boltyanskii, R. V. Gamkerlidz, and E. Mishchenko. *The mathematical theory of optimal processes*. Interscience Publishers, 1962.
- [69] D. E. Kirk. *Optimal Control Theory: An Introduction*. Dover, 1970.
- [70] R.R. Ernst, G. Bodenhausen, and A. Wokaun. *Principles of Nuclear Magnetic Resonance in One and Two Dimensions*. Clarendon Press and Oxford, 1987.
- [71] I. Kuprov and C. T. Rodgers. Derivatives of spin dynamics simulations. *J. Chem. Phys.*, 131:234108, 2009.
- [72] K. Aizu. Parameter differentiation of quantum-mechanical linear operators. *J. Math. Phys.*, 4:762, 1963.
- [73] R. Karplus and J. Schwinger. A note on saturation in microwave spectroscopy. *Phys. Rev.*, 73:1020, 1948.
- [74] A. Mordecai. *Nonlinear Programming: Analysis and Methods*. Dover Publications, 2003.
- [75] J. Nocedal and S. J. Wright. *Numerical Optimization*. Springer, 2000.

-
- [76] M. H. Hestenes and E. Stiefel. Methods of conjugate gradients for solving linear systems. *J. Res. Nat. Bur. Stand.*, 49:6, 1952.
- [77] A. E. Bryson and Y. C. Ho. *Applied Optimal Control*. Blaisdell Pub. Co. Waltham, Mass., 1969.
- [78] O. W. Sorensen, G. W. Eich, M. H. Levitt, G. Bodenhausen, and R. R. Ernst. Product operator formalism for the description of nmr pulse experiments. *Prog. NMR Spectrosc.*, 16:163–192, 29 March 1983.
- [79] C. H. Bennett, G. Brassard, R. Jozsa, C. Crepeau, A. Peres, and W. K. Wootters. Teleporting an unknown quantum state via dual classical and einstein-podolsky-rosen channel. *Phys. Rev. Lett.*, 70:1895, 29 March 1993.
- [80] G. Brassard, S. L. Braunstein, and R. Cleve. Teleportation as a quantum computation. *Physica D*, 120:43–47, 1 September 1998.
- [81] N. Gisin and R. Thew. Quantum communication. *Nature Photonics*, 1:165–171, 2007.
- [82] D. Gottesman and I. L. Chuang. Demonstrating the viability of universal quantum computation using teleportation and single-qubit operations. *Nature*, 402:390–393, 25 November 1999.
- [83] D. Bouwmeester, jian-wei Pan, K. Mattle, M. Eibl, H. Weinfurter, and A. Zeilinger. Experimental quantum teleportation. *Nature (London)*, 390:575–579, 11 December 1997.
- [84] D. Boschi, S. Branca, F. De Martini, L. Hardy, and S. Popescu. Experimental realization of teleporting an unknown pure quantum state via dual classical and einstein-podolsky-rosen channels. *Phys. Rev. Lett.*, 80:1121, 9 February 1998.
- [85] M. A. Nielsen, E. Knill, and R. laflamme. Complete quantum teleportation using nuclear magnetic resonance. *Nature (London)*, 396:52–55, 5 November 1998.

-
- [86] Yasushi Kondo. Quantum teleportation without irreversible detection: Nmr-experiment. *Journal of the Physical Society of Japan*, 76:10, 25 September 2007.
- [87] R. J. Baxter. *Exactly Solved Models in Statistical Mechanics*. Academic, 1982.
- [88] R. J. Baxter. Partition function of the eight-vertex lattice model. *Ann. Phys.*, 70:193–228, 1972.
- [89] I. B. Frenkel and N. Jing. Vertex representations of quantum affine algebras. *Proc. Natl. Acad. Sci. USA*, 85:9373–9377, 1988.
- [90] M. Gerstenhaber and S. D. Schack. Bialgebra cohomology, deformations, and quantum groups. *Proc. Natl. Acad. Sci. USA*, 87:478–481, 1990.
- [91] C. N. Yang and M. L. Ge. *Braid Group, Knot Theory and Statistical Mechanics*, 2nd ed. World Scientific, 1994.
- [92] S. C. Billey. Kostant polynomials and the cohomology ring for $\mathfrak{g}/\mathfrak{b}$. *Proc. Natl. Acad. Sci. USA*, 94:29–32, 1997.
- [93] C. P. Sun. The differential realization of new solutions for yang-baxter equation. *Chin. Sci. Bull.*, 37:379–379, 1992.
- [94] P. Gui. Another solution of yang-baxter equation on set and 'metahomomorphisms on groups'. *Chin. Sci. Bull.*, 42:1852–1855, 1997.
- [95] H. X. Chen. Cpcycle deformations, braided monoidal categories and quasitriangularity. *Chin. Sci. Bull.*, 44:510–513, 1999.
- [96] D. P. Hou and C. M. Bai. J-dendriform algebras. *Front. Math. China*, 7:29–49, 2012.
- [97] J. Dubail, J. L. Jacobsen, and H. Saleur. Exact solution of the anisotropic special transition in the $\mathfrak{o}(n)$ model in two dimensions. *Phys. Rev. Lett.*, 103:145701, 2009.
- [98] D. C. Mattis. *The Many-Body Problem*. World Scientific, 1993.

-
- [99] L. H. Kauffman and S. J. Lomonaco Jr. Braiding operators are universal quantum gates. *New J. Phys.*, 6:0134, 2004.
- [100] S. W. Hu, K. Xue, and M. L. Ge. Optical simulation of the yang-baxter equation. *Phys. Rev. A*, 78:022319, 2008.
- [101] C. A. Rayan, C. Negrevergne, M. Laforest, E. Knill, and R. Laflamme. Liquid-state nuclear magnetic reonance as a testbed for developing quantum control methods. *Phys. Rev. A.*, 78:012328, 15 July 2008.
- [102] Artur K. Ekert, Carolina Moura Alves, Daniel K. L. Oi, Michal Horodecki, Pawel Horodecki, and L. C. Kwek. Direct estimations of linear and nonlinear functionals of a quantum state. *Phys. Rev. Lett.*, 88:217901, 13 May 2002.